Supplementary Materials for

Complex signal processing in synthetic gene circuits using cooperative regulatory assemblies

Caleb J. Bashor*, Nikit Patel*, Sandeep Choubey, Ali Beyzavi, Jané Kondev, James J. Collins, Ahmad S. Khalil[§]

[§]Corresponding author. E-mail: khalil@bu.edu

This PDF files includes:

Materials and Methods
Supplementary Text
Figs. S1 to S24
Tables S1 to S4
Captions for Movies S1 to S2
Reference List

Other Supplementary Material for this manuscript includes the following:

Movies S1 to S2

Materials and Methods

General

All plasmid constructs used in this study are listed in **Table S1**. Construct architecture and open reading frame sequences are described in **Fig. S1**. For constructs used in yeast experiments, codon optimized versions of all ORFs were synthesized (IDT) and cloned into pRS-derived integrating plasmids (*20*) (Stratagene). Strains were constructed by sequential plasmid transformations using standard lithium acetate-based transformation techniques and growth on selective auxotrophic minimal media (Sunrise). The background strain for all experiments in this study was *S. cerevisiae* YPH500 (α, *ura3-52*, *lys2-801*, *ade2-101*, *trp1*, *his3*, *leu21*) (Stratagene). Genotypes for experimentally tested strains are listed in **Table S2**. Experimental replicates, unless otherwise noted, comprised distinct colonies picked from a transformation plate following construct integration and selection.

Recombinant protein expression and purification

The design of plasmids used for recombinant protein expression are described in **Fig. S1** and **Table S1**. Amino acid sequences were identical to those used in yeast, except where indicated in the figure. Synthetic sequences, codon optimized for *E. coli* expression, were synthesized (IDT) and cloned into the pMAL-c5X vector (NEB), and the vectors transformed into BL-21 Rosetta (DE3)pLysS (Novagen) for recombinant expression. Cultures (500 mL, Luria broth supplemented with 1 μM $ZnCl_2$) were grown under constant shaking at 37°C to 0.4 OD_{600} and induced with 1 mM IPTG, whereupon cultures were transferred to 25°C and grown overnight. Cells were pelleted, harvested by sonication into extraction buffer (20mM Tris, pH 8.0, 100 mM NaCl, 20 mM $MgCl_2$, 1 mM $ZnCl_2$, 0.02% NP-40, 20% glycerol), and cleared lysates were incubated with a 0.5 mL bed volume of amylose resin (NEB) at 4°C for 3 h to bind fusion proteins. Resin was washed with 20 column volumes of wash buffer (20 mM Tris, pH 8.0, 100

mM NaCl, 20 mM $MgCl_2$, 1 μM $ZnCL_2$, 10% glycerol), and for species harboring MBP (see **Fig. S1-3)**, proteins were eluted with wash buffer supplemented with 10 mM maltose. For proteins requiring MBP cleavage (see **Fig. S1-3**), resin was mixed with 2.5 mL of wash buffer supplemented with 2 mM $CaCl_2$ and 2 μg Factor Xa (NEB) and incubated overnight at 4°C. Protease was purified away from cleaved protein using a HiTrap benzamidine FF column (GE Healthcare). Proteins were dialyzed into buffer containing 20 mM Tris, pH 8.0, 100 mM $NaCl_2$, 50 μM $ZnCl_2$, 5% glycerol and then concentrated to ~10 mg/mL prior to freezing at -80°C. Concentrations of all protein species were measured by Bradford assay.

In vitro binding assay

In vitro binding assays were performed according to the methods of Jantz and Berg (*34*), with modifications. The probe sequences (IDT DNA) listed below were used for ZF-DNA binding experiments and represent the upper oligo of a temperature annealed duplex:

43-8 n_c=1:
5' - GAA_{fluor}TTCGTCCTCACTCTGGATCC – 3'

42-10 n_c=1:
5' - GAATTCA_{fluor}GACGCTGCTCGGATCC – 3'

43-8 n_c=2 :
5' - GAA_{fluor}TTCGTCCTCACTCTTCGGTCCTCACTCTGGATCC - 3'

43-8 n_c=3 :
5'-GAA_{fluor}TTCGTCCTCACTCTTCGGTCCTCACTCTTCGGTCCTCACTCTGGATCC– 3'

where A_{fluor} indicates the presence of fluorescein label on the thymidine in the bottom (reverse) oligo in the duplex, and underlined sequence indicates DNA binding motif (DBM) for single zinc finger arrays (ZF). Probes were generated by annealing an unlabeled top oligo to a labeled bottom oligo in a 2:1 ratio, while binding competitor oligos were generated using unlabeled top and bottom oligos mixed at equimolar ratios. For PDZ binding experiments, fluorescein-labeled peptide probe (ordered from Selleckhem) used for PDZ binding measurements contained the se-

quence VKESLV*, where the N-terminus was labeled with a FITC conjugate. Probe concentration was assessed by measuring Abs_{490}. Competitor peptides were purified as MBP-ZF_{43-8} fusions (see **Figs. S1** and **S3**).

All assays were conducted in 20 mM Tris, pH 7.5, 100 mM $NaCl_2$, 50 μM $ZnCl_2$ buffer at 25°C. Proteins, probes, and competitor oligos were added to a final volume of 300 μL. Probes were used at 10 nM in all experiments. For complex assembly experiments (**Fig. 1C**), indicated concentrations of MBP-ZF_{43-8} harboring a VKESLV* ligand (see **Figs. S1** and **S3**) were titrated against 5 μM concentrations of clamp. Mixtures were allowed to equilibrate at 25°C for 10 min in Costar black 96-well plates prior to reading. Fluorescence anisotropy (FA) measurements were made at 494 nm using a SpectraMax M5 (Molecular Devices) fluorescence plate reader. For all measurements, anisotropy (r) was calculated using the following equation:

$$r = \frac{I_{\parallel} - I_{\perp}}{I_{\parallel} - 2I_{\perp}}$$

where $I_{\parallel}$ and $I_{\perp}$ are parallel and perpendicular fluorescence, respectively. Fraction of bound probe was calculated using the following equation:

$$f_b = \frac{r - r_{free}}{(r_{bound} - r) \bullet Q + (r - r_{free})}$$

where r_{bound} and r_{free} are the anisotropy values for fully bound and fully unbound probe, respectively. Each of these values was measured independently of binding curves with either a 100x excess or absence of ZF (in the case of ZF-oligo binding) or PDZ (in the case of PDZ-ligand binding). Q is the ratio of total fluorescence (measured at 454 nm) under r_{bound} and r_{free} conditions. To obtain binding constants for ZF-probe and PDZ-probe interactions, binding data were fit to the following quadratic equation:

$$f_b = \frac{[P] + [probe] + K_d - \sqrt{([P] + [probe] + K_d)^2 - 4[P] \bullet [probe]}}{2[probe]}$$

where $[P]$ is the total concentration of either ZF or PDZ, $[probe]$ is the total concentration of the oligo or peptide probe, and K_d is the dissociation constant of the interaction. Competition binding curves were calculated by fitting competition binding curves to the following cubic equation (*35*):

$$f_b = \frac{[RL^*]}{[L_T^*]} = \frac{[R]}{K_{d1} + [R]} = \frac{2 \cdot \sqrt{(a^2 - 3b)} \cdot \cos\frac{\theta}{3} - a}{3 \cdot K_{d1} + 2 \cdot \sqrt{(a^2 - 3b)} \cdot \cos\frac{\theta}{3} - a}$$

where

$$a = K_{d1} + K_{d2} + [L_T] + [L_T^*] - [R_T]$$

$$b = K_{d2} \cdot ([L_T^*] - [R_T]) + K_{d1} \cdot ([L_T] - [R_T]) + K_{d1} \cdot K_{d2}$$

$$c = -K_{d1} \cdot K_{d2} \cdot [R_T]$$

$$\theta = \cos^{-1}\left[\frac{-2a^3 + 9ab - 27c}{2 \cdot \sqrt{(a^2 - 3b)^3}}\right]$$

where f_b is fraction probe bound, [L^*_T] is the total probe concentration, [R_T] and [R] are total and free concentrations of the ZF, respectively, while [L_T] and [L] are total and free concentrations of competitor. K_{d1} is the affinity for TF and probe, while K_{d2} is the affinity between TF and competitor. All binding curve fitting was done using MATLAB (Mathworks, Natick, MA) with function Anisotropy_Fit.m (code description in **Table S3**).

Western blot

Four mL yeast cultures were grown in triplicate to mid log phase in YPGal (YEP + 2% galactose) media in the presence or absence of inducers. Cultures were pelleted and total protein extracted by direct lysis in 200 µL boiling SDS-PAGE sample buffer (Biorad) containing 5 mM dithiothreitol. SynTFs were detected using mouse anti-FLAG (Sigma, #F3165) as primary and Alexa Fluor 488 anti-mouse as the secondary antibody (Cell Signaling, #4408). For hexokinase loading controls, rabbit anti-hexokinase (US Biological Life Sciences, #H2035-02) and anti-rabbit Alexa Fluor 647 (Cell Signaling, #4414) antibodies were used for primary and secondary probes, respectively. Western blot fluorescence was visualized using a Typhoon FLA 9000 (GE Healthcare). Image J (NIH) software was used to quantitate the background-subtracted, integrated intensities of FLAG bands and then normalize to that of the corresponding hexokinase bands.

Flow cytometry

Yeast colonies were picked from plates and cultured overnight in 2 mL liquid SD media with appropriate auxotrophic dropouts. Cultures were diluted 1:50 into 500 µL of YPGal and grown for 16 h in the presence or absence of inducers. Prior to flow cytometry reading, cells were diluted 1:10 into 200 µL of PBS supplemented with 20 µg/mL cyclohexamide and incubated at 25°C, in the dark, for 3 h to allow for complete GFP fluorophore maturation. Typically, 10,000 events were acquired using a BD LSRFortessa equipped with a high throughput sampler (BD Biosciences). Events were gated by forward and side scatter, and geometric means of the fluorescence distributions were calculated in FlowJo (Treestar Software) (**Fig. S6A**).

Microfluidic device construction

Single-cell microfluidic experiments were performed using custom microfluidic devices designed to support monolayer growth of *S. cerevisiae* cells and enable rapid, automated on-chip switching of liquid inputs (**Fig. S16**). To enforce monolayer growth, we used a previously

reported cell trapping design in which chambers were constructed with heights matching the cylindrical diameters of yeast cells (*36, 37*). To this "flow layer", we overlaid a "control layer" of integrated elastomeric valves to facilitate rapid on-chip switching of liquid inputs and outputs (**Fig. S16B**). We developed two variations of this common design. The first, termed '12S2T', was designed to screen a maximum of 12 different strains with up to two distinct environmental time series (six strains per time series; **Fig. S16B**, **top**). The second, termed '12S6T', also accommodates a maximum of 12 strains with the possibility for six distinct time series (two strains per time series; **Fig. S16B, bottom**).

Devices were fabricated using soft lithographic techniques, as described previously (*38, 39*). Two photoresist-based molds, corresponding to flow and control layers, were patterned with respective microchannel structures. The flow layer mold was constructed by first patterning SU-8 2 negative photoresist (MicroChem Corp.) at the appropriate feature height onto a silicon wafer then transferring the cell trapping chamber pattern from a high-resolution transparency photomask (CAD/Art Services, Inc.). Next, AZ4620 positive photoresist (Capitol Scientific, Inc.) was patterned at the greater flow channel feature height and aligned to the trapping chamber pattern before transferring. The completed flow layer mold was placed on a hotplate at 145°C for 1 min to reflow the photoresist and round the channel profiles for complete valve closure in assembled devices. The control layer mold was constructed by patterning SU-8 10 negative photoresist (MicroChem Corp.) onto a second silicon wafer and similarly transferring the control layer pattern from a photomask.

Devices were created by replica molding from the master molds. PDMS/Sylgard 184 was mixed in a 10:1 ratio of elastomer base:curing agent, poured onto the control layer mold to a thickness of ~5 mm, and baked at 80°C for 3 h. Elastomer was prepared in a similar fashion and spun onto the flow layer master (3500 rpm for 60 s), and baked at 80°C for ~10 min. The cured control layer was peeled from the master and aligned over the flow mold under a microscope. The multilayer devices were then baked for an additional 3 h, peeled from the master,

cleaned, and finally sealed to pre-cleaned No. 1.5 glass coverslips (Fisher Scientific). Devices were operated using a previously-described microfluidic platform that integrates plumbing, hardware, and the software that controls valve and liquid delivery (*37*).

Timelapse microscopy and image analysis

Imaging of microfluidic experiments was conducted using an Eclipse Ti-E inverted microscope (Nikon Instruments, Inc.) equipped with a Controlled Environment Microscope Incubator, a XYZ-motorized "Perfect Focus System", and a Clara-E charge-coupled device (CCD) camera (Andor Technology). Images were acquired at 100X magnification (Plan Apo Lambda 100X, NA 1.45). Filters, light sources (Nikon LED and Lumencor SPECTRA X Light Engine), and stage movement were automatically controlled by the supplier's software (NIS-Elements Advanced Research).

Colonies were picked from plates and cultured overnight under auxotrophic selection in 2 mL liquid SD, and then diluted 1:20 into 0.4 mL YPGal and allowed to grow for ~20 h (OD ~0.8) before seeding devices. Flow channels were loaded individually by flowing suspended culture through the 'inlet' ports until 2-10 cells of a particular strain were trapped in at least four growth chambers. Loaded devices were placed on the microscope stage and incubated at 30°C under constant YPGal flow for 5-6 h prior to experimental time course initiation. Cells were then subjected to a specific environmental time series by toggling on-chip valves to control the different media inputs. Phase contrast and GFP images were collected every 15 min at programmed XY positions in three chambers per loaded flow channel. The duration of time-lapse imaging (following a short pre-growth in chambers) in all our experiments was limited to 42 h, after which accumulation of cells at efflux ports could affect the consistent delivery of media and growth of cells across all chambers. Following each experiment, images were analyzed by first using CellTracer (*40*) to segment single cells within each image. Single cell GFP fluorescence values, normalized by cell area, were extracted from segmented images using custom MATLAB soft-

ware (code available upon request). Background fluorescence in the device was subtracted from each segmented cell's fluorescence values. Fluorescence trajectories shown throughout this study represent the mean and standard deviation of all cells across multiple chambers from a single channel (except for the device precision experiments of **Fig. S16D**).

Fluorescence images shown in **Fig. 4B** were generated by segmenting cells and normalizing the background-subtracted fluorescence intensities for each cell to maximum circuit output under constitutive Dox. Strains producing mKate and GFP were false colored red and green, respectively. Cells boundaries determined by the segmentation software are overlaid on each image.

Supplementary Text

Goal: model-driven programming of circuit input-output behavior using cooperative assemblies

Our objective in this study was to explore how sophisticated non-linear signal processing behavior can emerge from synthetic gene circuitry regulated by cooperative complex assembly. The molecular basis of cooperativity has been classically understood through the paradigm of protein allostery. Another mechanism for generating cooperativity is through the self-assembly of multimeric complexes, where avidity created by initial binding events render subsequent higher-order assembly steps more energetically favorable. Transcription factor complex assembly underpins decision making in regulatory networks, allowing network nodes to convert linear, graded inputs into non-linear, “all-or-none” output responses. In metazoan systems, gene networks are thought to utilize assembly-based computation to precisely interpret positional and temporal information during cell state decision-making processes like cell type differentiation and developmental tissue patterning.

We sought to capture essential features of multivalent, cooperative TF binding observed in natural promoter regulation using a simple, modular assembly scheme (**Fig. 1A**). In our design, cooperativity arises when synthetic transcription factors (synTFs) bound in tandem to a multisite promoter are coordinated by a multivalent co-factor (the "clamp") (**Fig. 1B**). The configuration of a synTF complex is defined by three tunable molecular features that determine the free energy of complex formation: the number of synTFs in the complex (n_c), the affinities of the synTFs for the promoter (K_t), and the affinity of the clamp for the synTF (K_p). Understanding how complex configuration gives rise to regulatory behavior requires modeling the functional relationship between K_t, K_p, n_c, and the free energy of complex assembly. Such a model could provide a powerful tool for circuit engineering by enabling the systematic computational exploration of the behavioral space accessible to circuits regulated by cooperative assemblies. This would allow for identification of sets of circuit designs that fulfill a particular target behavior prior to physical construction. Motivated by these possibilities, we created a modeling framework consisting of the following modules:

(**1**) A thermodynamic module that relates cooperative assembly to transcriptional output for a given complex configuration (n_c, K_p, K_t).

(**2**) A differential equation module that describes temporal dynamics for circuits composed of interacting synTF assemblies.

Below we provide a detailed description of how we selected molecular parts used for synTF complex construction, experimentally measured their relevant properties, performed model parameterization based on these measurements, and then utilized the model to simulate circuit input/output behavior and guide circuit construction.

Molecular parts library: selection and parameter measurement

As a first step toward construction of a molecular assembly scheme amenable to modeling, we identified a set of part variants comprising a range of K_t and K_p values, and then conducted *in vitro* binding experiments to directly measure their binding affinities (see **Materials and Methods**) (**Figs. S2-3**). We used fluorescence anisotropy (FA) to measure affinities for two types of purified ZFs (43-8 'ZF1' and 42-10 'ZF2'), and their respective oligo DBMs (*20*). For each ZF, we used previously described R-to-A ZF backbone mutations as affinity variants (*20*). We also generated DBM affinity series (DBM1, DBM2, etc.) for both ZFs by systematically mutating nucleotides both in the core and directly flanking the core 9-bp recognition sequence (ZF1: aGAGTGAGGAc, ZF2: aGACGCTGCTc). Similarly, PDZ-ligand affinities were measured for two domains (syntrophin 'syn' and erbin 'erb') and their respective partner ligands (*41, 42*). For each pair, we obtained ligands of various affinities from published reports (S1, S2, …; E1, E2, …) (*41, 42*) (**Fig. S3**). Altogether, this yielded a set of component interactions consisting of 15 ZF-DNA and 13 PDZ-ligand pairs with *in vitro*-measured values ranging from mid μM to low nM, providing us with broad, tunable control of K_t and K_p.

For *in vivo* experiments, cellular concentrations of synTF and clamp species ($[TF]_{tot}$ and $[C]_{tot}$) were controlled by one of two small molecule-inducible expression systems. Both were selected for their reported non-cooperative dose response profiles. The first is a TetR-regulated *pGAL1* expression system modified to have a linearized, non-cooperative dose-response (ncTET) (*21*) (**Fig. S4A**). The second is a non-cooperative system that utilizes a chimeric estrogen receptor transactivator (ncZEV) (*22*) (**Fig. S4B**). ncTET and ncZEV are induced by anhydro-tetracycline (ATc) and estradiol (EST), respectively. To quantitatively characterize dose responses for these expression systems, we constructed yeast strains harboring either GFP or FLAG-tagged synTF1 (derived from ZF1) placed under expression system control. Dose response curves were obtained for both systems by flow cytometry analysis of inducer-dependent GFP expression (see **Materials and Methods**). After subtracting background/intrinsic fluores-

cence, each dose response was fit to the following Hill model (**Fig. S4,** code description in **Table S3**):

$$F_{obs} = F_{min} + ((F_{max} - F_{min}) \cdot [I]^{n_H} / (EC_{50}{}^{n_H} + [I]^{n_H}))$$

where [*I*] is the concentration of chemical inducer, n_H the Hill coefficient, EC_{50} the chemical inducer concentration at half-maximal response, and F_{min} and F_{max} the minimum and maximum fluorescence values measured in the dose response curves. n_H, EC_{50}, and the fold change of GFP fluorescence (F_{max}/F_{min}) were extracted from this fit and used during model parameterization (see below) as a proxy for the fold change of protein concentration resulting from promoter induction. In order to validate GFP as an accurate surrogate for expression, ncTET induction was assessed by Western blot (**Fig. S4B**). Fitted values were found to be similar for both systems: EC_{50} (60.7 ng/mL by flow cytometry compared to 107 ng/mL by western) and n_H (1.53 by flow cytometry compared to 1.14 by western). Additionally, we measured constitutive fluorescence from a *pADH1* promoter driving GFP expression for different integration loci (**Fig S4A**).

Demonstrating complex formation in vitro

In order to provide a direct demonstration that our molecular components (DNA, synTF, and clamp) are capable of cooperative assembly, we used the FA binding assay to test the effect of both clamp and complex size (n_c) on the cooperativity (n_H) and midpoint (EC_{50}) of a synTF titration (**Fig. 1C**). Species used in the binding assay are described in **Fig. S1**, and descriptions for protein purification and the binding assay are in **Materials and Methods.** For the n_c = 2 binding curves depicted in **Fig. 1C**, an oligo probe with two tandem DBMs and a clamp with two tandem PDZ domains was used. Probe and clamp species with three repeats were used for the n_c = 3 binding curve. Adding clamp to the system (2 μM) increased the affinity of synTFs for the probe (EC_{50} of 210 nM to 18 nM) and cooperativity (n_H = 1.07 to 1.81). This effect

was PDZ-binding dependent, as indicated by the absence of corresponding affinity and cooperativity increases with titration of synTFs containing non-binding ligands (nb). Increasing n_c to 3 further enhanced both affinity and cooperativity (EC_{50} = 5.1 nM, n_H = 2.55), verifying that greater stability is conferred by higher complex valency.

To confirm that nearly all of the change in anisotropy measured during complex formation results from binding of MBP-ZF (and not clamp) to the DNA probe, we conducted a control experiment (**Fig. S5**) where a single PDZ domain was titrated into a mixture containing probe with fully-saturated MBP-ZF binding. Addition of the PDZ made a minimal contribution (<5%) to the overall anisotropy signal, confirming that binding of species composed of low molecular weight PDZ domains have little effect on the anisotropy of synTF-probe complexes.

Optimizing cooperative complex molecular configuration

Individual domains comprising both synTF and clamp species are interconnected by flexible GS-repeat linkers (**Fig. S1**). These occur between ligand and ZF in the synTF, and between PDZ domains in the clamp. We postulated that free energy of complex assembly would depend heavily on domain interdistance, and thus attempted to identify a set of linker lengths that would best facilitate complex formation and transcriptional activation (**Fig. S6B**). We constructed circuits in which synTF expression is driven by ncTET, clamp is constitutive expressed with *pAHD1,* and n_c = 2 complex assembly takes place at a GFP reporter locus. Within this context, we tested three GS linker lengths for synTF1 (0, 5, 10 AAs) against three clamp linker lengths (5, 10, 20 AAs) at three different K_p values. Complex assembly at a GFP reporter locus was assessed by flow cytometry (see **Materials and Methods**). Induced (ATc) and uninduced circuits were compared in strains in which clamp was either present or absent. We assessed the ability of the synTF and clamp to induce higher GFP expression when co-expressed, and the best performing set of linkers (5 GS for synTF and 20 GS for clamp) was selected for circuit construction throughout the paper (**Fig. S6B**).

Thermodynamic model: background and motivation

We selected a statistical thermodynamic framework to model cooperative complex assembly. Similar models have been used to investigate a wide range of biological processes, including transcription, bacterial chemotaxis, and ion channel mechanism (*14, 23, 24, 43*). The fundamental principle underlying such a model is the notion of the microstate: one of many distinct ways that species making up a macroscopic system can be arranged. For a multi-part, self-assembling molecular system, relevant microstates are represented by the fully intact complex, as well as any sub-complexes that exist along a pathway to complete assembly. Construction of a model proceeds by first enumerating these complexes, and then calculating their relative free energies (or, equivalently, their relative probabilities) based on the number and affinity of interactions within each state. When using such an approach to study natural systems, predictive power is often limited by either incorrect assumptions about a system's molecular features, or the presence of unaccounted-for microstates. It is our assertion that by modeling a synthetic system, we obviate many of these concerns. For our synTF/clamp complexes, microstates comprise any distinct promoter-bound configuration of synTFs or clamp. Thus, the set of states available for any given configuration are pre-accounted, with interaction affinity, specificity, and concentration of constituent species fully defined. Moreover, the physical microscopic quantities that we use to describe free energy changes associated with each microstate correspond to affinities (K_t and K_p), over which we have tunable control. Thus, consistent with a major goal of our work, this class of model gives us a quantitative framework for understanding how to tune assembly using the molecular 'knobs' conferred by the variability of our molecular parts. As such, this framework represents a simple, first principles model tailored to our synthetic biology goal of providing insight and predictive power into the design of circuits that utilize our TF assembly scheme to drive target transcriptional behaviors. Studies of natural systems have identified many (other) factors that can affect the process of transcription in eukaryotic cells. Howev-

er, for our synthetic study, many of these factors are not explicitly varied (and in some cases, are controlled across our engineered strains), and thus our model does not account for them. Instead, the model is designed to allow us to dissect specifically the effects of varying assembly parameters on programmed complex formation and transcriptional regulation. Below, we provide a description of the model framework and discuss the assumptions that underlie it. Ultimately, we design experiments that enable us to test the predictive power of the model. Instances where we observe significant deviation between model and experiment may be interesting starting points for incorporating higher-order factors and elaborating on our simple model in future studies.

Model description

Constructing a thermodynamic model for synTF complex assembly involves first identifying all possible promoter-bound synTF/clamp configurations for a given n_c, and then assigning to each a characteristic transcriptional rate (*r*). A weight (*w*) describing the change in free energy for all interactions within each state is computed based on intracellular component concentrations and dissociation constants. Relative transcriptional contributions from each state are given by *w*r*. Because states within the system are assumed to be in thermal equilibrium with one another (which holds true as long as transcription initiation is much slower than rates of synTF binding), the following equation can be used to compute promoter output by averaging relative transcriptional contributions from each state:

$$txn = \sum_i r_i \cdot w_i \Big/ \sum_j w_j$$

where *i* are transcriptionally active states and *j* are all promoter states.

In **Fig. S7**, we apply this framework to the assembly of an $n_c = 2$ promoter complex. To model complex formation under different synTF and clamp expression levels, we first distinguish promoter-bound complex assembly from interactions between promoter-dissociated species in the nucleus. Hill equations relate inducer concentration to component expression, while mass-action equations describing formation of non-promoter complexes (synTF•Clamp and 2*synTF•Clamp) as a function of total synTF and clamp expression levels ($[TF]_{tot}$, $[C]_{tot}$) dictate the concentrations of species available to bind to the promoter. We assume these equilibria to be unaffected by promoter complex formation. Next, the thermodynamic promoter states are enumerated. Under conditions with both synTF and clamp present, the promoter can assume one of five possible states: unoccupied, one synTF bound, two synTFs bound, one synTF bound to clamp, and the full assembly containing two synTFs plus clamp. States containing a single bound synTF are degenerate—they can exist in one of two configurations assumed to be energetically and transcriptionally equivalent. Of the five states, four contain at least one bound synTF and are therefore transcriptionally active. Binding energies for each state are calculated based on the following parameters: (1) concentrations of free synTF and clamp ($[TF]$ and $[C]$), which are related by chemical equilibria to $[TF]_{tot}$ and $[C]_{tot}$, (2) dissociation constants for ZF-DNA (K_t) and PDZ-ligand (K_p) interactions, and (3) a constant (c_2) that accounts for assembly cooperativity by acting as an interaction constant multiplier for the state in which two synTFs are bound to clamp (*14, 43*). The values of *w* are then multiplied by the degeneracy of each state. Finally, each state is assigned an *r* proportional to the number of bound synTFs. We assume that neither synTF position within the DBM array, nor the presence of the clamp itself, influence *r*. For clarity, the expression describing the $n_c = 2$ system is written explicitly in **Fig. S7**. To model $n_c > 2$ complexes, we generalize the $n_c = 2$ case such that the number of states and their corresponding *r* and degeneracy are functions of n_c and the number (N) of bound synTFs, and c_n is a function of N (**Fig. S8,** MATLAB function MeanTxn_OneTF.m in **Table S4**).

There are a number of assumptions to the model. First, it does not explicitly account for the broader yeast chromatin context in which transcriptional regulation is occurring. Studies have proposed, for example, that nucleosome positioning may affect transcriptional output, such as aspects of the transcriptional dose response (*44*). Second, built into the thermodynamic model is an assumption of a single rate limiting step in transcription. Studies have proposed that eukaryotic transcription is a multi-step process, including activator-dependent nucleosome remodeling and transcription initiation (*45, 46*), and that these remodeling dynamics may affect gene expression timing (*45, 47*). In general, these and many other factors can affect the process of transcription and there are exciting efforts aimed at discovering and characterizing them in the context of natural systems. However, our synthetic study does not explicitly vary these factors and in fact by using designed synthetic promoter/reporter systems, we can to some degree control for them. For example, all of our reporters feature the same minimal *CYC1* promoter design, which lacks endogenous upstream regulatory sequences to minimize endogenous TF recruitment, signaling crosstalk, and other undesired regulatory events (*19, 48*). Additionally, our reporters are all single integrated into one of two genetic loci, allowing us to control for certain chromatin context effects across the circuits/strains being compared. This provides a useful background for isolating and testing the effect of altering assembly parameters (over which have tunable control) on transcriptional behaviors. An additional simplifying assumption in our model is that transcriptional rate, r, is linearly proportional to the number of bound synTFs. There is little experimental evidence or consensus to support any specific relationship between the number of bound TFs and transcriptional rate in eukaryotes (*49*). As such, we chose a simple linear relationship, which is both consistent with other recent theoretical work (*49*) and with our goal of developing the simplest model for designing circuits using our TF assembly scheme. Once again, instances where we observe significant deviation between model and experimental results could be intriguing starting points for implementing more complicated relationships and more generally for elaborating on our simple model in future studies.

Fitting and model parameterization

In order to turn our model into a generalizable tool that can be used to predict regulatory functions for arbitrary complex configurations, we conducted parametric fitting on a set of circuit induction data (**Figs. 1D,E**). Experimentally measured values for *in vitro* component binding affinity (**Figs. S2-3**) were used as initial parameter guesses to constrain the fit (**Figs. S7-9**). These values account for affinities between interacting complex components (K_t, K_p). Fitting allows us to infer parameter values for which we do not have *a priori* estimates: the complex cooperativity factor (c_n) and effective maximum *in vivo* concentrations of complex components ([TF_{max}] and [C_{max}]). By fitting data from configurations featuring different n_c, K_t, and K_p under various promoter induction levels (**Figs. 1D,E**), we obtain generalizable functional relationships between not only complex size (n_c) and c_n, but also between promoter induction ([ATc], [EST]) and [TF_{tot}] and [C_{tot}].

The seven circuits comprising the model fitting dataset are shown in **Fig. 1E**. Component expression is driven by ncTET (synTF) and ncZEV (clamp). Each circuit has a slightly different complex configuration (**Fig. 1E**): for n_c = 2 complexes we varied K_t (6.5 nM, 13.6 nM, 143 nM) and K_p (0.88 μM, 1.97 μM, 27.3 μM) affinities, while n_c was varied from 2 - 4 with fixed K_t and K_p values of 13.6 nM and 1.97 μM, respectively. For each of the strains in this set, input-output dose response surfaces (12 ATc by 12 EST doses; 144 total data points) were generated by measuring GFP expression as a function of inducer concentration (see **Materials and Methods**). A global fit on all surfaces was performed using the trust-region-reflective algorithm implementation of Matlab's nonlinear least-squares solver (**Fig. 1E,** code description in **Table S3**). Parameters describing the expression of synTF and clamp by our induction systems (n_H, EC_{50}, and species fold change) were fixed to experimentally measured values (**Fig. S4**). Unmeasured values $[TF]_{max}$, $[C]_{max}$, and c_n were unconstrained during the fit. Measured affinity values (**Figs. S2-3**) were constrained to a 4-fold bound, chosen initially based on reported comparisons of

binding affinities *in vitro* vs. *in vivo* for well-characterized TFs (*50*). To test our fitting methods, we performed multiple parameter fits across a broad range of fitting bounds and found that the goodness of fit of the model, evaluated by mean absolute error (MAE), as well as the fitted affinity values do not change for bounds larger than 4-fold (**Fig. S9B**). As show in **Fig. 1E**, our fitted solution revealed good correspondence between model and data across the entire fitted data set (MAE = 0.088).

The resulting set of fitted parameters represents a transformation of experimental measurements into values that describe effective component behavior in model space. For example, K_t and K_p values were fit-adjusted to optimize $[TF]_{max}$, $[C]_{max}$, which serve as *de facto* proportionality constants relating component affinity to expression system induction. To obtain model space-transformed values for the full set of values measured in **Figs. S2-4**, we used linear extrapolation. First, we extrapolated the expression level of *pADH1*-Clamp based on GFP expression data from **S4** (**Fig. S10A**). In order to obtain a full set of affinity values (K_t and K_p) measured in **Figs. S2-3**, we chose a log-log relationship to extrapolate model affinities from our measured values (**Fig. S10B**). Though absolute affinities could differ *in vitro* and *in vivo*, multiple studies have shown that relative differences between biochemically measured affinities correlate well with relative differences in *in vivo* activity (*51*), thus making this relationship a reasonable approximation. Additionally, c_n values for configurations with $n_c > 4$ were extrapolated following a log linear fit of the three fitted clamp constants using the following equation (**Fig. S10C,** code description in **Table S3**):

$$c_n = 10^{k\cdot(1-n)}$$

where k is a scaling term which was determined from the fit to be 2.18. We chose this relationship because it represents the simplest approximation for the role the clamp plays in affecting the free energy of the complex. We assume that each clamped synTF contributes the same

amount of free energy to the complex, in which case the K_d of binding, being proportional to the exponential of the free energy of the complex, will depend exponentially with the number of binding sites (n).

Relating cooperative complex configuration to circuit behavior

We used the parameterized thermodynamic model to quantitatively map the relationship between complex configuration and circuit behavior for a number of different circuit motifs (**Figs. 2-4, S11-22**). In each case, we generated a database of all possible complex configurations ("configuration space") based on the combinatorics furnished by our available part space. Transcriptional input/output functions were simulated for each configuration, and then used to compute circuit behavior variables ("behavior space"). 2D behavior space plots for relevant variables were generated and used to identify relationships between regions of circuit behavior space and characteristics of corresponding complex configuration space.

Mapping circuit behavior space for single-input circuits

One fundamental signal processing function that cellular regulatory networks perform is the conversion of a non-cooperative regulatory input (dose) into a nonlinear, switch-like output (response). Nonlinear dose response can emerge from cooperative assembly when the titration of a molecular species into a system dominated by weak, low valency interactions leads to the formation of stable, high valency complexes. The greater the energetic difference between low and high valency regimes, the greater the nonlinearity in the relationship between concentration of the titrated species (input) and complex formation (output). In **Fig. S11** we use the parameterized model to demonstrate how nonlinearity can arise from titration and complex formation for a single synTF. We evaluated how the free energy state distribution for a synTF-clamp complex changes by altering configuration features. Total Gibbs free energy change (ΔG) for each state

was calculated by summing binding energies from each of the constituent binary interactions. ΔG for each interaction (K_d) was calculated using the following equation:

$$\Delta G = -k_B T \ln\left(\frac{K_d}{c_{ref}}\right)$$

where k_B is the Boltzmann constant ($J \cdot K^{-1}$), T is temperature (K), K_d is disassociation constant (M), and c_{ref} is a standard reference concentration of 1 M.

As seen in **Fig. S11**, for a low valency $n_c = 2$ configuration, very few states are available for occupancy by complex components, and energetic separation between states is relatively small; plotting *txn* as a function of synTF concentration, we see a non-cooperative dose response ($n_H = 1.0$). Very little nonlinearity ($n_H = 1.02$) is introduced by increasing complex valency (e.g., from $n_c = 2$ to 5) despite the greater overall number of states as well as an increase in the free energy differences between them. Here, higher energy binary synTF-promoter states dominate transcriptional output at lower synTF concentrations, while much lower energy, clamp-bound ternary states dominate at higher concentrations. However, when synTF affinities are lowered for DBM (large K_t values) and raised for the clamp (small K_p values) within the $n_c = 5$ complex, we see a sharp jump in dose response cooperativity ($n_H = 3.1$), as a result of binary and ternary states becoming energetically separated (**Fig. S11**). Thus, our model suggests that it should be readily possible to use different K_t, K_p, and n_c regimes to program dose-response cooperativity, tuning to either non-cooperative or highly switch-like activation profiles.

In order to determine the extent to which our parts collection enables dose response tuning, we used our parameterized model to map the relationship between accessible complex configuration space and behavior space for an inducible single input circuit (**Fig. 2B**). We modeled steady-state GFP output in response to ncTET-driven transcription of synTF1, which assembles with constitutively expressed (*pADH1*) clamp (MATLAB function MeanTxn_OneTF.m in

Table S4). We reasoned that, because the induction profile for ncTET—the first node in the circuit—is non-cooperative with respect to ATc input (n_H = 1.53; **Fig. S4**), it should be possible to manipulate the overall cooperativity of circuit input-output by programming complex assembly at the second node. Complex configuration space was obtained from the combinatorial enumeration of our parts set: K_t (13 affinities) + K_p (15 affinities) + n_c (2-5) + (with and without clamp) = 855 total configurations (**Fig. S12A**). Using our parameterized thermodynamic model, ATc dose response titrations were simulated for the entire configuration space (ATc range = 10^0-10^4 ng/mL) and resulting dose responses were fit to the following Hill function (code description in **Table S3**):

$$txn_{norm} = \left(\frac{a \cdot [ATc]^{n_H}}{EC_{50} + [ATc]^{n_H}}\right) + c$$

where txn_{norm} is the normalized transcriptional output for a circuit with a given configuration, EC_{50} is the ATc concentration at which transcriptional activation is half-maximal, n_H is the Hill coefficient, a is the max activation level, and c is basal expression for each circuit. Both non-activating configurations (a/c < 2) and configurations with high basal expression (c > 0.2) were omitted. EC_{50} and n_H values were extracted from the remaining configurations (603) and plotted as a two-dimensional behavior space (**Fig. 2B**).

As demonstrated by the scatter in **Fig. 2B**, the n_H distribution of low n_c (1 - 3) configurations are narrow and mostly non-cooperative, while higher order configurations (n_c = 4 and 5) show broader distributions, granting access to regions of more switch-like circuit behavior. For both low and high valency complexes, EC_{50} is tunable over approximately 1.5 logs (~5 - 150 ng/mL), a range which is constrained by the dose response profile of the ncTET system (EC_{50} = 60.7 ng/mL). Plotting parameter profiles for configurations in different sectors of the behavior space (**Fig. S12B**) revealed that non-cooperative dose responses were enriched for weak

clamp interactions (large K_p values), while the most cooperative configurations were highly enriched for both weak DNA (large K_t) and strong clamp (small K_p) interactions in a manner consistent with our earlier thermodynamic analysis (**Fig. S11**). We selected a number of configurations evenly distributed across the scatter to test experimentally (**Fig. S12B-C, Fig. 2B**). ATc dose response profiles (ATc = 2182, 1190, 649, 354, 193, 105, 57.5, 31.3, 17.1, 9.32, 5.09, 2.77, 1.51. 0.83 ng/mL) were determined using the same method as in **Fig. S4** and data were fit to the above Hill equation to extract EC_{50} and n_H values. Within this experimental set, we included configurations without clamp and with higher affinity synTF binding sites (strains #2-5 in **Fig. S12B-C**) to test for potential indirect sources of cooperativity(*44*) that are not dependent on clamp. With increasing numbers of higher affinity binding sites (n_c = 2, 3, 4, 5), we did not observe increases in cooperativity (n_H = 1.42, 1.58, 1.36, 1.45, respectively), and all Hill coefficient values were close to that of the ncTET induction system (n_H = 1.53). This result suggests that the clamp plays an essential role in mediating cooperative dose responses in our system.

Finally, comparing model-predicted and experimentally-obtained values of n_H and EC_{50} for each configuration revealed good general correspondence for n_H (MAE = 0.3) and to a slightly lesser extent for EC_{50} (MAE = 26.7 ng/mL) (**Fig. S12D**). This data suggests that our model is broadly predictive of complex configurations capable of quantitatively modulating aspects of the dose response curve with some limitations, particularly for the EC_{50}, which is likely constrained by the dynamic range and EC_{50} of the ncTET induction system controlling synTF expression.

Mapping circuit behavior space for two-input circuits

Cellular networks sense and integrate concurrent environmental signals in a variety of ways. Signals can be integrated linearly, by summing inputs, or non-linearly, by computing inputs in near-digital fashion. We tested our ability to use programmed cooperative complex assembly to tune between these regimes for a two-input circuit, where regulation is mediated by two differentially inducible synTF species that assemble together into a clamped complex (**Fig.**

2C). Dose response behavior for two-input circuits depends not only on the cooperativity associated with binding of each individual synTF, but also on binding interdependence conferred by the clamp. We used our model to investigate the relationship between complex configuration and two-input regulatory function (**Figs. 2C, S13A**). The configuration space that was tested included 6 K_t affinities for each synTF, 5 K_p affinities, and n_c ranging from 2-6 (1-3 for each of the two synTFs), for a total of 8,424 configurations (**Fig. S13A**). For all circuits that were simulated, synTF1 was expressed from a ncTET promoter, and synTF2 from a ncZEV promoter. For each configuration, two-input dose response surfaces were simulated by titrating ATc from 10^{-1}-10^4 ng/mL, and EST from 0.05-12.5 nM to generate surfaces containing 96 x 96 data points (MATLAB function MeanTxn_TwoTF.m in **Table S4**). To identify configurations that exhibit desired target behaviors, we used Kullback-Leibler divergence (D_{KL}), an information theory quantity that measures informational entropy, to assess similarity between simulated and target dose-response surfaces (**Fig. S13B**). D_{KL} is given by the following equation:

$$D_{KL}(P||\,Q) = \sum_i P(i) \ln \frac{P(i)}{Q(i)},$$

which provides a measure of "information lost" when distribution Q is used to approximate distribution P (and thus equals 0 when P and Q are the same) (**Fig. S13B**). D_{KL} was calculated between surface data for simulated surfaces (Q) and target distributions (P) designed to mimic ideal Boolean logic gate behavior (**Figs. S13C, S14A**). Target distributions consisted of 12 x 12 square regions located in the corners of each surface; regions were either uniformly fully transcriptionally active or inactive based on their particular logic (**Fig. S14A**).

We generated a circuit behavior space (**Fig. 2C**) by plotting D_{KL} for an idealized OR-gate behavior against that of an idealized AND-gate (**Fig. S13C**). In qualitative terms, the position of a configuration within this space represents the degree to which binding of the synTF species

during complex formation is either independent (OR-like) or interdependent (AND-like). Configurations that confer the most AND-like and OR-like circuit behavior cluster at two opposing vertices (**Figs. 2C, S14B**), both of which are enriched for higher order (n_c = 4 - 6) complexes. Thus, circuits that exhibit more Boolean-like behavior, with sharper decision boundaries, contain more highly-cooperative assemblies. Circuits conferring more non-cooperative, graded surfaces are found in the fronts between vertices, or near the center of the scatter, amongst complexes with lower n_c. Configurations conferring sharp AND and OR-like logic are enriched for low K_t affinities and high K_p affinities (**Fig. S14B**), while those with graded responses show a broader range of parameter values, particularly for K_p.

In addition to AND and OR logic, we probed the behavior space for other Boolean logic behaviors to assess the behavioral capabilities and limitations of the two-input system. We queried NOR, NAND, and XOR gates, but were unable to find configurations capable of accessing these behaviors. It should be noted the types of logic behaviors that can be accessed by our system are likely limited by our exclusive use of activators to engineer transcriptional regulation. Therefore, only logic functions that feature monotonically increasing transcriptional activity with respect to inducer concentration are likely possible. Indeed, we see little evidence of any non-monotonic behavior in our system, including negative cooperativity between binary and ternary complexes, which might be formally possible through competition between transcription factors for binding to free clamp. Here, the model suggests that clamp is expressed at sufficient quantities to prevent such a scenario.

In order to validate model predictions, we selected various circuits within the behavior space distribution to construct and experimentally test (**Fig. S15A**). We did a simple “4-corners” test, where we added saturating amounts of ATc (2000 ng/mL) and EST (15 nM) inducer either individually, or as a pair (**Fig. S15B**). To quantify the predictive power of the model, we compared model and experimental data in correlation plots of the divergence (D_{KL}) with ideal AND and ideal OR logic (**Fig. S15C**). For the majority of the tested configurations, model and data

show close agreement; however, behaviors predicted to be AND-like for several of the circuits was not observed, suggesting that AND-like assemblies may be extremely sensitive to assembly parameters. When we further analyzed the performance of configurations predicted to give the best AND-gate logic, we found that these tended to show a greater overall deviation from model predictions than all other configurations (**Fig. S15C**). We collected data on full surfaces (ATc = 500, 298.5, 178.2, 106.4, 63.5, 37.9, 22.6, 13.5, 8.1, 4.8, 2.9, 1.7 ng/mL; EST = 12.5, 7.58, 4.59, 2.78, 1.69, 1.02, 0.62, 0.38, 0.23, 0.14, 0.08, 0.05 nM) for a number of these circuits to compare with model predictions, selecting AND- and OR-gate configurations predicted to yield Boolean-like dose response surfaces, as well as configurations predicted to exhibit intermediate behavior (**Fig. 2C**). Using an MAE assessment, we found good overall agreement with between the model and measured D_{KL} values (**Fig. S15C**). Interestingly, AND-logic was less well-predicted by the model than other behaviors. This may be due to assemblies underlying AND-logic being extremely sensitive to both component affinity and intracellular concentration. In the case of the AND-gate, this manifests as difficulty with balancing higher order binding energies for each of the ternary states within the complex.

Dynamic model for circuits composed of interacting synTF assemblies

In order to examine the extent to which programmable complex assembly could be used to program synthetic gene circuit dynamics, we developed a microfluidic workflow to measure single cell response to circuit induction (**Fig. S16A**). We established accumulation and decay of GFP fluorescence in response to a single, saturating square pulse of doxycycline (Dox) as a generic assay for dynamic behavior (**Figs. 3, S16**). Prior to testing cooperative assemblies, we assessed experimental precision for the 12S2T microfluidic device (**Fig. S16B**, see **Materials and Methods**) using square pulse induction of the ncTET-GFP reporter strain (**Fig. S4**). Population-to-population variation in mean fluorescence measured across different chambers (chamber-to-chamber) and different devices (device-to-device) was found to be minor (**Fig. S16D**).

Dox was used in place of ATc for time-lapse fluorescence imaging because of its increased photostability relative to ATc. In **Fig. S16E** we verified that Dox concentration (10 μg/mL) we used for microfluidic experiments was administered at saturating levels.

In order to predict the dynamic behavior of circuits measured in microfluidic pulse experiments, we developed a model that incorporates our thermodynamic treatment of cooperative assembly while using a system of first-order differential equations to account for synTF transcriptional dynamics (**Fig. S17A**). Each equation describes species production from a single circuit "node" (e.g. regulated promoter driving expression of synTF or GFP), and consists of: (i) a basal promoter activity (k_{basal}), (ii) regulated promoter activity (k_{act}), and (iii) degradation of the protein species (k_{deg}). For *(DBM)miniCyc1*-derived promoters regulated by synTF assemblies (**Fig. S1**), transcriptional regulation is described using thermodynamic polynomials described in **Figs. S7** and **S8**, which are multiplied by activation rate constants, k_{act}, to obtain locus-specific rates of species production (**Fig. S17A**).

Activation/deactivation dynamics were measured for a set of five test circuits to obtain training data for parametric model fitting (**Fig. S17B**): (1) The ncTET-GFP expression system (one-node), (2) a two-node network where ncTET drives expression of synTF1 (K_t = 13.6 nM), which activates GFP reporter driven by an n_c=2 promoter, (3) a two-node network where synTF1 drives cooperative assembly (K_t=224 nM, K_p = 1.97, n_c=4) at the reporter, and (4) a three-node cascade in which synTF1 activates production of synTF2 (K_t = 15 nM), which subsequently activates GFP with and (5) without clamp (code description in **Table S4**). We extracted model rate parameters (k_{basal}, k_{act}, and k_{deg}) by performing a pattern search least squares global fit on data traces shown in **Fig. S17B.** During the fit, complex-mediated transcription was calculated using fixed values obtained from previous thermodynamic model fitting (K_t, K_p, c_n, and *pADH1*-driven $[C]_{tot}$) (**Figs. S9-10**). Initial guesses for dilution/degradation rate (k_{deg}) of protein species were approximated to be 0.003 min^{-1} (based on the doubling time of yeast cells in YPGal). Fitting multiple circuits allowed us to extract locus-specific promoter activation rates for

both synTF and GFP transcription (k_{act}). As shown in **Fig. S17B**, our fit solution revealed close correspondence between model and data across the entire fitting set.

Finally, we developed a general relationship that could be used to scale the extracted promoter activation rates (k_{act}) for promoters having different synTF operator numbers (n_c) by constructing two-node cascades with promoter (pSynTF1) variants having n_c = 2-5. We measured the induced maximum circuit output for these variants, and fit this data with a simple logistic function to produce a relationship between n_c and the promoter activation rate (**Fig. S17C,** code description in **Table S3**).

Mapping behavior space for circuit activation/deactivation dynamics

In order to assess the extent to which cooperative complex assembly can be used to predictively tune temporal circuit behavior, we used our integrated model to map activation/deactivation behavior space for circuits comprising three different network motifs: a two-node cascade, three-node cascade, and three-node cascade with positive feedback loop at the second node (**Figs. 3, S18, Table S4**). Activation/deactivation dynamics were calculated in response to a 16 h Dox pulse for the full set of assembly configurations available to each motif (total of 64,080). We filtered out circuit configurations with low maximum outputs (max GFP < 1000 AFU) or weak inducibility (max/basal < 1.5), resulting in a "filtered space" of 12,774 circuit configurations (**Fig. S18B**). Values for activation (τ_a) and decay (τ_d) half-time were respectively defined as the time it takes to reach the half-maximal response following Dox pulse initiation, and time to return to half-maximal response following the end of the pulse (**Fig. 3A**). Circuits that did not decay to less than their half-maximal response within the time frame of the simulation (4000 min) were designated as "no decay". Plotting (τ_a) against (τ_d) for all circuits yielded the behavior space scatter in **Fig. 3B**. Circuits designated as no decay were plotted separately

in a box above the (τ_d) axis. Grey shaded region denotes circuit decay times that exceed the duration of time-lapse imaging in microfluidic devices.

In **Fig. S19A**, we demonstrate that behavior space distribution expansion for two- and three-node circuits in **Fig. 3B** is the result of cooperative complex assembly. Comparing no-feedback configurations with clamp to those without, we see a dramatic expansion along both (τ_a) and (τ_d) axes. In **Fig. S19B**, various peripheral regions of **Fig. 3B** behavior space are highlighted, along with parameter distributions for circuit configurations that fall within each region. Highlighted categories include 'fast ON / slow OFF', 'slow ON / fast OFF', 'slow ON / slow OFF', 'fast ON / fast OFF', and 'Memory'. Parameter profiles for a number of these regions show enrichment in higher-order configurations ($n_c > 3$), once again highlighting the importance of complex assembly in granting access to non-linear behaviors (**Fig. S19B**). Comparing opposing vertices of the behavior space, we see that configurations conferring fast ON / slow OFF behavior are enriched for high synTF2 affinities (small K_{t2} values) at the reporter C-node, while those at the opposing vertex demonstrate a shift to lower affinity values. This was observed for circuits with or without feedback. This affinity difference in the C-node configuration is consistent with a shift from slower to faster deactivation times (e.g., see **Fig. 3B**). Moreover, configurational differences at the B-node are likely important in determining circuit activation time-scales. For example, in the no feedback case, B-node configurations exhibiting fast ON / slow OFF dynamics utilize high affinity clamp interactions (small K_{p1}), in contrast to those in slow ON / fast OFF, which would enable lower activation thresholds and thus faster responses.

Though complex assembly enables expansion of the behavior space for two- and three-node cascades (**Fig. S19A**), there is still a strong (inverse) dependency between (τ_a) and (τ_d), with scatter points lying along the axis connecting the fast ON / slow OFF and slow ON / fast OFF vertices. Our analysis reveals that accessing behavior spaces that break this dependency requires feedback; the only configurations emerging that exhibit slow ON / slow OFF were cir-

cuits with feedback (**Fig. S19B**). Similarly, feedback was a required feature of circuit configurations that show either very slow decay rates (high τ_d) or memory. The lower left corner of the behavior space is not accessible due to a combination of synTF affinities and the inherent limitations imposed by transcription/protein synthesis and decay. Not surprisingly, areas of faster (τ_a) and (τ_d) behavior space can be accessed by two-node circuits (**fig. S19A**), but the behavior distribution shows the same shape – a curved front with a 'knee' - as that of three-node. This shape likely arises from assembly thermodynamics: fast on times that result from low energy complexes assembling at lower synTF concentrations necessarily take longer to disassemble when input is removed and intracellular synTF begins to decay.

A number of interesting features emerge from analysis of feedback-containing three-node circuits. While both type 1 (homo-assembly; both TFs clamped) and type 2 (hetero-assembly; only one TF clamped) B-node architectures were observed for circuits with slow ON / memory space behavior, only type 2 configurations featuring both synTFs complexed together at the B-node could attain slow ON / slow OFF dynamics (**Fig. S19B**). In this latter case, weak synTF1 interactions form the basis for the slow ON phase, while stable complex formation resulting from accumulation of higher affinity synTF2 (small K_{t2} values) enforces positive feedback, resulting in prolonged decay times and a slow OFF.

To test the ability of our kinetic model to predict experimental circuit behavior, we constructed a number of circuits representative of different regions of behavior space, and analyzed their behavior using microfluidics (**Fig. S20A**). Circuits were subjected to a 16 h pulse of Dox (10 μg/mL) on the device after which the inducer was removed and GFP measurements were collected for another 26 h (**Fig. S20B**). See **movie S1** and **S2** for time-lapse videos. From these data, we extracted τ_a and τ_d for each circuit, as we did with model-predicted traces, and compared them to model-predicted τ_a and τ_d (**Fig. S20C**). We found correspondence between model and experiment for ON dynamics (MAE=150.6 min) and, to a slightly lesser extent, OFF dy-

namics (MAE=273 min), suggesting that the model can predict aspects of circuit response dynamics. For a few circuits, GFP profiles showed prolonged decay times, preventing us from obtaining a τ_d within our experimental measurement window (e.g. strain #9 in **Fig. S20B**). As a second method for evaluating model performance, we directly compared model and data for all circuits at specified time points throughout the experiment (**Fig. S20D**). For most circuits, the model and data correspond well through 22 h of measurement (6h post DOX removal), after which predictive power is diminished for a fraction of circuits. Interestingly, the model tended to under predict decay dynamics for a number of three-node + FB configurations. More specifically, configurations that were predicted to decay slowly instead showed no measurable decay within our measurement window (e.g. strains #15, 19, 20 in **Fig. S20**). For these configurations, the dynamic model may have underestimated feedback strength conferred by B-node assembly. Consistent with the idea that fine adjustments in assembly thermodynamics can readily tune feedback circuits between mono- and bistable steady-state regimes (*52*), it is possible that minute inaccuracies in our complex assembly model may render the behavior of feedback-containing circuits more difficult to predict.

Because GFP is a stable protein and highly resistant to proteasomal degradation in yeast, its clearance closely tracks the rate of cell division. Therefore, maintenance of cellular growth in the microfluidic device can be another potential factor that could affect the predictive power of the model. To investigate this further, we quantified cell size for all measurements and found that mean cell size and variation across the population stay relatively constant throughout our experiments (see **Fig. S24A**). Furthermore, analysis of cell number showed that the mean growth rate across our strains (0.0029 min^{-1}) is very close to the dilution rate of GFP in our model (0.003 min^{-1}), providing a cross-validation for our kinetic model fit. These observations are also consistent with prior work showing that synTFs (constructed using affinity mutants ZFs 42-10 and 43-8) confer little to no fitness defects in yeast (*20*) (see **Fig. S24B**). Lastly, we compared mean growth rates with the measured activation and decay times of each circuit and

found no significant correlation (see **Fig. S24C**), suggesting that variation in growth rate does not strongly impact or drive circuit dynamics. However, a detailed investigation would be needed to fully quantify this, and to exclude the possibility that growth rate changes influence the observed differences in circuit dynamics. Limitations of the current study include our ability to accurately measure cellular growth rate over long periods of time: growth rate data is obtained for ~20 h, after which cells fill the chamber and exit the measurable field of view, and microscopic images are captured every 15 min, limiting the accuracy of growth rate determination.

Engineering circuits that interpret and decode dynamic environmental information

In nature, cells are exposed to dynamically-changing environments. Regulatory circuits must interpret fluctuating signals in the environment and precisely translate them into the appropriate cellular response (*26, 53*). Because this type of behavior is, by nature, highly nonlinear, we predicted that creating synthetic circuits that respond to temporal features of the environment, or execute time-based signal processing, could be enabled by our ability to program complex assembly. Implementing time-based control could be used to design and tune filtering functions, e.g. that allow cells to distinguish transient environmental fluctuations from prolonged signals, or become activated under particular temporal input regimes.

Persistence detection: circuits that can discriminate input pulse length

As a first step toward engineering dynamically-gated behavior, we attempted to design circuits that can discriminate between input pulses of different duration. We mapped persistence detection behavior for a configuration space including two- and three-node cascades, and coherent feedforward loops (CFFL) (**Fig. S21A**) – a motif that is not only accessible within our design space, but one that has been postulated to confer persistence detection behavior in natural systems (*27*).

Using our model to simulate behavior, we subjected each circuit configuration to a set of 40 input pulses, with durations ranging from 30 min to 12 h of Dox, and calculated maximum GFP output as a function of time for a 12 h time course. Circuit output for each input pulse was normalized to maximum circuit output (following a 9000 min Dox pulse) and then plotted as a function of pulse length to produce a characteristic "temporal dose response" (TDR) for each circuit (**Fig. S21B**). We filtered out circuit configurations with low maximum outputs (max GFP < 1000 AFU) and weak inducibility (max/basal < 1.5). Using a linear fit at points closest to the half-maximal response, we approximated two metrics from each TDR that define persistence filtering behavior: (1) input duration threshold (input duration at half-maximal response) and (2) filter sharpness (*s*, slope of TDR at half-maximal response). Just as Hill coefficient represents sensitivity to concentration changes in a biochemical dose response, temporal filter sharpness serves as an index for the sensitivity of circuit output to changes in pulse length duration.

In **Fig. S21C,** temporal filter sharpness (*s*) was plotted versus input duration threshold for all circuits. Analysis of the resulting behavior space revealed three-node cascades provide the broadest range of persistence filtering behaviors, and comprise nearly all circuits that exhibit the sharpest filtering. Analysis of these filters revealed an enrichment in highly-cooperative assemblies (high n_c, large K_t, small K_p values) (**Fig. S21C**). CFFL circuit configurations demonstrated many instances of sharper filtering behavior compared with those in the two-node distribution. However, despite previous description of this motif as an effective persistence filter (*27*), none of the CFFL configurations were as sharp as the top 4.5% of three-node cascades. Taken together, our analysis demonstrates strong correspondence between circuit node nonlinearity and filter sharpness, suggesting that complex assembly can be effectively used to tune temporal dose response.

In order to validate model predictions, a circuit predicted to be a sharp filter was constructed: a three-node cascade with high n_c complexes. This 'nonlinear' circuit was compared to the simple 'linear' circuit from **Fig. 3A**, which is a non-cooperative two-node cascade that falls

into the region of behavior space with diminished sharpness (**Fig. S21C**). We used microfluidics to measure each circuit's maximum output in response to six pulse lengths (durations ranging from 30 min to 16 h) and observed close agreement between measured and model-predicted behaviors (**Fig. 4A**).

Mapping frequency response behaviors

Dynamic information can be encoded in other aspects of a signal besides the duration of a single pulse. The archetypal example in biology is neural coding, in which a stimulus is coded in the temporal pattern of a neural spike train (*54*). Dynamic information coding and decoding appears to be pervasive in cellular regulatory systems as well. For example, a variety of regulatory molecules (e.g. p53, Msn2, etc.) have been shown to display pulsing behavior in cells, and these dynamic patterns of activity can encode information about the nature of an upstream stimulus in temporal features, such as the pulsing frequency (*25, 26*). Moreover, experiments subjecting cells to time-varying (oscillatory) stresses have shown that cellular networks may have the ability to decode frequency information from environmental signals (*28*).

At the cellular level, systems analysis has identified specific network motifs for their ability to generate characteristic and useful responses to time-dependent inputs (*27*). To see whether our available circuit design space could support temporal signal processing, we extended our computational methods to assess frequency response behavior. We examined five circuit motifs accessible to our part space: two-node cascade, three-node cascade, cascade + FB, CFFL, and CFFL + FB (total collection of 169,552 configurations) (**Fig. S22**).

Frequency response for each circuit was obtained by simulating circuit output in response to a series of 20 periodic (square wave) Dox inputs, with periods ranging from 90 min (high frequency) to 9000 min (low frequency). All input regimes have the same 33% duty cycle and thus experience an identical duration of total input. A frequency response curve was generated for each circuit by plotting maximum GFP output (normalized to maximum output for consti-

tutive Dox) for each input frequency (**Fig. S22B**). Examining the resulting response curve database, we identified two patterns of circuit behavior that demonstrate dramatically different output minima and maxima: one which filters high frequency input, only responding to low frequency regimes, and another which responds poorly to low frequency regimes, but is activated at high frequency. These circuit types effectively function as low-pass and band-stop filters, respectively, and are discretely activated at different points along the frequency input axis.

Within the response curve database, we systematically identified circuits of each filter type based on the following criteria: low-pass filters were defined by a ratio of low to high frequency amplitude > 5, while band-stop filters were defined as having ratio of high frequency to minimum amplitude > 2 (**Fig. S22B**). This screen yielded 4,726 low-pass and 327 band-stop candidates. In configurations supporting both behavior types, we observe cooperative, high n_c complexes, further validating our prediction that filtering behavior is enabled by cooperative assembly. Circuits with low-pass behavior were comprised primarily of three-node cascades and CFFLs, with B-node enrichment of highly-cooperative assemblies (large n_c, large K_t, small K_p values) (**Fig. S22C**). Within CFFLs, we find an enrichment in configurations that exhibit AND-like logic at the C-node (both synTFs in complex), consistent with previous work implicating this type of regulatory logic for sharp filtering (*27*). Band-stop circuit configurations all contained B-node feedback, suggesting that retaining memory of prior events plays a role in this type of filtering. Indeed, we see enrichment of B-node configurations similar to those conferring slow ON / slow OFF dynamics for single pulses (**Fig. S21**). The dynamics of these circuits (weak activation triggers and strongly reinforced type-1 B-node assembly and slow decay) would appear to underpin their ability to filter out mid-range frequencies, while responding to high frequency environments by integrating successive short pulses over time.

Temporal decoding: engineering circuits that can distinguish between different input frequencies

Since the frequency response profiles for low-pass and band-stop filters have non-overlapping regimes of frequency space, we surmised that, if tuned properly, these two filter classes could be used to create a 'mixed' cellular population able to readily distinguish between unique frequency environments (temporal decoding). To experimentally demonstrate this, we selected from our analysis top hit low-pass and band-stop configurations for construction (**Figs. S22B, S23**). We placed mKate2 under expression control of the low-pass (CFFL) circuit and GFP under control of the band-stop (CFFL+FB) circuit (**Fig. 4B**). We then mixed equal concentrations of the two engineered yeast strains, co-cultured them in the 2S6T microfluidic device, and analyzed their behavior when exposed to varying Dox input frequencies (with periods ranging between 3 h to 60 h, all with 33% duty cycle). The resulting frequency response curves for each circuit show agreement with model predictions and, critically, reveal distinct regimes of frequency space ('low' and 'high') in which the circuits have opposite outputs (**Fig. S23**). Representative fluorescence images of the co-cultures exposed to these two regimes confirm the discriminatory ability of the population based on mKate2 and GFP reporter output (**Fig. 4B**).

Conclusions

In summary, our work demonstrates that manipulating the molecular interactions within a synthetic promoter complex facilitates tuning between linear and non-linear computational functions, unlocking steady state and temporal circuit behaviors inaccessible to non-assembly schemes. This work suggests that the widespread deployment of cooperative complexes in native systems may have been a natural design strategy that allowed networks to evolutionarily modulate between linear and nonlinear signal processing regimes without the need to evolve new wiring or additional regulatory components, thereby allowing a relatively low diversity of molecular components to execute the exponentially larger number of computations required for metazoan regulation. Use of engineering approaches that incorporate cooperative assembly as a design feature could therefore facilitate creation of densely interconnected signal processing

circuitry with a level of density and computational sophistication approaching that of natural networks, enabling precision control in applications where non-linear temporal and spatial signal processing are critical, such as circuit-directed cell differentiation or dynamic regulation of homeostasis in engineered tissues.

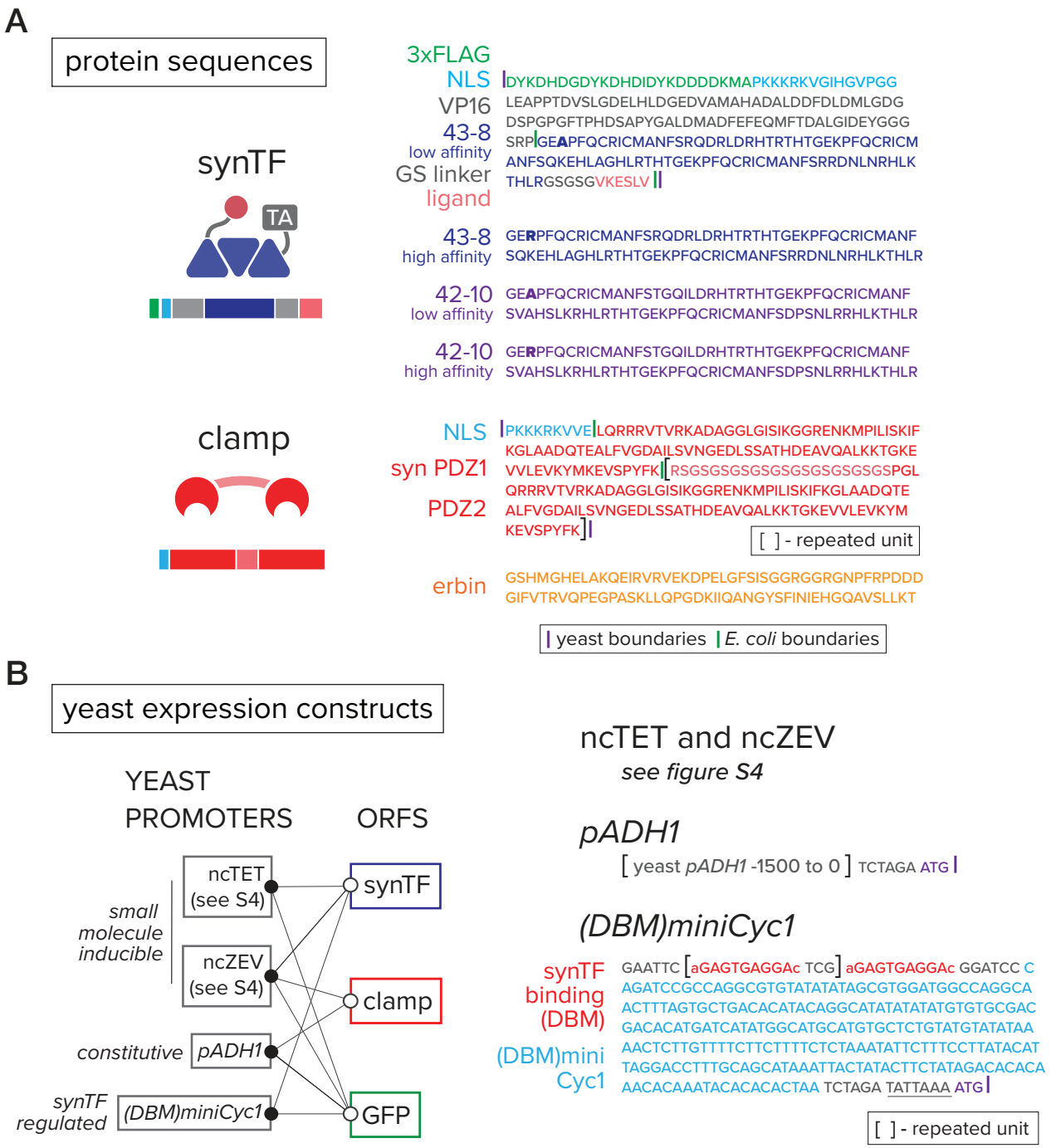

Figure S1. Sequence details of synthetic promoter and protein components. Plasmid constructs listed in **Table S1** are composed entirely of molecular components described in this figure. (**a**) Amino acid sequences common to all synthetic transcription factors (synTFs) and clamps used in this study. synTFs feature a FLAG epitope tag, nuclear localization sequence (derived from SV40 NLS), and VP16 transcriptional activation sequence upstream of a triple repeat zinc finger array. For zinc finger affinity alleles, mutated residues are highlighted in bold. Clamps contain the same N-terminal nuclear localization sequence as synTFs. An n_c=2 clamp sequence is depicted, and the unit repeated in higher order clamps is highlighted. Flexible GS repeat linker sequences for both synTF (5AAs) and clamp (20 AAs) are depicted at lengths found to be optimal for complex assembly (see **Figure S6B**). Yeast or *E. coli* optimized coding sequences were cloned into expression plasmids (see **Table S1**) at the indicated boundaries. For yeast, N-terminal boundaries directly abut promoter-associated start codons, while *E. coli* boundaries indicate fusion with expression vector MBP (see **Materials and Methods**). (**b**) Promoter/coding sequence pairs used in circuit construction. All combinations of promoter and coding sequence used in **Table S1** yeast expression constructs are indicated (left). DNA sequences for *pADH1* and *(DBM)miniCyc1* promoters, and associated start codons are indicated (right). *(DBM)miniCyc1* with 43-8 DNA binding motif (DBM) sites for an n_c=2 configuration is depicted. The highlighted unit gets repeated in the 5' direction to create higher order assemblies. Kozak sequence is underlined and translational start (ATG) is colored purple.

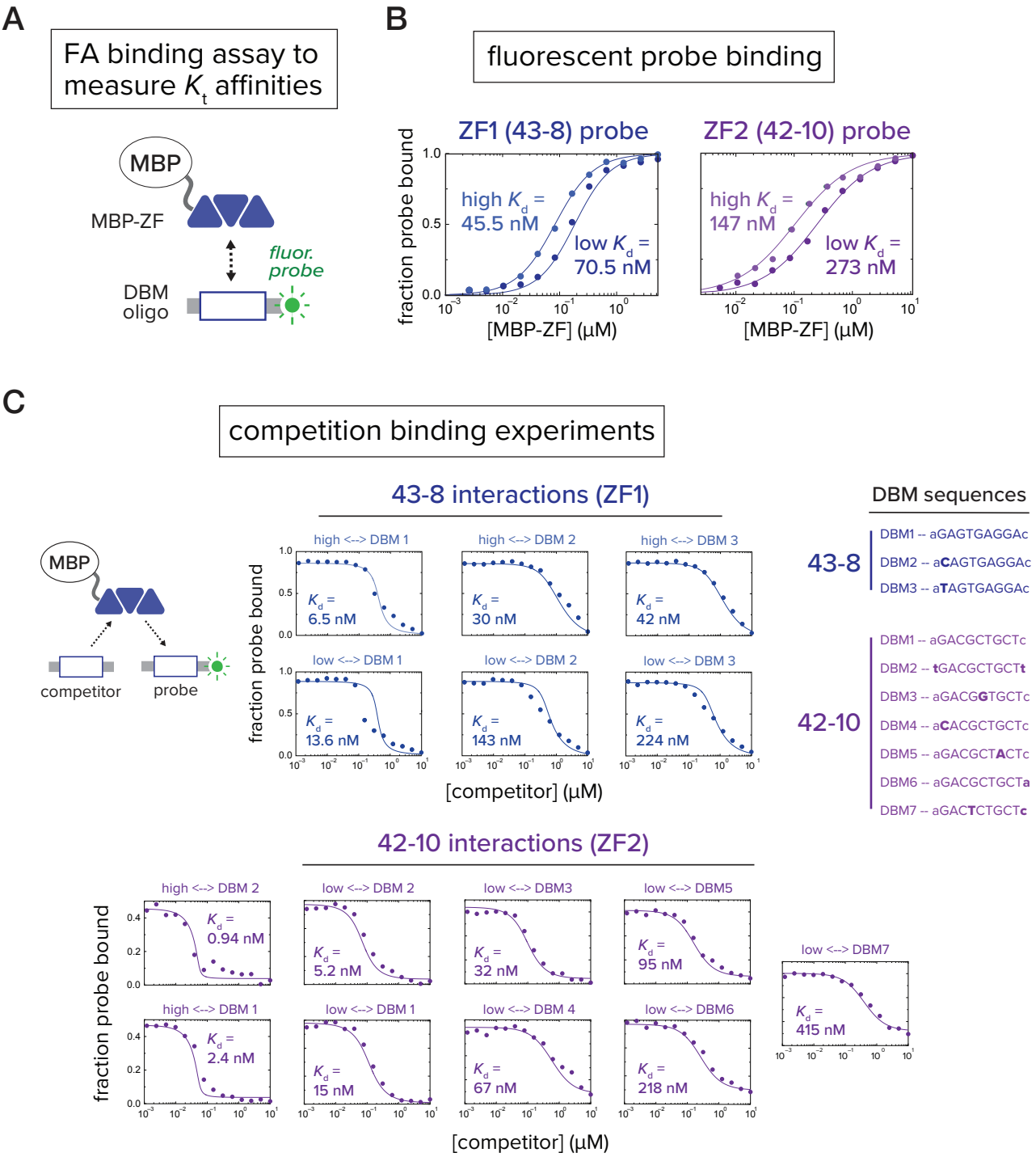

Figure S2. *In vitro* measurement of TF-DBM binding constants by fluorescence anisotropy (FA). Recombinant proteins were purified and DBM oligos prepared as described in **Materials and Methods**. (**a**) MBP-ZF fusion proteins (see **Figure S1** for sequence details) bind to oligonucleotide probes harboring a single DBM repeat. Affinities for the interaction were measured as a function of the increase in fluorescence anisotropy resulting from binding of the fusion to a fluorescently labeled (FITC) oligo probe (see **Materials and Methods**). (**b**) Measuring oligo probe binding to ZF affinity variants. MBP-ZF was titrated against 10 nM oligo probe. Change in anisotropy was converted to the fraction of bound probe and binding curves were obtained for high and low affinity variants for both 43-8 (TF1) and 42-10 (TF2) species. K_d values were extracted by fitting data to a quadratic binding equation (see **Materials and Methods**). (**c**) Using competition binding experiments to measure binding constants for DBM affinity variants. At concentrations of MBP-ZF and probe at which half-maximal binding was observed in **Figure S2B** experiments, we titrated unlabeled oligo competitors containing DBM affinity variants and measured anisotropy increases accompanying displacement of the probe by the competitor. Competitor oligo K_d values were extracted by fitting data (converted to fraction probe bound) to a cubic equation describing competitive binding (see **Materials and Methods**). Sequences for both sets of DBM affinity variants are listed on the right. Residues mutated from the WT sequence are indicated by bold type.

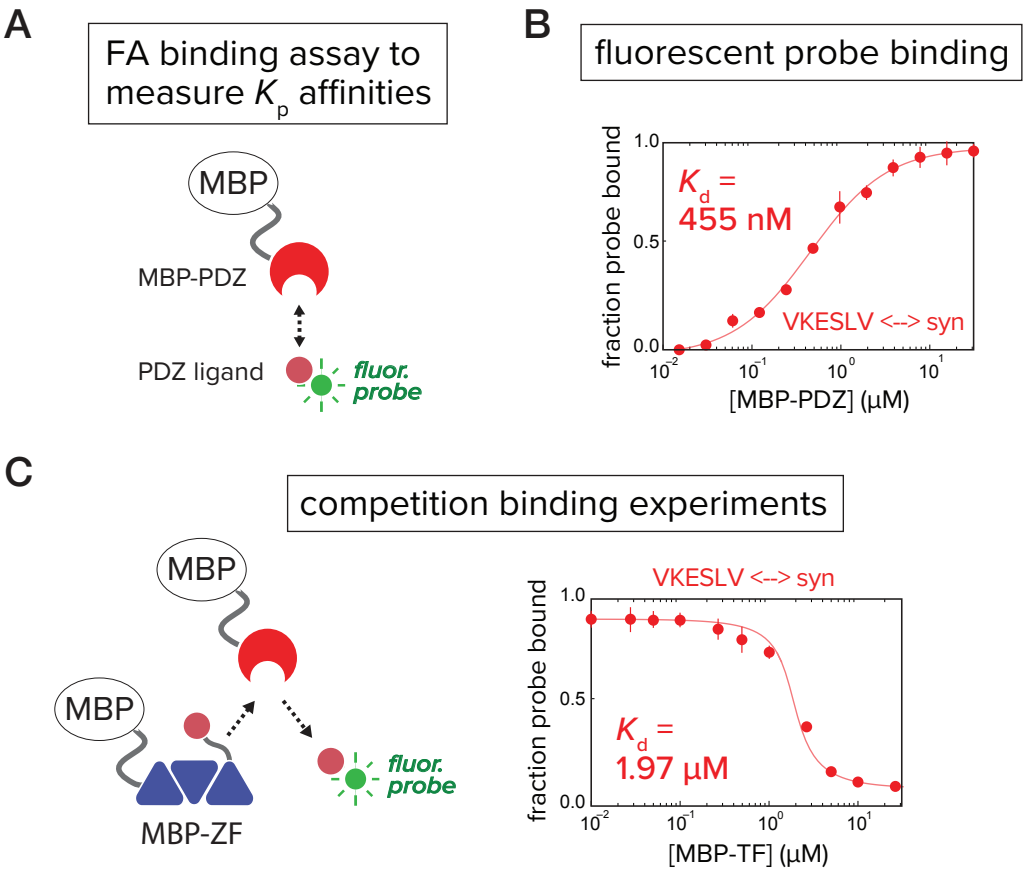

D

		competitor ligands	syn K_d (μM)	erb K_d (μM)
syntrophin-specific	S1	IRETII	0.062	nb
	S2	IRETIL	0.18	nb
	S3	IRWTIV	0.49	1.73
	S4	IRETIV	0.88	3.46
	S5	VKESLV	1.97	5.71
	S6	VKEALV	27.3	nb
	S7	HLETFF	43.2	nb
no binding		VKEAAA	nb	nb
erbin-specific	E1	WLVTWV	nb	0.10
	E2	WLKTWV	nb	0.33
	E3	PVDSWV	1.57	0.42

Figure S3. ***In vitro*** **measurement of PDZ-ligand binding constants by fluorescence anisotropy.** Recombinant proteins were purified as described in **Materials and Methods** (**a**) MBP-PDZ fusion proteins (see **Figure S1** for sequence details) bind to peptide ligand probe. Affinities for the interaction were measured as a function of the increase in fluorescence anisotropy resulting from binding of the fusion to a fluorescently-labeled (FITC) oligopeptide probe (see **Materials and Methods**). (**b**) Measurement of peptide probe binding to PDZ domain. MBP-PDZ was titrated against 10 nM peptide ligand probe, and anisotropy data were converted to fraction of bound probe. Binding curves were obtained for high and low affinity variants for the syntrophin PDZ domain. K_d values were extracted by fitting data to a quadratic binding equation (see **Materials and Methods**). (**c**) Competition binding experiments were conducted to measure binding constants for ligand affinity variants. At concentrations of MBP-PDZ and probe at which half-maximal binding was observed in **Figure S3B** experiments, we titrated 43-8 synTFs with appended ligands of various affinities. Anisotropy increases accompanying displacement of the probe by the competitor was measured, and competitor ligand K_d values were extracted by fitting data (converted to fraction probe bound) to a cubic equation describing competitive binding (see **Materials and Methods**). (**d**) Table of competitior ligand K_d values collected for both syntrophin and erbin PDZ domains.

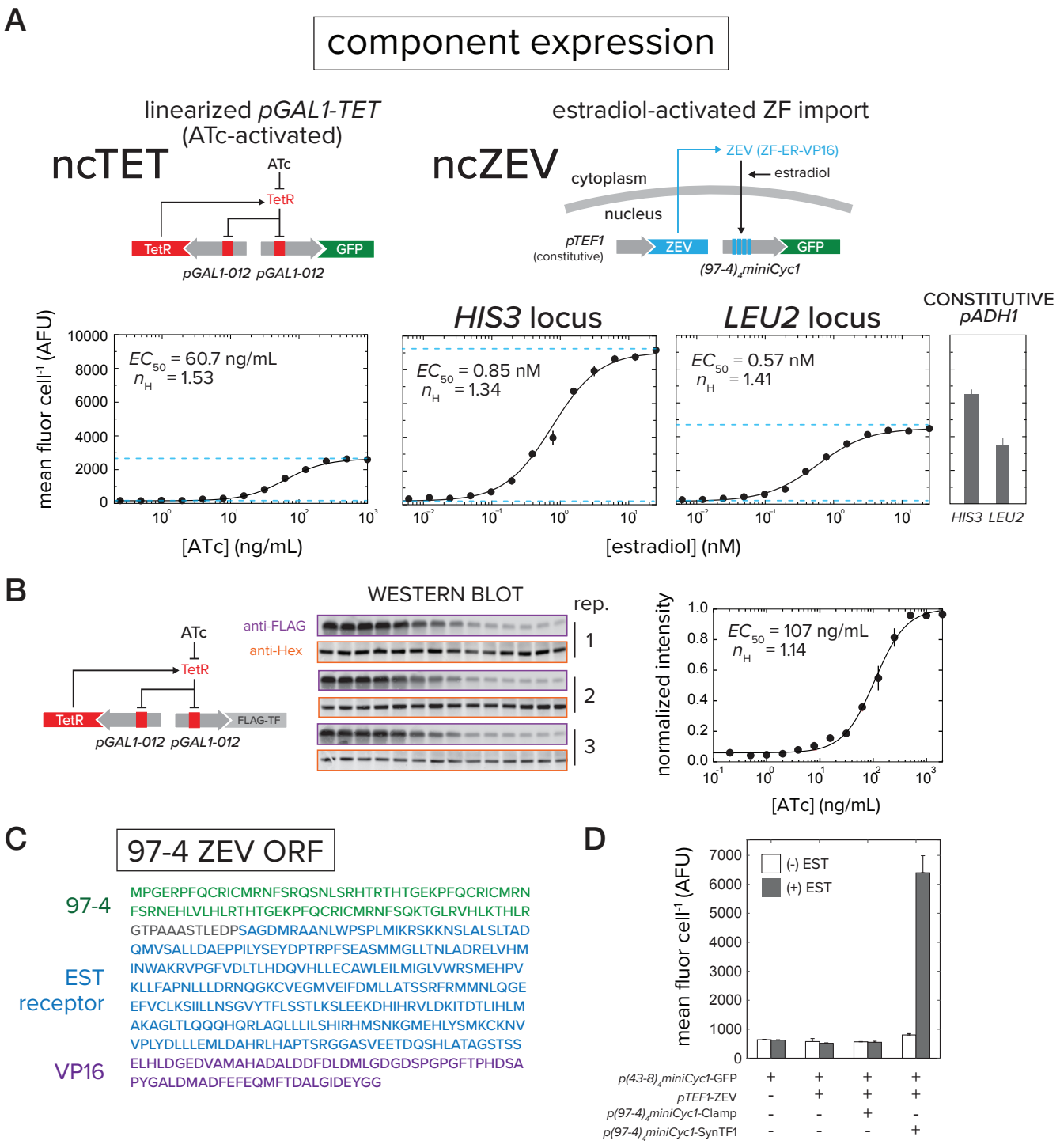

Figure S4. Characterization of inducible and constitutive expression systems. Experiments were conducted to obtain model input parameters for circuit component expression systems. **(a)** Using GFP as a surrogate to quantitate promoter expression. For inducible expression systems, dose response curves were generated to characterize transfer functions between inducer concentration and transcriptional output. For the ncTET system, ATc was titrated, while EST was titrated for the ncZEV system. Measurements were made for induced cultures at mid-log growth by flow cytometry. Error bars represent standard deviation for three replicates. Curves were fit according to a Hill model (see **Supplementary Text**). Blue dotted lines indicate minimum and maximum expression levels as determined by fit. Constitutive expression from *pADH1* (see **Figure S1**) was measured for both *LEU2* and *HIS3* loci. Parameterization experiments for *(DBM)miniCYC1* promoters are described in **Figure S17**. (**b**) Validation of GFP expression system by western blotting. In three separate blots, top panels were probed with anti-FLAG antibody (purple) and bottom panels with anti-Hex loading controls (orange) (left). Band intensity was measured using ImageJ, and mean normalized intensity data (error bars = std. dev.) were plotted and fitted with a Hill equation. (**c**) Amino acid sequence of the ZEV transcription factor involved in the ncZEV activation system. A 97-4 zinc finger was appended with the estrogen receptor harboring a C-terminal VP16 activation domain. Expression of the resulting coding sequence was driven by the *pTEF1* promoter (-417 to 0). (**d**) ncZEV does not affect transcription of the reporter in the absence of its target synTF1. Strains were constructed with different combinations of: reporter ((*p(43-8)*4miniCyc1-GFP), ZEV expression cassette, ZEV-inducible clamp, and ZEV-inducible synTF1. All four strains were grown with and without 25 nM EST. Mean GFP fluorescence values were measured by flow cytometry. Error bars represent standard deviation.

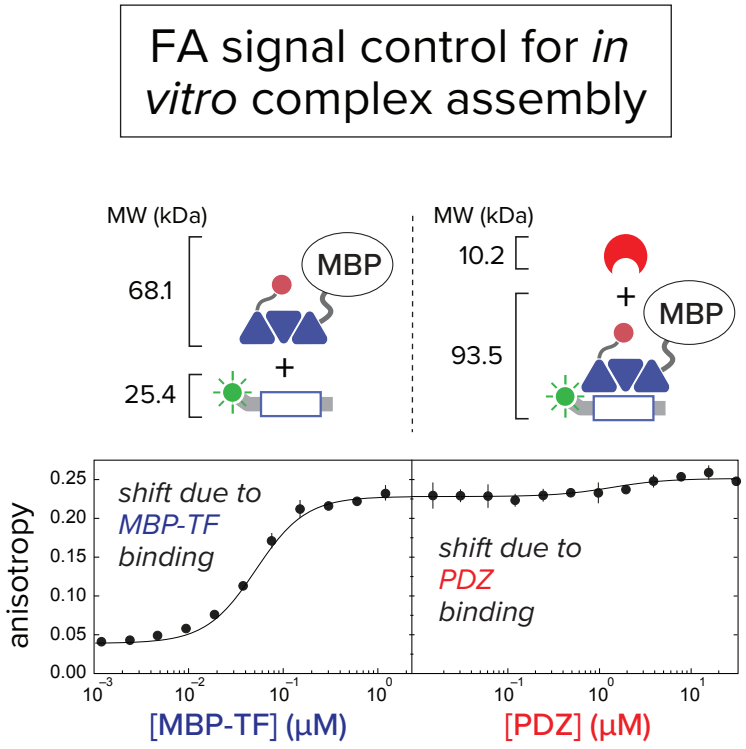

Figure S5. Component anisotropy signal contribution. A control experiment was run to verify minimal contribution of PDZ domain/clamp binding to overall change in anisotropy signal upon complex formation. Molecular weights for components and complexes are indicated to the left of each complex component (see **Figure S1** for sequence information). Binary complex was assembled by titrating MBP-TF against 10 nM fluorescent probe. Saturated binary complex was titrated with a syntrophin PDZ domain. Lines represent Hill fits for both titrations. Error bars are standard deviation for three replicates.

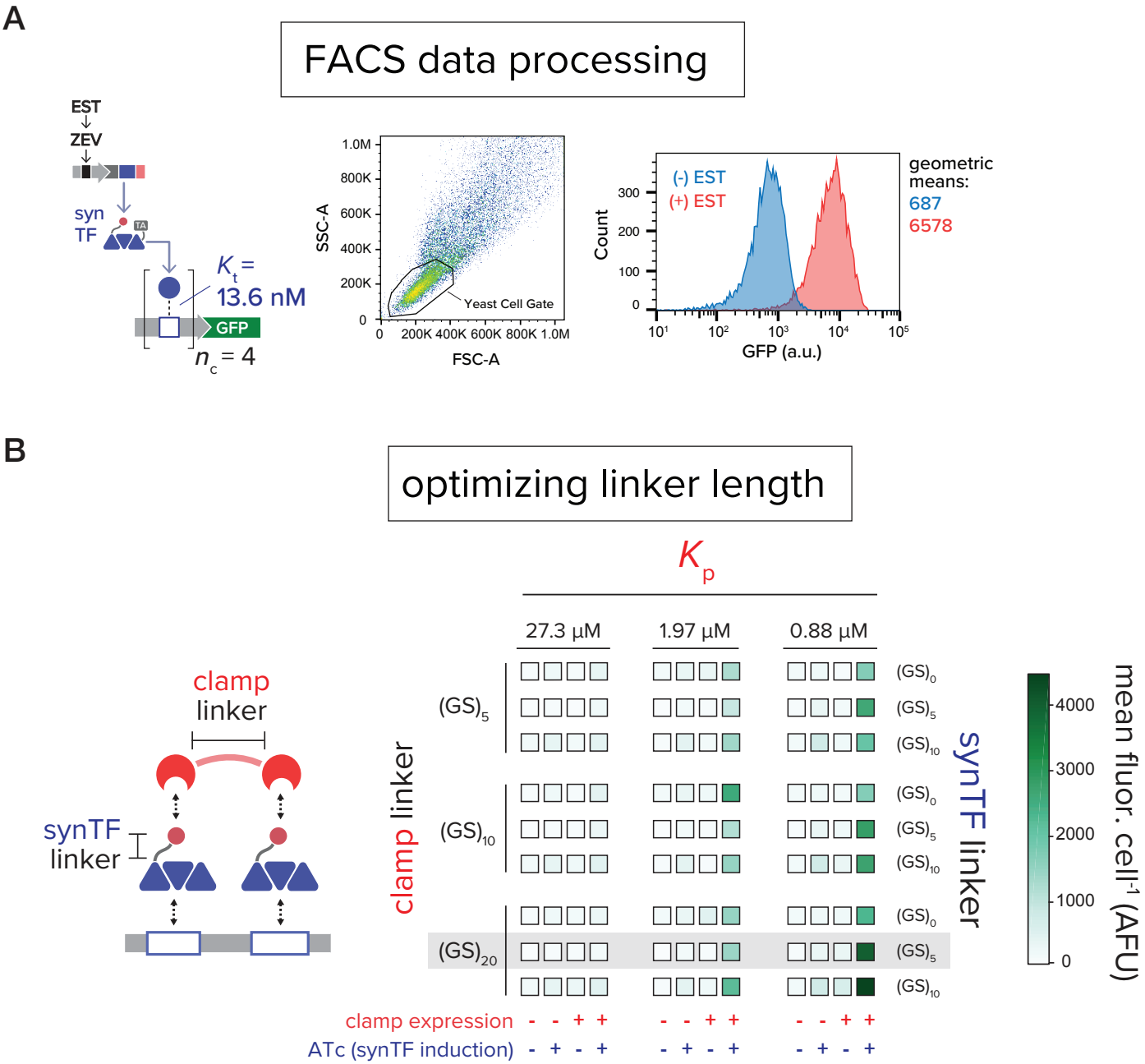

Figure S6. Screening linker length combinations to optimize complex-mediated transcriptional output
(a) Workflow for processing flow cytometry data. In order to determine mean reporter fluorescence intensities, yeast cell populations are gated by forward (FSC) and side scatter (SSC) resulting in ~10,000 events (center). Geometric mean fluorescence intensities are then determined for gated poulations (right). Data shown are representative fluorescence distributions for a yeast strain with ncZEV controlling a synTF and corresponding n_c=4 reporter (-/+ 25 nM EST). **(b)** We screened flexible interdomain linkers of both synTF and clamp proteins to identify combinations of linker lengths that yield high transcriptional synergy (see **Figure S1** for component sequence details). synTF expression is controlled by ATc-inducible ncTET and clamp is either constitutively expressed or absent (see also **Figure S4**); synTF/clamp complex assembles as an n_c=2 complex, driving expression of a GFP reporter (top left). GS-repeat linkers interconnect ZF and ligand domains in the synTF, and PDZ domains in the clamp (bottom left). Three different synTF linker lengths (K_t = 13.6 nM) were tested against three lengths in the clamp, for three different K_p values (right). Configurations yielding high transcriptional synergy produce high GFP output when synTF is induced and clamp is present (+/+), relative to when components are expressed individually. Grey box highlights the synTF/clamp linker pair exhibiting the highest transcriptional synergy from our screen ($(GS)_x$=glycine-serine linker of length x).

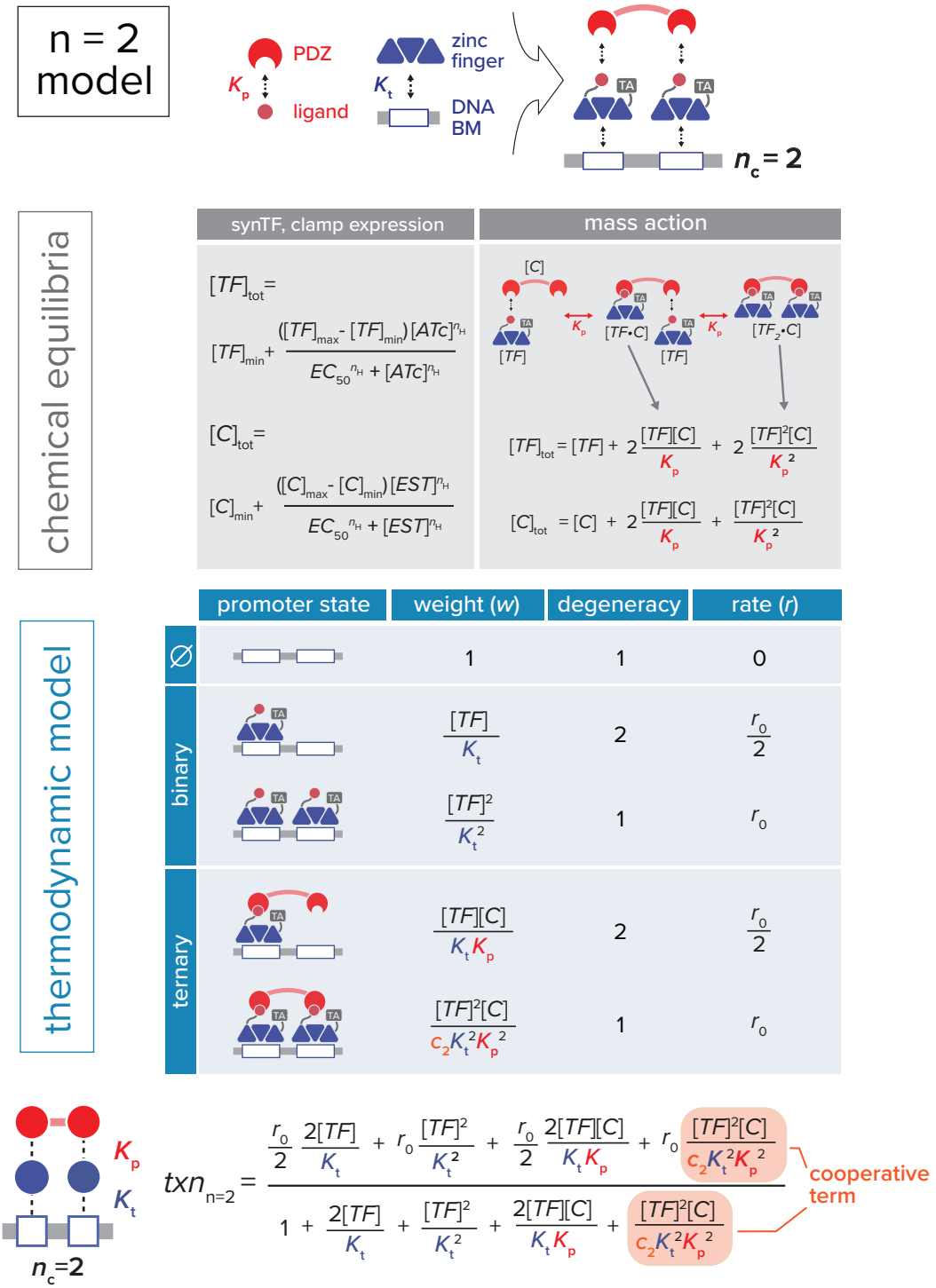

Figure S7. Thermodynamic model for n_c = 2 complex assembly. The mathematical model describing assembly of an n_c=2 promoter complex has three components: **(1)** Grey boxes: Chemical equilibria dictate concentrations of freely-diffusing species available for promoter binding. In our experimental system, synTF and clamp expression is controlled by ATc-inducible ncTET and EST-inducible ncZEV, respectively. Thus, Hill equations are used to describe the relationship between inducer and the *in vivo* concentrations of expressed components (left box, see also **Figure S4**). Mass-action equations are used to account for concentrations of all available species, including free monomeric components ([*TF*] and [*C*]) and non-promoter multimeric complexes (right box). **(2)** Blue boxes: Enumeration of possible promoter states. Each of the five states is assigned a corresponding thermodynamic weight (*w*) that describes the change in free energy for interactions within that state. (K_t = synTF-promoter binding affinity; K_p = PDZ-ligand binding affinity; n_c = size of the complex) Each state is assigned a degeneracy that accounts for thermodynamically equivalent sub-states, and a transcription rate (*r*) proportional to the number of bound synTFs. (r_0 = maximum transcriptional output of the promoter.) The weight for the ternary complex (synTF + clamp) features a cooperativity constant (*c*) that represents additional stability afforded by the multivalent interaction (see also **Figure S10**). (3) Transcriptional activity (bottom): A function describing transcriptional output (txn_n) is obtained by averaging the relative transcriptional contributions (*w*r*) of all promoter states.

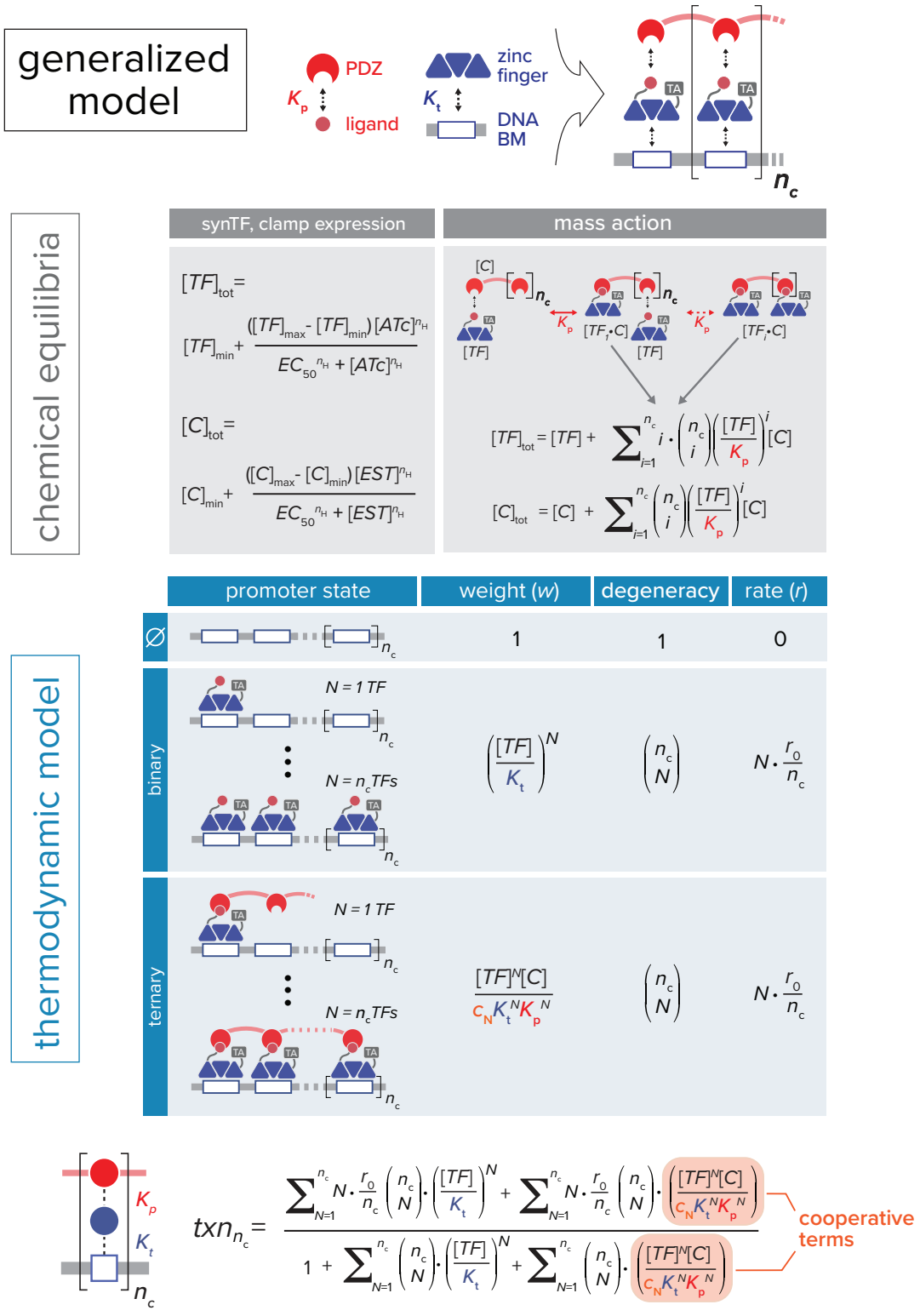

Figure S8. Generalized thermodynamic model for synTF/clamp complex assembly. The n_c=2 model of **Figure S7** is generalized for synTF/clamp complexes of arbitrary size. (*N* = the number of promoter-bound synTFs; n_c = total number of DNA binding sites; c_N = cooperativity constant that defines the additional stability the clamp gives to a complex of *N*-bound synTFs)

A

thermodynamic model parameter fitting

	experimentally-measured values	model-fitted values
K_t values (ZF 43-8-DNA affinities) - *from fig. S2*		
high <--> DBM 1	6.5 nM	9.9 nM
low <--> DBM 1	13.6 nM	11.5 nM
low <--> DBM 2	143 nM	572 nM
K_p values (syntrophin-ligand affinities) - *from fig. S3*		
ligand S6	20.3 μM	27.5 μM
ligand S5	1.97 μM	2.05 μM
ligand S4	0.88 μM	0.40 μM
Effective *in vivo* protein concentrations		
$[TF]_{max}$	-	26.7 nM
$[C]_{max}$	-	129.6 nM

B

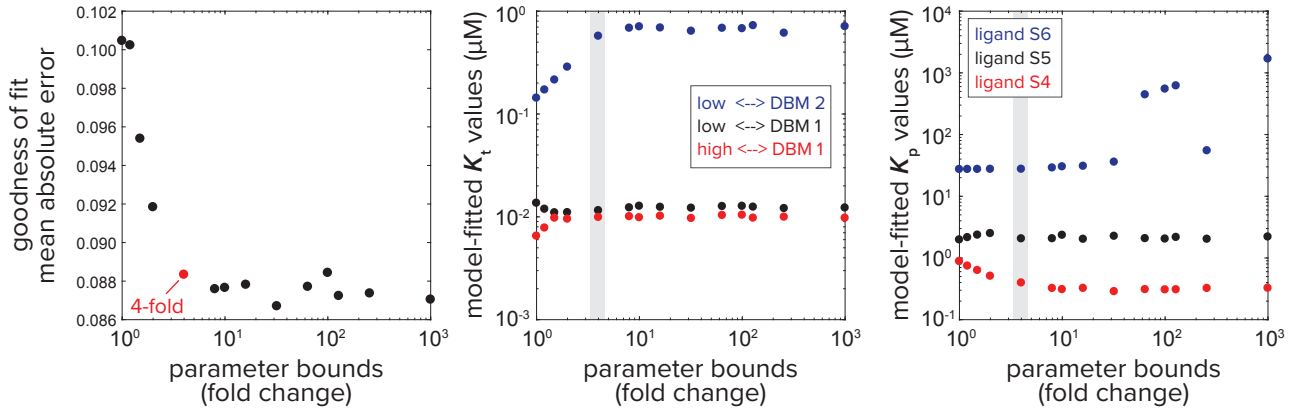

Figure S9. Summary of thermodynamic model parameters. (a) Comparison of experimentally-measured and model-fitted parameter values. Interaction affinities (ZF-DNA, PDZ-lig) were measured using *in vitro* binding assays (see **Materials and Methods**, **Figures S2-3**). Expression parameters were obtained using dose response measurements of the ncTET and ncZEV expression systems (see **Figure S4**). Fitted parameters were obtained by performing a global fit on a set of experimental data of two-input circuits (see **Figures 1D,E**). The two-input circuits consisted of ncTET and ncZEV driving expression of synTF and clamp (for different n_c, K_t, and K_p), with complex formation inducing expression of GFP. **(b)** Goodness of fit, evaluated by mean absolute error, between model and data for different choices of parameter fitting bounds on affinity values (left). A 4-fold bound was used in our model fits (highlighted in red). Model-fitted affinity values for K_t (middle) and K_p (right) for different choices of parameter fitting bounds (4-fold bound is highlighted in grey).

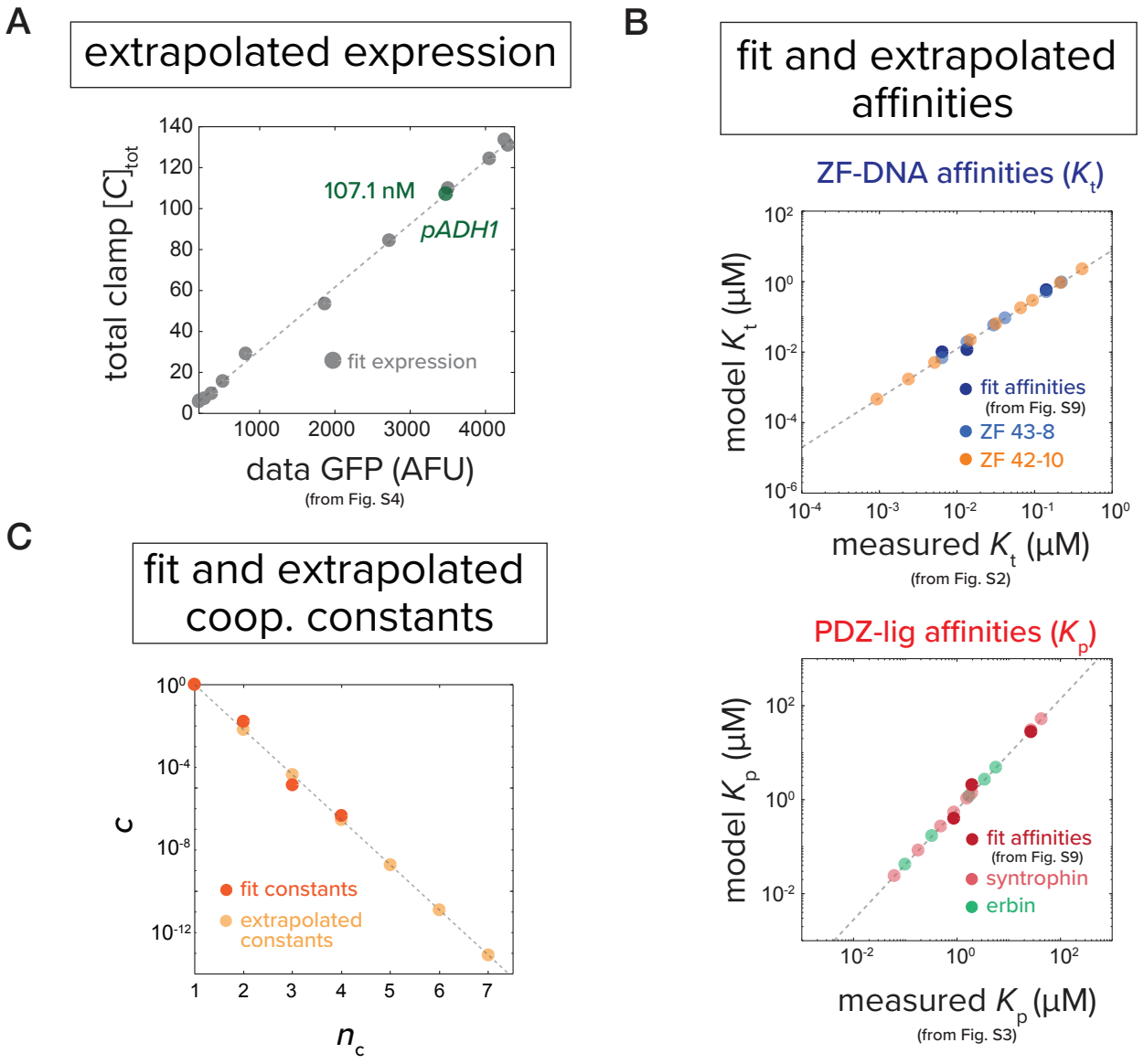

Figure S10. Transformation of experimentally measured values into *in vivo* parameter space. For parameter values associated with configurations used in the model fitting (**Figure 1e**), linear regression was used to model the relationship between experimentally measured values and corresponding fit-derived *in vivo* parameters (see **Figure S9**). Using fitted linear functions, interpolation was used to transform the remaining measured values (**Figures S2-4**). (**a**) Transformation of experimental expression data for *pADH1* into *in vivo pADH1*-clamp expression. We fit a linear function (grey line) to thermodynamic model fit-derived values for ncZEV clamp expression ($[C]_{tot}$, see **Figure S7**) at corresponding experimentally measured GFP expression levels (data from **Figure S4A**). From this, *in vivo* concentration for *pADH1*-expressed clamp was interpolated (green point) based on *pADH1*-GFP expression measured from the *LEU2* locus (**Figure S4A**). (**b**) Transformation of measured affinity values (K_t and K_p) into model parameter space. A log-log function (grey line) was used to model thermodynamic model fit-derived values for K_t and K_p affinity at corresponding experimentally measured affinities (see **Materials and Methods**, **Figures S2-3, S9**). Measured affinity values that were not associated with the thermodynamic model fit in **Figure 1E** were used to interpolate *in vivo* affinities. (**c**) Extrapolation of model-fitted clamp cooperativity constants (dark orange points) to infer constants for complexes with $n_c > 4$ (light orange). The extrapolation follows a log-linear relationship.

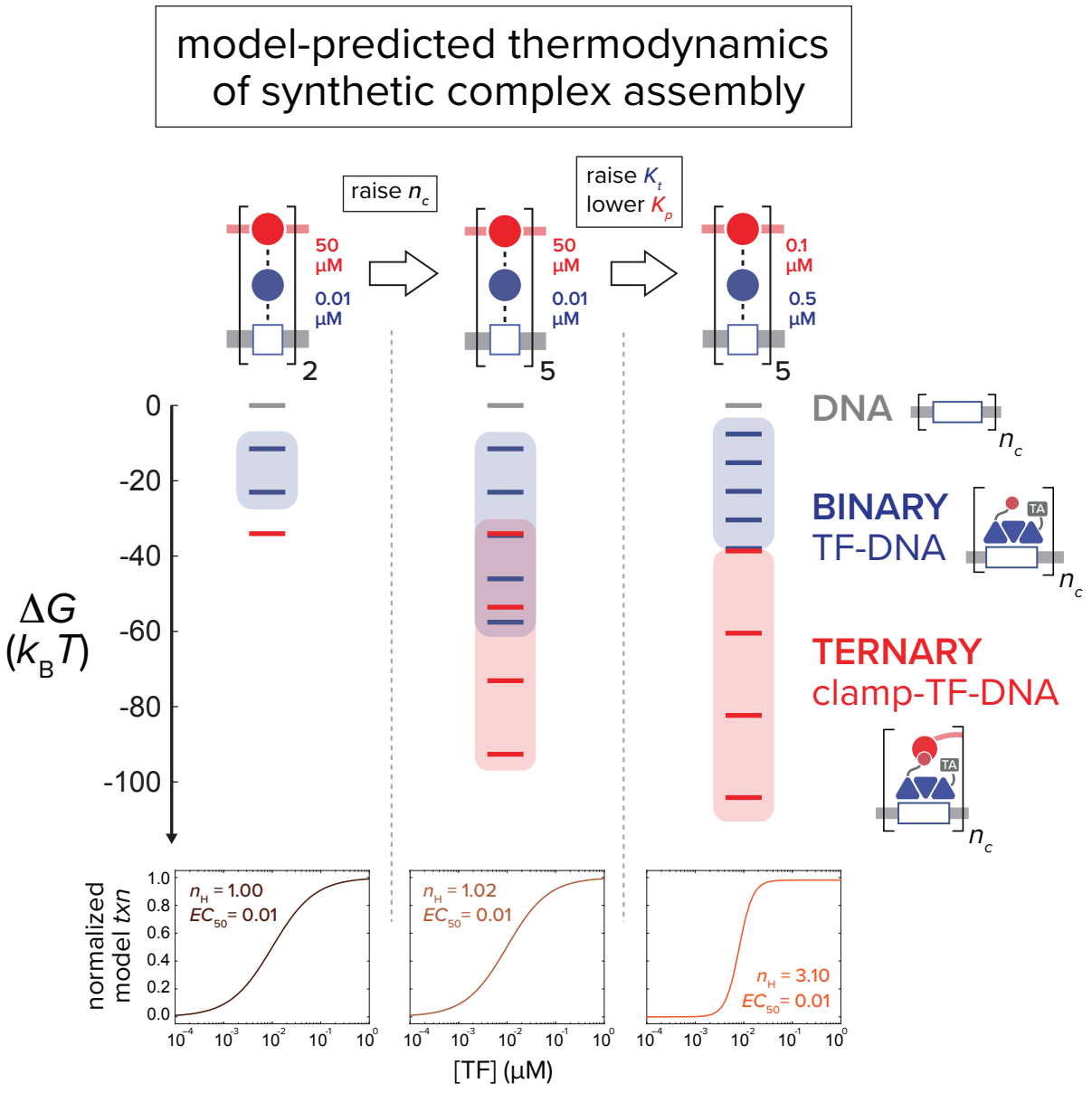

Figure S11. Thermodynamics of complex assembly in the generation of nonlinear dose response. The thermodynamic model (**Figures S7-9**) was used to simulate three different synTF/clamp configurations (n_c, K_t and K_p) predicted to have input/output responses progressing from non-cooperative to nonlinear (left to right). Free energy diagrams below each configuration depict relative free energies of the promoter states (grey are DNA-only states, blue are binary synTF-DNA states, and red are ternary synTF/clamp-DNA states). Below each free energy diagram is the simulated txn_n (see **Figure S8**) dose response of the assembly's transcriptional response when synTF species is titrated, and the corresponding EC_{50} ([*TF*] at half-maximal response) and n_H (Hill coefficient) for the dose response. Nonlinearity is increased by raising the complex valency (from n_c = 2 to 5), lowering synTF affinity for DNA (K_t), and raising affinity for clamp (K_p). These configuration changes are accompanied by an increased free energy separation between binary (blue) and ternary (red) states.

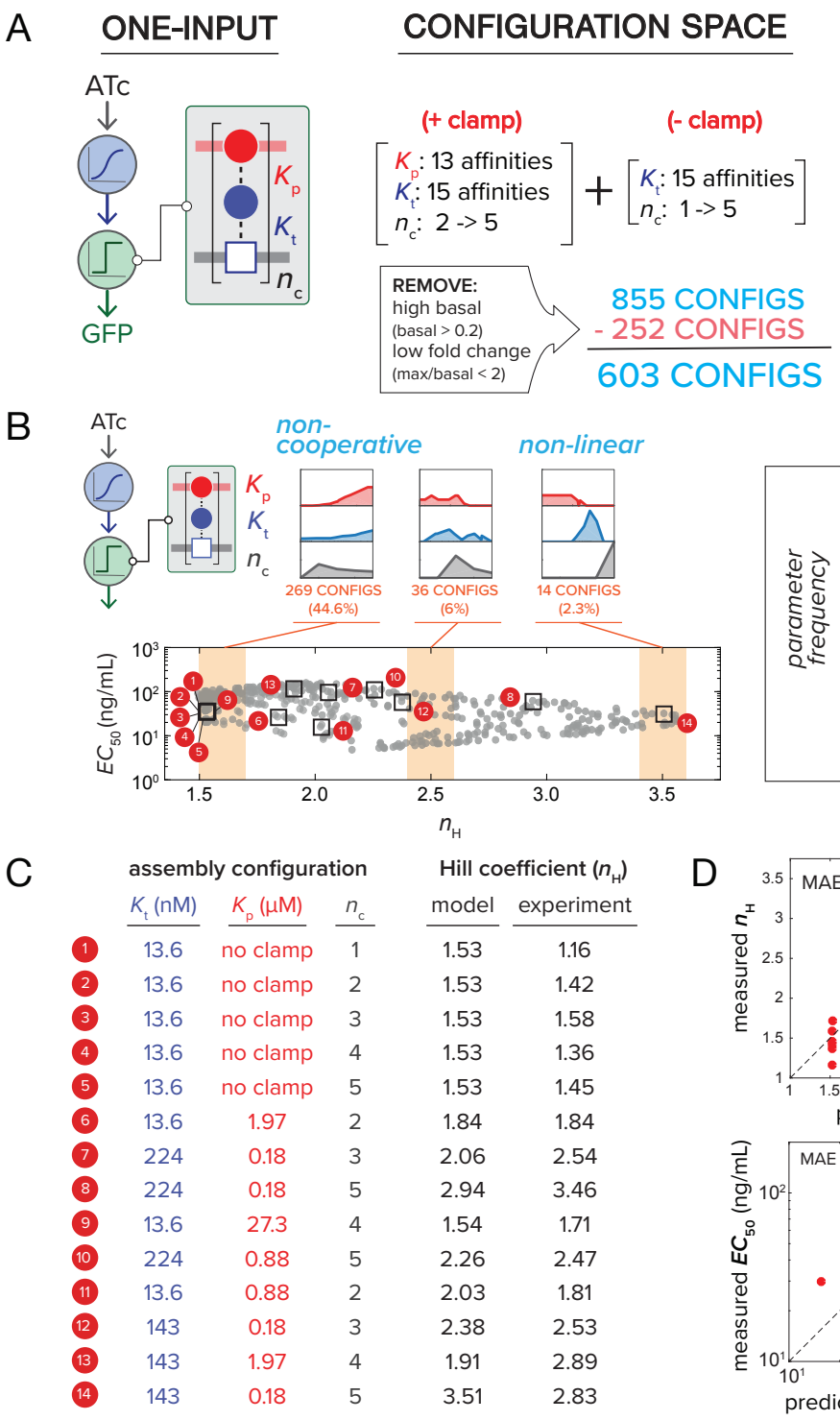

Figure S12. Using the model to explore cooperative complex modulation of dose response behavior. We used our thermodynamic model to map circuit dose response behavior onto configuration space for a single-input, two-node circuit where output is regulated by cooperative complex assembly. (**a**) Defining configuration space. ATc induces expression of a synTF (from the ncTET promoter), which forms an assembly with constitutively expressed clamp (*pADH1*), driving GFP reporter expression (left). Enumeration of available configurations for this assembly (855) and curation (removal of unproductive configurations) resulted in a final set of 603 (right). Using the model, dose responses were simulated for each configuration ([ATc] range = 10^{-1} - 10^{4} ng/mL). Hill functions were fit to extract EC_{50} ([ATc] at half-maximal response) and n_H (Hill coefficient) values for each dose response. (**b**) The single-input behavior space of EC_{50} vs. n_H. Each point corresponds to a specific circuit configuration (scatter). Above the morphospace is a parameter frequency analysis of values of (K_p, K_t, n_c) for three different regions of the scatter, corresponding to non-cooperative (left orange box), nonlinear (center box), and highly nonlinear responses (right box). Shown to the right is the range of values for each parameter's frequency analysis distribution. A set of circuit configurations (red circles) distributed throughout the behavior space were constructed and used to experimentally test the model predicted dose response behaviors. **(c)** Table summarizing the 14 circuit configurations highlighted in (**b**), and their corresponding model-predicted and experimentally-obtained n_H values. (**d**) Correlation between model predictions and experimental data for the 14 circuit configurations. The top scatter compares n_H, while the bottom compares EC_{50}. MAE = mean absolute error.

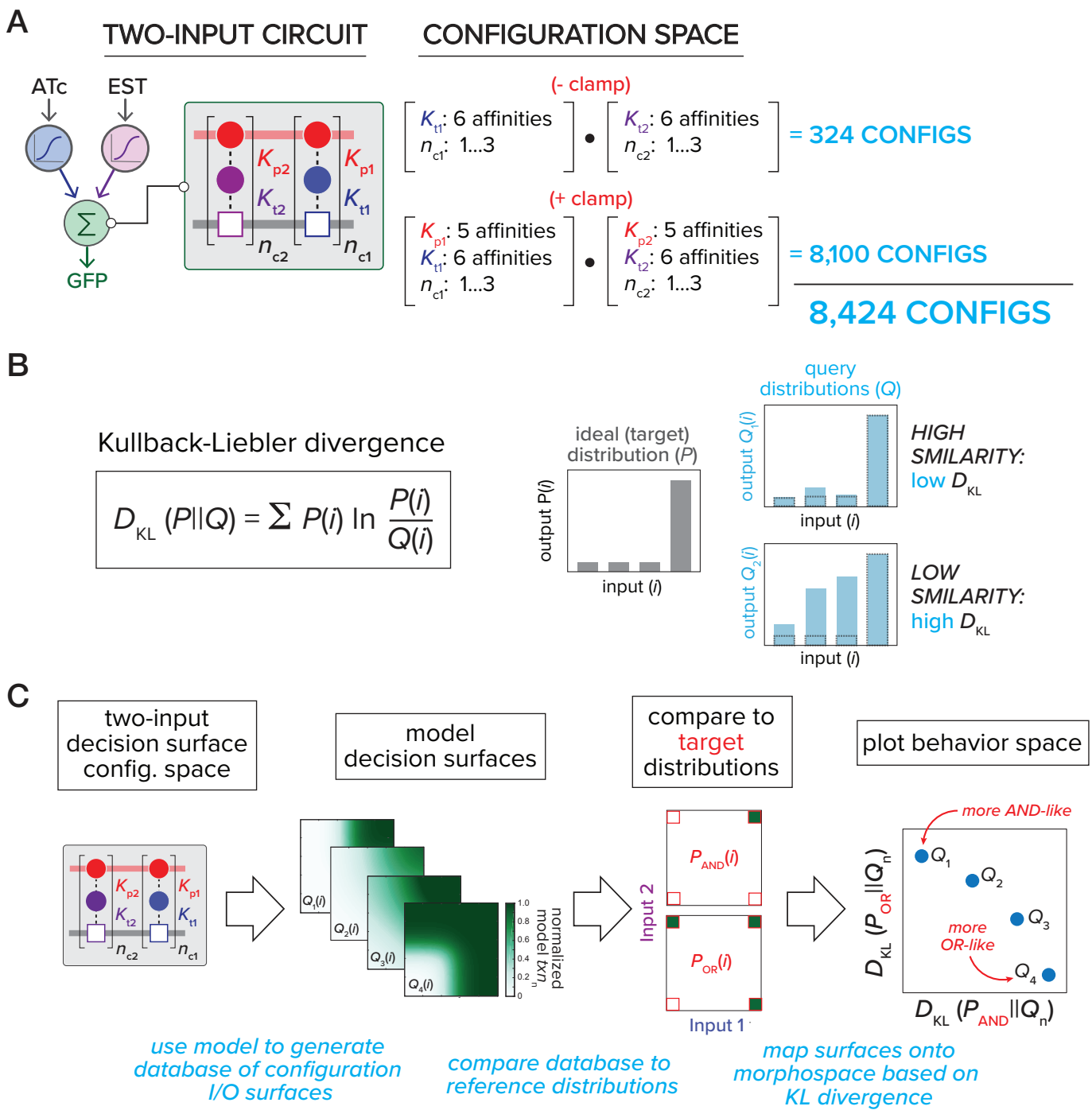

Figure S13. Computationally probing the relationship between cooperative complex configuration and two-input logic. We used our thermodynamic model to map dose response behavior onto configuration space for a two-input circuit, where output is regulated by assembly of two synTFs and a clamp (see **Figure 2B**). (**a**) For the two-input circuit, ATc and EST induce expression of two different synTFs (from the ncTET and ncZEV promoters), while clamp expression is driven by *pADH1*. Enumerated configuration search space for the circuit (right) includes configurations with and without clamp. (**b**) Method for scoring circuit behavior based on an information theory-based comparison with an ideal (target) behavior. Kullback-Liebler divergence (D_{KL}) uses informational entropy to measure the difference between two distributions: e.g., a reference distribution (P) representing a target behavior and a distribution (Q) representing query data. Lower D_{KL} values signify distributions that are more "similar" to the target. (**c**) Computational workflow for analyzing two-input logic behavior space. Progressing from left to right: for each configuration in the search space, normalized model transcriptional output (txn_n) is simulated across ranges of [ATc] (96 data points, 10^{-1} - 10^4 ng/mL) and [EST] (96 data points, 0.5-12.5 nM). Each member of the resulting decision surface database ($Q_1(i)$, $Q_2(i)$, $Q_3(i)$, etc.) is then compared to two ideal (target) distributions: a two-input AND gate ($P_{AND}(i)$) and an OR gate ($P_{OR}(i)$). Specifically, $D_{KL}(P_{AND}||Q_n)$ and $D_{KL}(P_{OR}||Q_n)$ are evaluated by comparing the four corner regions (red search area boxes, 12 x 12 data points) of each model surface to those of the target AND and OR distributions, respectively. The full set of $D_{KL}(P_{AND}||Q_n)$ and $D_{KL}(P_{OR}||Q_n)$ were plotted to generate a behavior space representing the degree to which each circuit configuration is AND-like or OR-like (see **Figure 2B**).

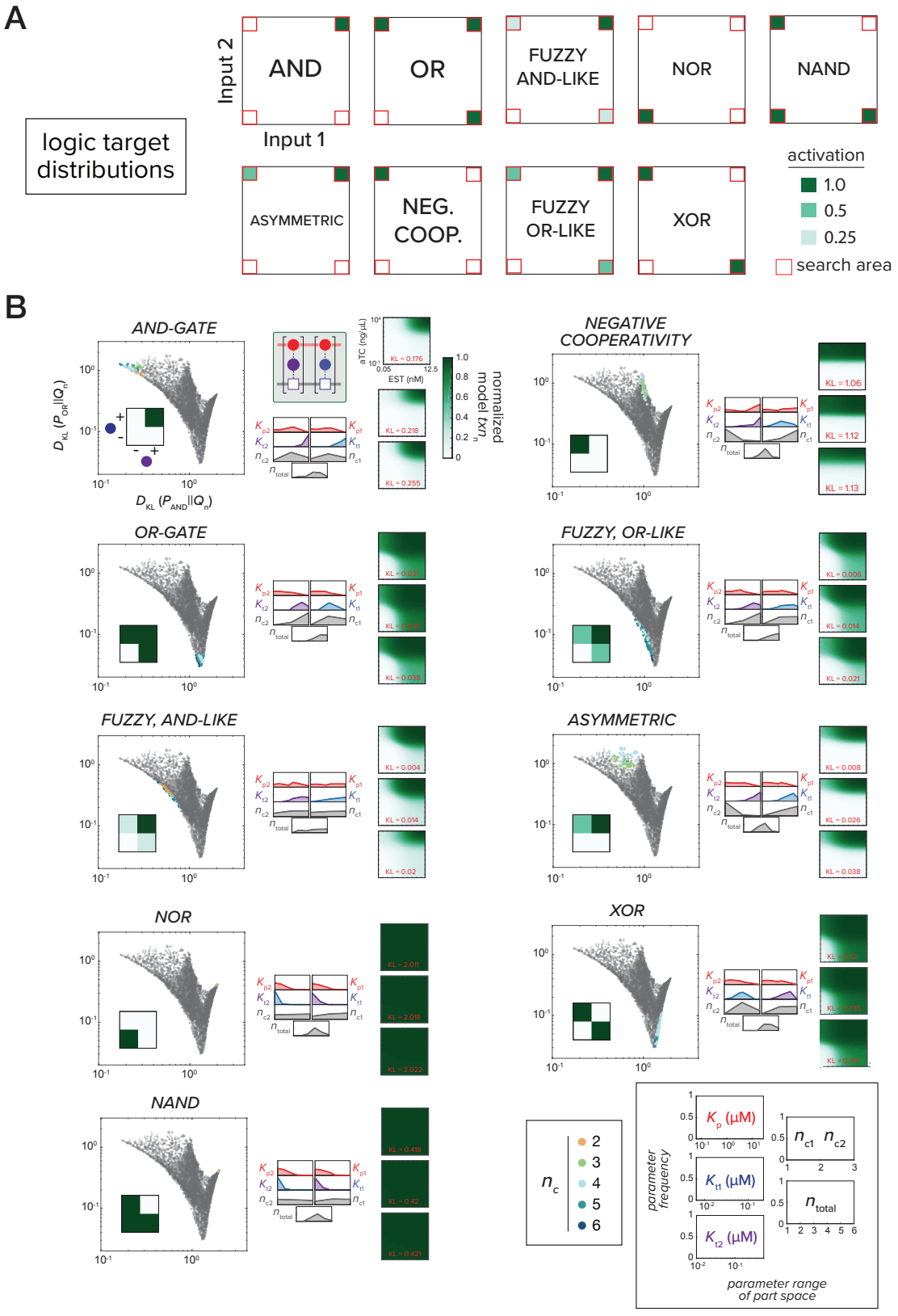

Figure S14. Mapping logic behavior onto two-input morphospace. (**a**) The set of ideal logic (target) distributions. Target distributions were defined by assigning normalized transcriptional activation values (1, 0.5, 0.25, 0) to the four corners of the distribution, where each corner is composed of 12 x 12 points (search area, red squares). The search areas of model-predicted decision surfaces can then be compared against these target logic distributions using D_{KL} as described in **Figure S13C**. (**b**) Identifying areas of morphospace enriched for desired two-input logic functions. For a given logic function (scatter inset: AND, OR, etc.), we evaluated D_{KL} for all configurations in the morphospace. Highlighted within each morphospace are the top 1% of configurations (lowest D_{KL}) corresponding to the target logic function. The color of the highlighted configurations indicates complex size (n_c, bottom right). Parameter frequency analyses of (K_p, K_t, n_c) for highlighted configurations are shown to the right of the morphospace, along with three example decision surfaces (parameter frequency key is shown on the bottom). (dark grey scatter points = configurations with clamp)

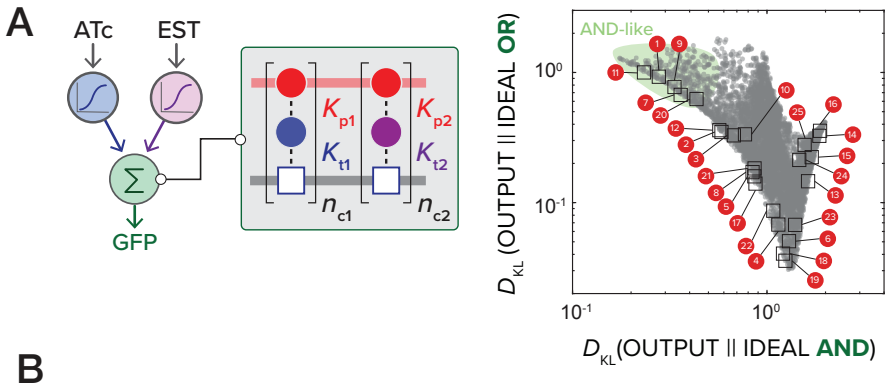

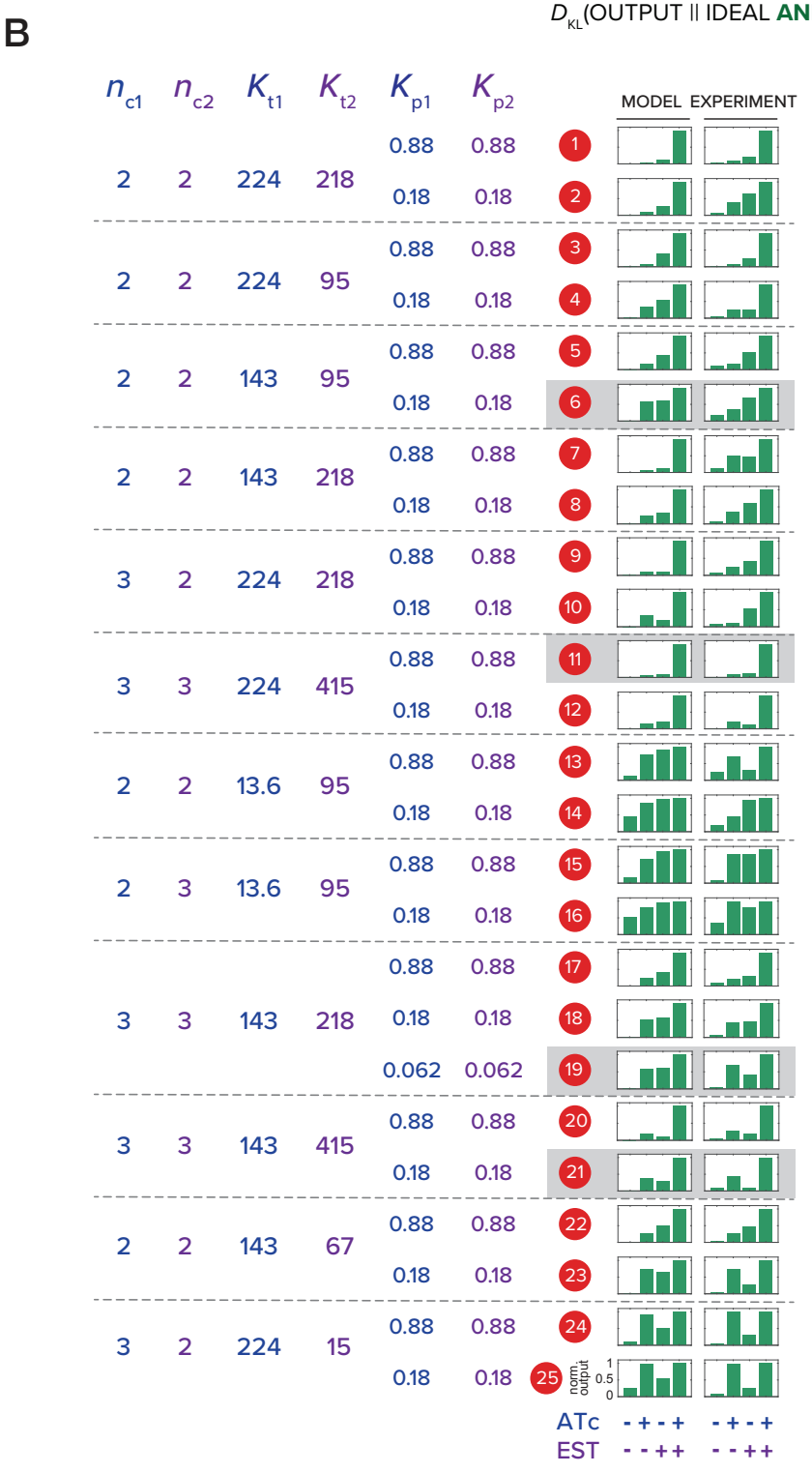

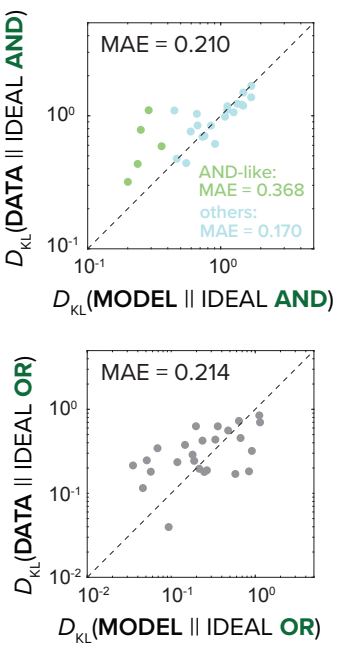

Figure S15. Experimental verification of two-input circuit behavior space. **(a)** A set of circuits were constructed to test the ability of our model to predict steady state behavior for two-input circuits containing two differen synTF species (left). We selected circuits broadly distributed throughout the predicted behavior space (right), including within regions thought to contain boolean-like behavior (AND- and OR-gates). Circuits were induced with saturating concentrations of ATc and EST, grown for 18h, and measured by flow cytometry. **(b)** Model and experimental fluorescence values were normalized to calculated and observed maximum outputs. Circuit configurations highlighted in grey are shown in **Fig. 2C**. **(c)** Correlation betwen model predictions vs. experimental data for two-input circuits. The top scatter compares divergence (D_{KL}) of model and data to an ideal AND-gate, while the bottom compares divergence (D_{KL}) of model and data to an ideal OR-gate. D_{KL} is computed as described in **Figure S13**. MAE = mean absolute error. Green points and corresponding MAE refer to five configurations predicted to have the best AND-like logic. Blue points and MAE refer to all other configurations.

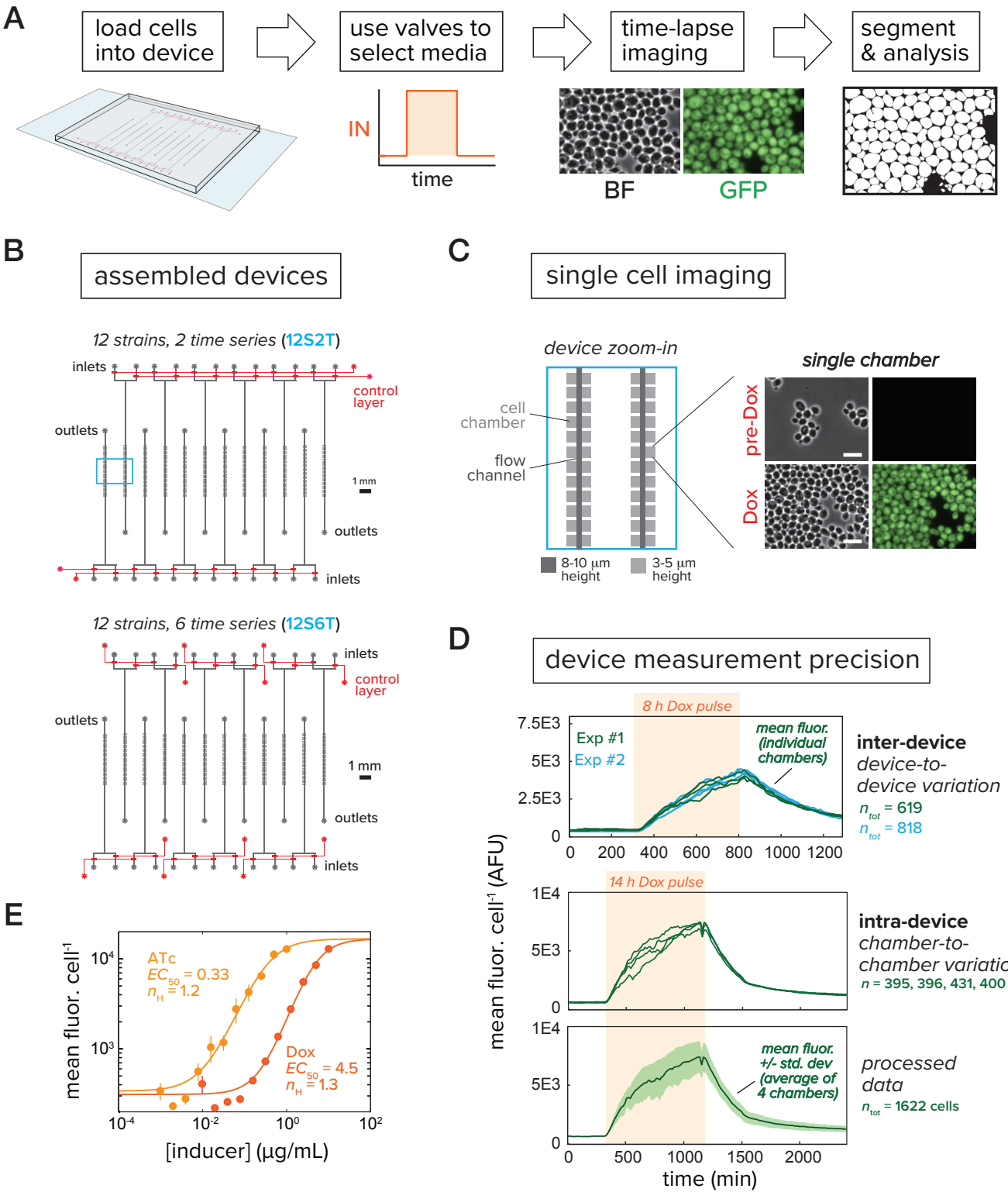

Figure S16. Microfluidic devices and methods for time-lapse experiments. (**a**) Workflow for microfluidic experiments. Yeast cells are loaded into a device, on-chip valves are used to select media and specify an induction time series, cells are imaged using time-lapse microscopy, and image analysis is performed to extract single-cell fluorescence trajectories. (**b**) Schematic of the multi-layer microfluidic devices used in this study, where flow layers are shown in grey and control layers in red. Cells loaded from inlets are trapped in cell chambers that have been fabricated to the height of a single monolayer of *S. cerevisiae* cells (light blue box, magnified in c). (**c**) Magnified view of the cell trapping chambers (left). Representative bright field and GFP images of the ncTET-GFP strain before and after Dox induction (right). Scale bar, 10 μm. (**d**) The variation in single-cell fluorescence trajectories measured in cells across different devices (inter-device, top) and different cell chambers (intra-device, middle). Fluorescence trajectories shown throughout this study represent the mean and standard deviation of many cells aggregated from multiple cell chambers (bottom). Dox was used at 10 μg/mL. (**e**) Dose response curves for the ncTET expression system using the inducers ATc and Dox. Because of ATc photodegradation, Dox was used in all microfluidic time-lapse experiments.

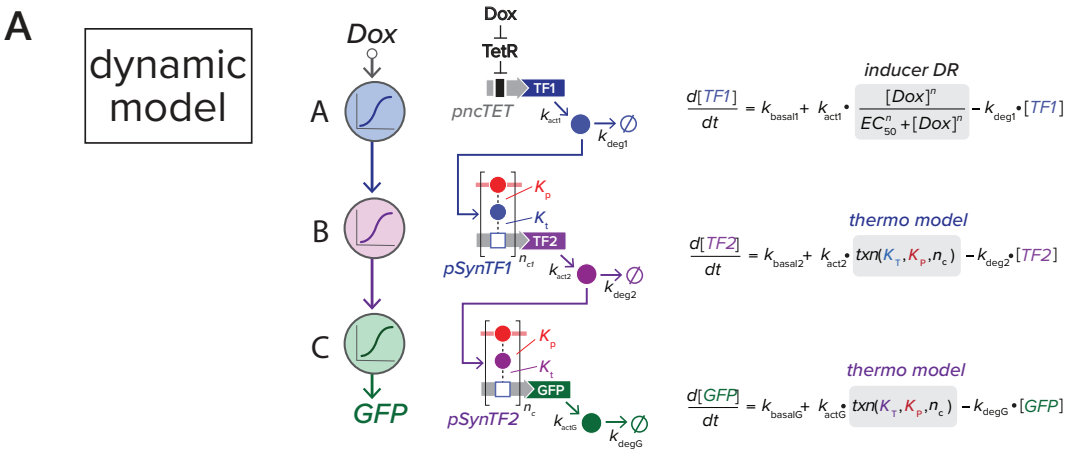

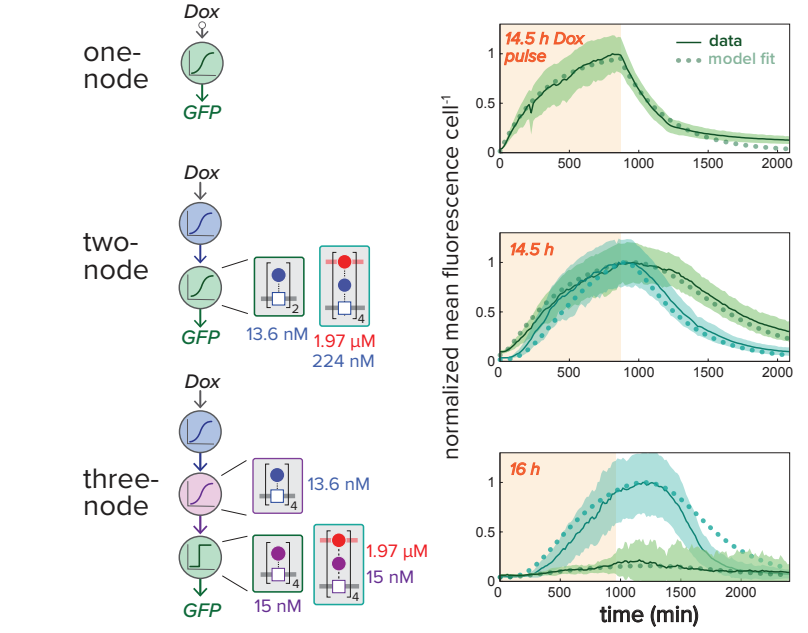

FITTED CONSTANTS

promoter activation rates

1 node

- k_{actG} (pncTET) = 26.51 min^{-1}

2 node

- k_{act1} (pncTET) = 4.21•10^{-4} µM•min^{-1}
- k_{actG} (pSynTF1) = 20.95 min^{-1}
- k_{basal1} = 4.5•10^{-6} µM•min^{-1}
- k_{basalG} = 0.3 min^{-1}

3 node

- k_{act1} (pncTET) = 4.21•10^{-4} µM•min^{-1}
- k_{act2} (pSynTF1) = 1•10^{-5} µM•min^{-1}
- k_{actG} (pSynTF2) = 16.96 min^{-1}
- k_{basal1} = 4.5•10^{-6} µM•min^{-1}
- k_{basal2} = 1.1•10^{-8} µM•min^{-1}
- k_{basalG} = 0.3 min^{-1}

protein properties

- GFP: k_{degG} = 0.0030 min^{-1}
- TF1: k_{deg1} = 0.0045 min^{-1}
- TF2: k_{deg2} = 0.0045 min^{-1}

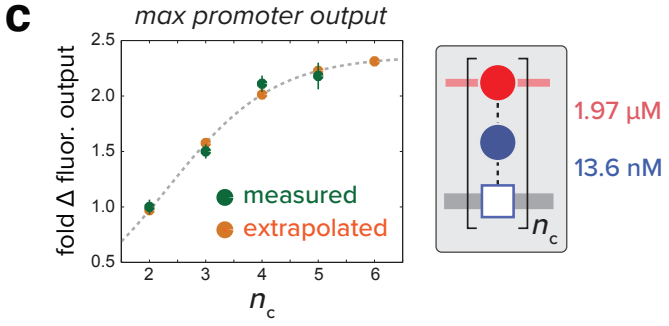

Figure S17. Experimental parameterization of dynamic model for circuits composed of synTF assemblies. (a) Application of the dynamic model to a three-node circuit (cascade). Dox-induced ncTET expression of TF1 from the first node assembles with constitutively expressed clamp (*pADH1*) at the second node, inducing expression TF2, which subsequently assembles with clamp to drive expression of GFP at the third node (left). Corresponding rate equations describe the change in species concentrations over time (right). ncTET expression of synTF1 is modeled with a Hill equation ("inducer DR" grey box). For downstream *(DBM)miniCyc1* promoters that are regulated by synTF assemblies, such as pSynTF1 and pSynTF2, the thermodynamic model is used to compute the species production rate ("thermo model" grey boxes). k_{act} = maximum transcriptional activation rate for each promoter; k_{basal} = basal promoter activity; k_{deg} = degradation/dilution rate of each protein. **(b)** Fitting dynamic model to time course data. Rate parameters were obtained from a global fit of the model to microfluidic time course data of strains harboring one-node, two-node, and three-node test circuits (subjected to a Dox pulse of 14.5 or 16 h). Specific circuit configurations are shown to the left, fits (dots) to the experimental data (lines) are on the right, and the extracted rate constants are below. **(c)** A relationship for scaling promoter activation rates, k_{act}, as a function of synTF complex size, n_c. Maximum fluorescence outputs were measured for two-node cascades having identical assembly configuration (shown to the right), but with n_c = 2-5 (fold change is relative to maximum output for n_c = 2 configuration). The data were fit to a logistic function, and used to extrapolate k_{act} values for assemblies of arbitrary size.

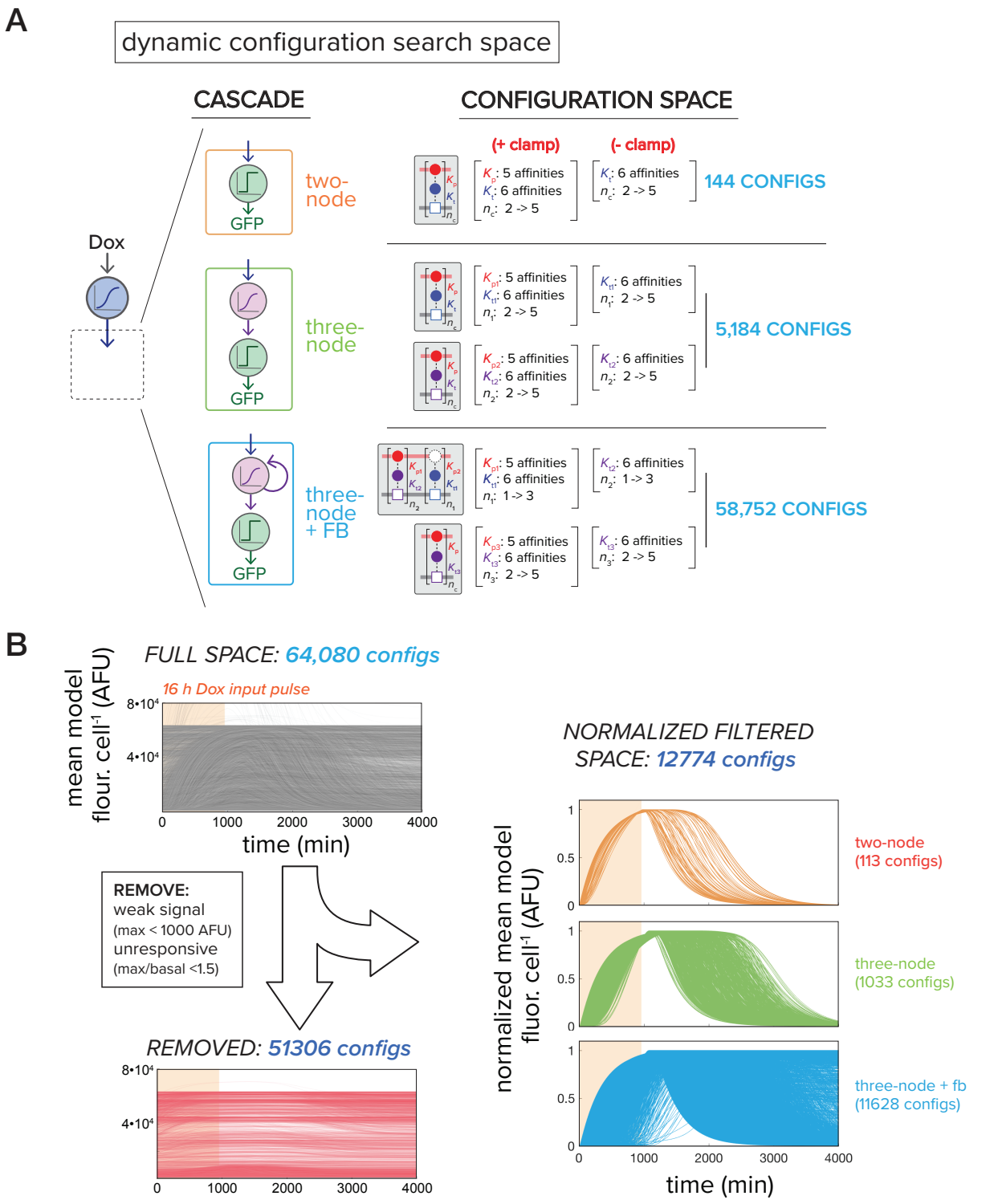

Figure S18. Model-based construction of the circuit activation/deactivation behavior space. We used our model to map behavior space for activation/deactivation kinetics from assembly configuration space for two-node, three-node, and three-node with feedback (+FB) circuits (see also **Figure 3B**). (**a**) For all circuits, ATc (or Dox) is the input, inducing ncTET expression of a synTF, which assembles with constitutively expressed clamp (*pADH1*) to drive expression of either GFP (two-node) or a second synTF (three-node and three-node+FB). The second synTF assembles with clamp to drive GFP expression and its own production (for three-node+FB) (left). Enumeration of the configuration search space for these circuits (right). This space includes configurations with and without clamp. (**b**) Simulation and curation of output traces for circuit configuration space. We used the model to simulate GFP output traces for the full space of circuit configurations in response to a 16 h Dox pulse (10 µg/mL) (grey, full space). Traces with weak basal or low fold activation (red) were filtered out, and the remaining traces normalized between 0 and 1 (orange, green, blue).

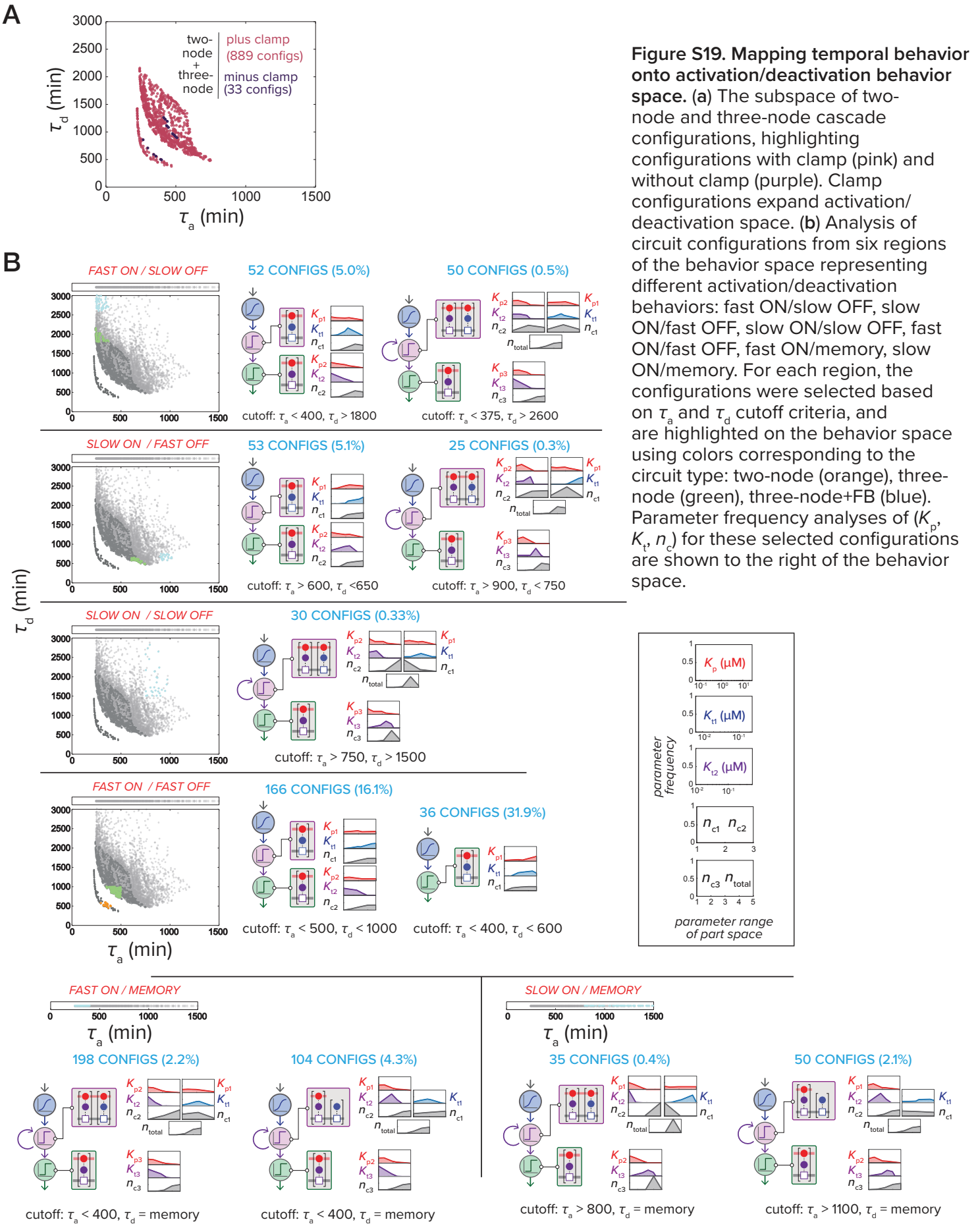

Figure S19. Mapping temporal behavior onto activation/deactivation behavior space. (**a**) The subspace of two-node and three-node cascade configurations, highlighting configurations with clamp (pink) and without clamp (purple). Clamp configurations expand activation/deactivation space. (**b**) Analysis of circuit configurations from six regions of the behavior space representing different activation/deactivation behaviors: fast ON/slow OFF, slow ON/fast OFF, slow ON/slow OFF, fast ON/fast OFF, fast ON/memory, slow ON/memory. For each region, the configurations were selected based on τ_a and τ_d cutoff criteria, and are highlighted on the behavior space using colors corresponding to the circuit type: two-node (orange), three-node (green), three-node+FB (blue). Parameter frequency analyses of (K_p, K_t, n_c) for these selected configurations are shown to the right of the behavior space.

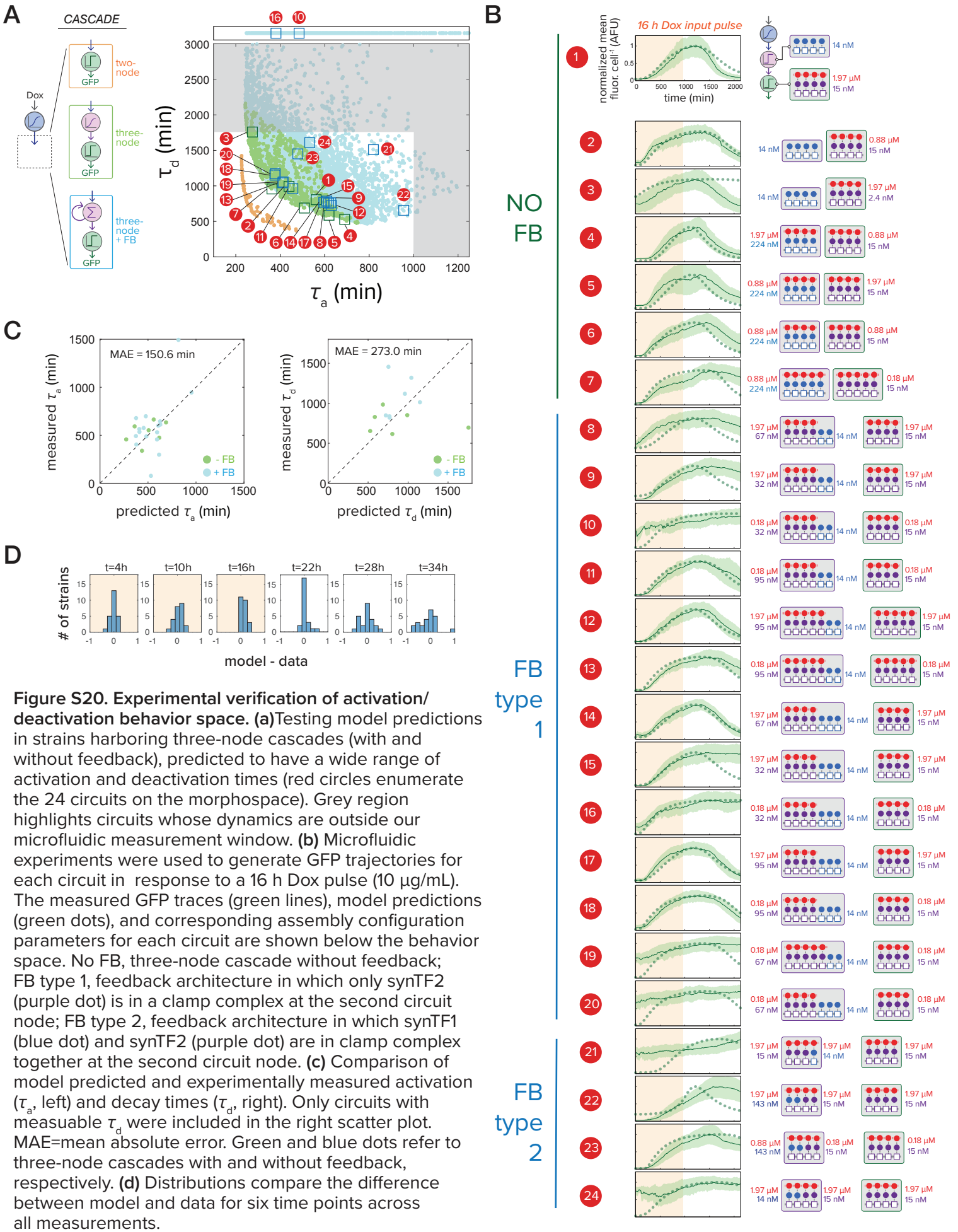

Figure S20. Experimental verification of activation/deactivation behavior space. (a) Testing model predictions in strains harboring three-node cascades (with and without feedback), predicted to have a wide range of activation and deactivation times (red circles enumerate the 24 circuits on the morphospace). Grey region highlights circuits whose dynamics are outside our microfluidic measurement window. **(b)** Microfluidic experiments were used to generate GFP trajectories for each circuit in response to a 16 h Dox pulse (10 µg/mL). The measured GFP traces (green lines), model predictions (green dots), and corresponding assembly configuration parameters for each circuit are shown below the behavior space. No FB, three-node cascade without feedback; FB type 1, feedback architecture in which only synTF2 (purple dot) is in a clamp complex at the second circuit node; FB type 2, feedback architecture in which synTF1 (blue dot) and synTF2 (purple dot) are in clamp complex together at the second circuit node. **(c)** Comparison of model predicted and experimentally measured activation (τ_a, left) and decay times (τ_d, right). Only circuits with measuable τ_d were included in the right scatter plot. MAE=mean absolute error. Green and blue dots refer to three-node cascades with and without feedback, respectively. **(d)** Distributions compare the difference between model and data for six time points across all measurements.

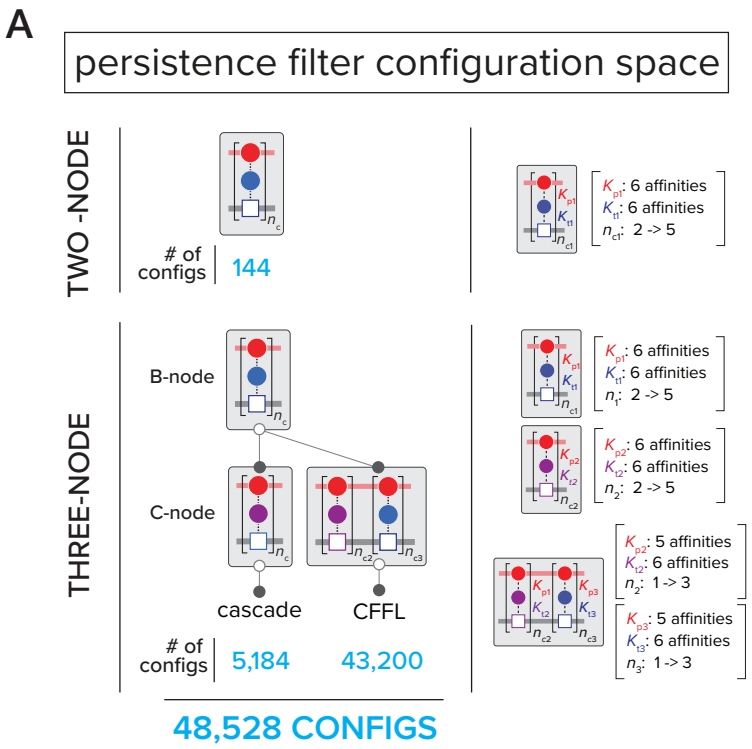

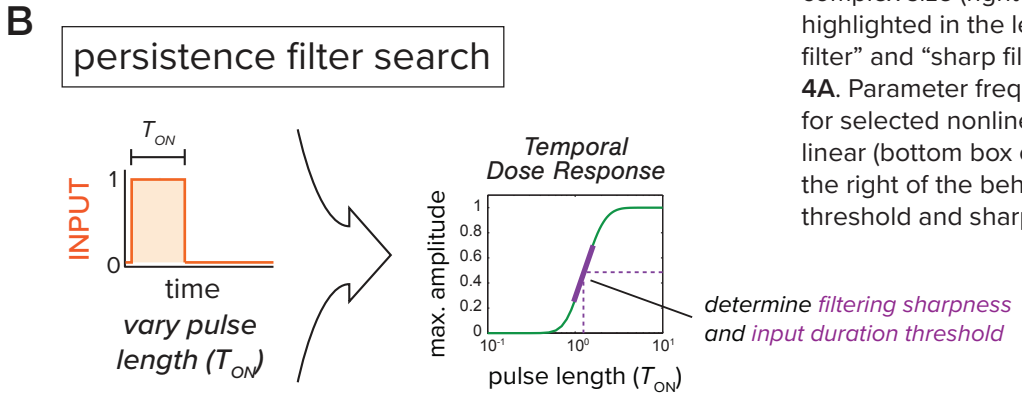

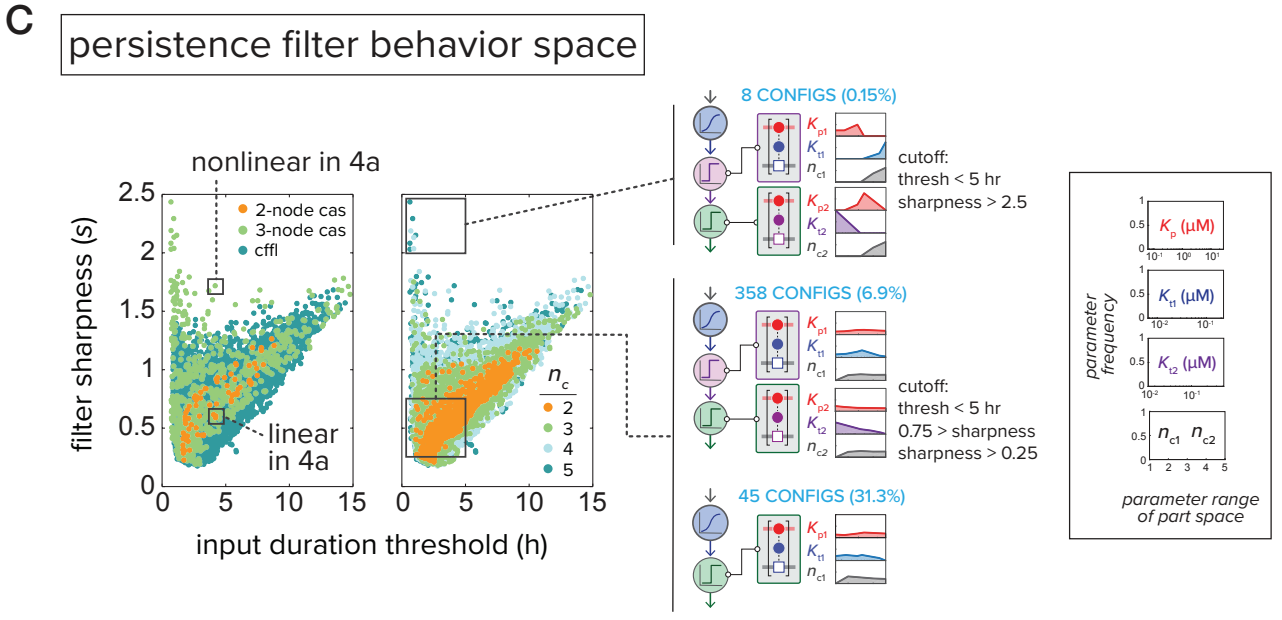

Figure S21. Model-based search and analysis of persistence filtering. (**a**) Enumeration of configuration search space used for persistence filtering. The space includes two-node and three-node cascades and coherent feed-forward loop (CFFL) circuits. (**b**) Computational search for circuits that perform persistence filtering. For each configuration, we used the model to simulate output traces in response to a Dox pulse of varying lengths (T_{ON} = 30 - 3000 min) (left). A "temporal dose response" curve is generated for each circuit configuration by plotting maximum output amplitude for each pulse length, and used to obtain two filtering metrics: the pulse length threshold (input duration at half-maximal response) and filtering sharpness (slope at threshold) (right). (**c**) Analysis of behavior space of persistence filtering behavior: input duration threshold vs. filter sharpness (*s*) for each circuit configuration in the search. Examination of behavior space as a function of circuit type (left scatter) and synTF/clamp complex size (right scatter). Configurations highlighted in the left scatter are the "linear filter" and "sharp filter" circuits shown in **Figure 4A**. Parameter frequency analyses of (K_p, K_t, n_c) for selected nonlinear (top box callout) and linear (bottom box callout) filters are shown to the right of the behavior space, along with threshold and sharpness selection criteria.

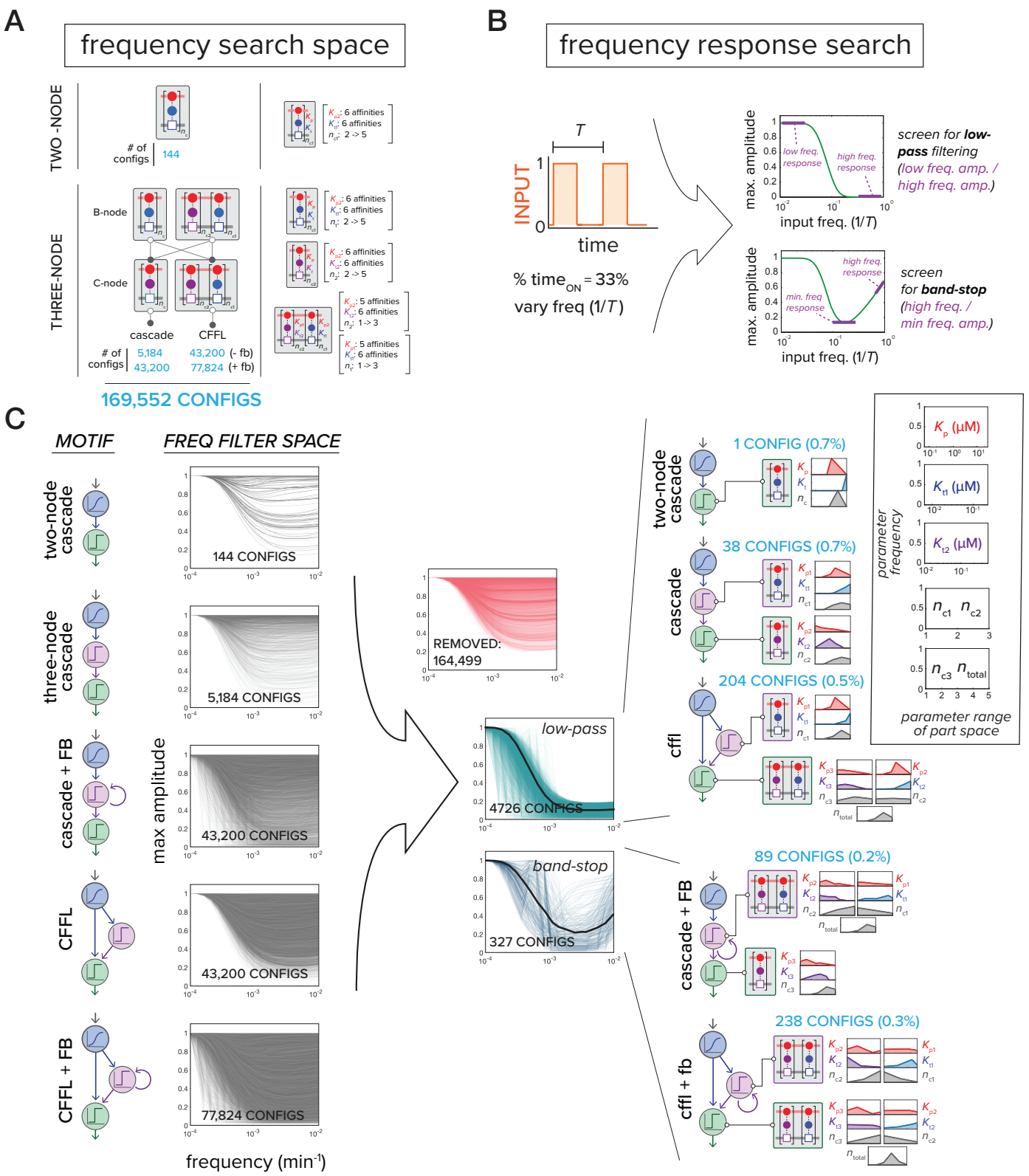

Figure S22. Model-based search and analysis of frequency filtering behaviors. (**a**) Enumeration of configuration search space used for frequency filtering. The space includes two-node and three-node cascades (+/- feedback) and coherent feed-forward loop (CFFL) circuits (+/- feedback) . (**b**) Searching the configuration space for frequency filtering target behaviors: low-pass and band-stop filters. For each circuit configuration, the model was used to simulate output traces in response to periodic Dox pulses of varying frequency (periods ranging from T = 90 to 9000 min) (left). Maximum amplitudes of the resulting traces are used to construct frequency response curves for each circuit (right). Low-pass and band-stop filters are then screened based on two different metrics extracted from this curve: the ratio of low to high frequency amplitudes (low/high freq. gain, low-pass) and the ratio of minimum to high frequency amplitudes (min/high freq. gain, band-stop). (**c**) Computational screen and analysis of low-pass and band-stop filtering circuit configurations. Progressing from left to right: We searched a configuration space corresponding to five circuit motifs. Frequency response curves were generated for the full configuration space, and binned into low-pass (green curves, low/high freq. gain > 5) or band-stop (blue and orange curves, min/high freq. gain > 2). Circuit configurations not meeting either criteria were discarded (red curves). Parameter frequency analyses of (K_p, K_t, n_c) for the selected configurations are shown to the right. Bold black curves show the predicted response of circuit configs in **Fig. 4B**.

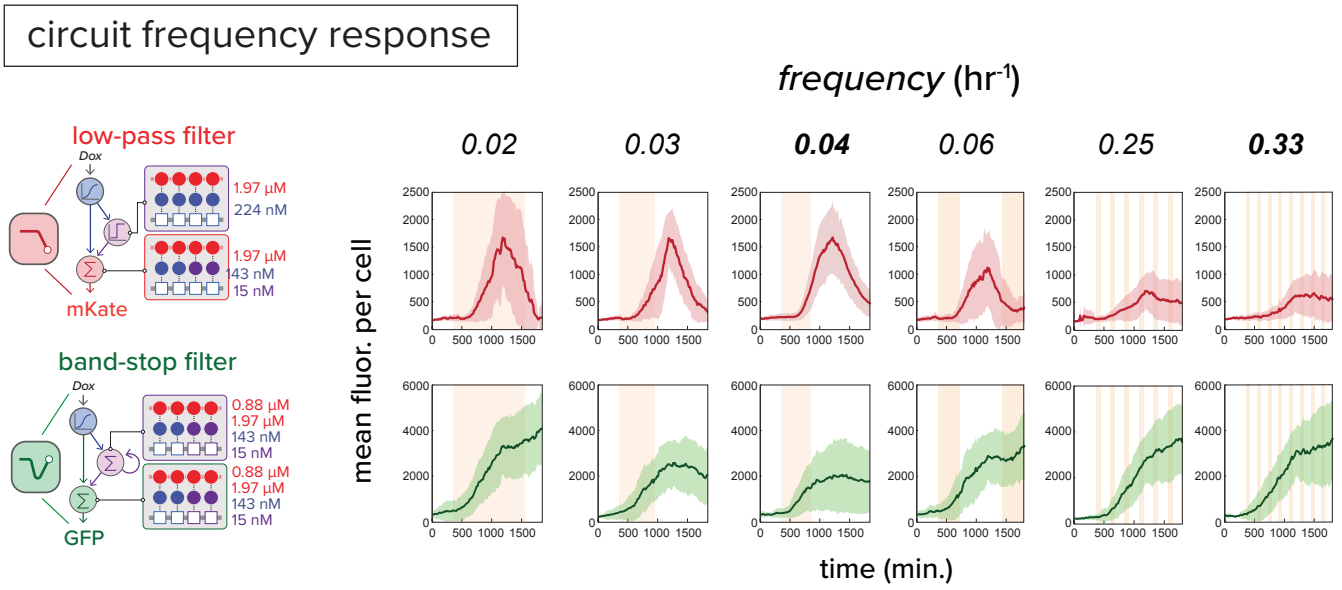

Figure S23. Experimental verification of frequency response behavior of low-pass and band-stop filter circuits. Circuit configurations computationally predicted to display low-pass (red) and band-stop (green) filtering were constructed (**left**), and their frequency responses were experimentally obtained using microfluidic experiments (**right**). Strains harboring the low-pass and band-stop circuits, driving expression of mKate and GFP respectively, were co-cultured in the 12S6T device (**Fig. S16B**), and subjected to periodic square wave pulses of Dox (10 µg/mL, 33% duty cycle) for different frequencies. mKate and GFP traces (mean and standard deviation) for each circuit. Frequencies in bold are the two frequency regimes highlighted in **Fig 4B**.

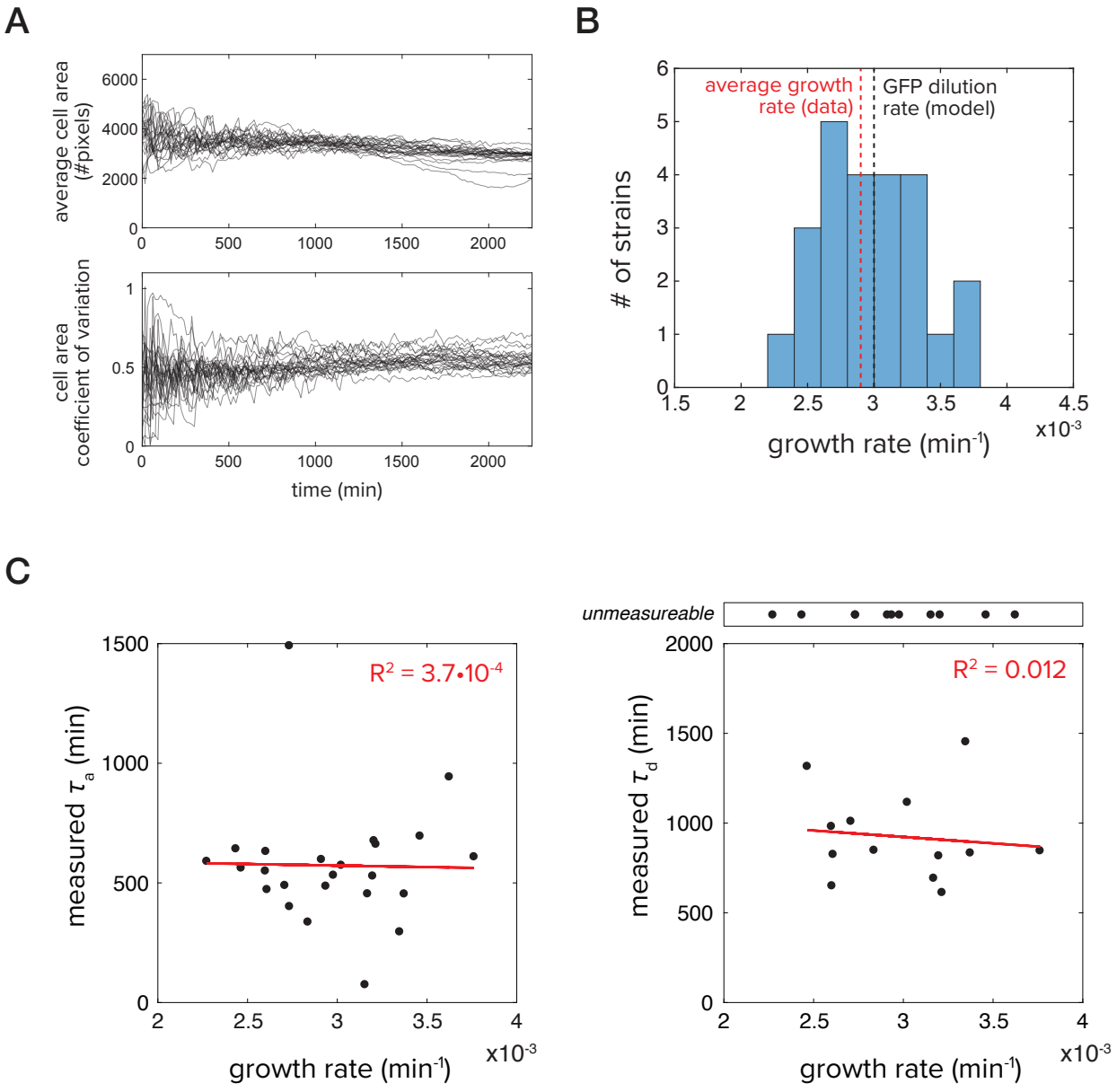

Figure S24. Quantification of cell size and growth rate for strains analyzed in microfluidic devices. (**a**) Mean cell area (top) and cell area coefficient of variation (bottom) quantified over time using segmentation software (CellTracer, see **Materials and Methods**) for all 24 strains analyzed in **Figure S20**. (**b**) Distribution of growth rates for all strains analyzed in **Figure S20**. Growth rates for each strain were calculated using cell counts at each time point. The average growth rate across all strains (0.0029 min^{-1}) is indicated (red dashed line), along with the model dilution rate for GFP (0.003 min^{-1}, black dashed line). (**c**) Comparison of average growth rate and circuit dynamics for all strains analyzed in **Figure S20**. Linear regression with associated r-squared values shown in red.

TABLE S1: Plasmid Table

FIGURE	PLASMID #	PARENT	PROMOTER	ORF
1C	**pCB342**	pMAL-c5	*Ptac*	MBP-43-8(low)-syn. lig.(S5)
	pCB348	pMAL-c5	*Ptac*	MBP-43-8(low)-syn. lig.(no bind)
	pCB376	pMAL-c5	*Ptac*	MBP-2x syn. clamp
	pCB428	pMAL-c5	*Ptac*	MBP-3x syn. clamp
1E	**pN8**	pRS406	*p(n_c=2, 43-8 DBM1)minCyc1*	GFP
	CB269	pRS406	*p(n_c=2, 43-8 DBM2)minCyc1*	GFP
	pCB277	pRS406	*p(n_c=3, 43-8 DBM1)minCyc1*	GFP
	pCB228	pRS406	*p(n_c=4, 43-8 DBM1)minCyc1*	GFP
	pCB298	pRS304	*pNcTET*	43-8(low)-syn. lig(S5)
	pCB300	pRS304	*pNcTET*	43-8(low)-syn. lig(S6)
	pCB302	pRS304	*pNcTET*	43-8(low)-syn. lig(S4)
	pCB706	pRS304	*pNcTET*	43-8(high)-syn. lig(S5)
	pN187	pRS605	*pNcZEV*	2x syn. clamp
	pCB397	pRS605	*pNcZEV*	3x syn. clamp
	pCB398	pRS605	*pNcZEV*	4x syn. clamp
2B	**pCB707**	pRS406	*p(n_c=1, 43-8 DBM1)minCyc1*	GFP
	pN8	pRS406	*p(n_c=2, 43-8 DBM1)minCyc1*	GFP
	pN18	pRS406	*p(n=3, 43-8 DBM3)minCyc1*	GFP
	pCB280	pRS406	*p(n=5, 43-8 DBM3)minCyc1*	GFP
	pCB281	pRS406	*p(n_c=5, 43-8 DBM2)minCyc1*	GFP
	pCB298	pRS304	*pNcTET*	43-8(low)-syn. lig(S5)
	pCB393	pRS304	*pNcTET*	43-8(low)-syn. lig(S2)
	pCB245	pRS605	*pADH1*	2x syn. clamp
	pCB247	pRS605	*pADH1*	3x syn. clamp
	pCB266	pRS605	*pADH1*	5x syn. clamp
2C	**pCB726**	pRS406	*p(n_c=3, 43-8 DBM3, n_c=3, 42-10 DMB7)minCyc1*	GFP
	pCB730	pRS406	*p(n_c=3, 43-8 DBM2, n_c=3, 42-10 DMB7)minCyc1*	GFP
	pCB723	pRS406	*p(n_c=2, 43-8 DBM2, n_c=2, 42-10 DMB5)minCyc1*	GFP
	pCB729	pRS406	*p(n_c=3, 43-8 DBM2, n_c=3, 42-10 DMB6)minCyc1*	GFP
	pCB302	pRS304	*pNcTET*	43-8(low)-syn. lig(S4)
	pCB393	pRS304	*pncTET*	43-8(low)-syn. lig(S2)
	pCB395	pRS304	*pncTET*	43-8(low)-syn. lig(S1)
	pN288	pRS304	*pNcZEV*	42-10(low)-syn. lig.(S4)
	pCB515	pRS304	*pNcZEV*	42-10(low)-syn. lig.(S2)
	pCB516	pRS304	*pNcZEV*	42-10(low)-syn. lig.(S1)
	pCB263	pRS605	*pADH1*	4x syn. clamp
	pCB266	pRS605	*pADH1*	5x syn. clamp
	pCB564	pRS605	*pADH1*	6x syn. clamp
3A	**pN8**	pRS406	*p(n_c =2, 43-8 DBM1)minCyc1*	GFP
	pCB278	pRS406	*p(n_c =4, 43-8 DBM3)minCyc1*	GFP
	pCB298	pRS304	*pNcTET*	43-8(low)-syn. lig.(S5)
	pCB263	pRS605	*pADH1*	4x syn. clamp
3B	**pN367**	pRS306	*p(n_c=4, 42-10 DBM2, n_c =3, 43-8 DBM1)minCyc1*	42-10(low)-syn. lig.(S2)
	pN410	pRS306	*p(n_c=2, 42-10 DBM1, n_c=2, 43-8 DBM2)minCyc1*	42-10(low)-syn. lig.(S2)
	pN488	pRS406	*p(n_c=4, 43-8 DBM1)minCyc1*	42-10(low)-syn. lig.(S5)
	pN489	pRS406	*p(n_c=4, 43-8 DBM1)minCyc1*	42-10(low)-syn. lig.(S4)
	pN464	pRS306	*p(n_c=4, 43-8 DBM3)minCyc1*	42-10(low)-syn. lig.(S4)
	pN369	pRS306	*p(n_c=4, 42-10 DBM4, n_c=3, 43-8 DBM1)minCyc1*	42-10(low)-syn. lig.(S2)
	pN281	pRS304	*pNcTET*	43-8(low)-no lig.
	pCB298	pRS304	*pNcTET*	43-8(low)-syn. lig.(S5)
	pCB301	pRS304	*pNcTET*	43-8(low)-syn. lig.(S4)
	pCB263	pRS605	*pADH1*	4x syn. clamp
	pN286	pRS603	*p(n_c=4, 42-10 DBM1)minCyc1*	GFP
4A	**pN8**	pRS406	*p(n_c=2, 43-8 DBM1)minCyc1*	GFP
	pN468	pRS306	*p(n_c=5, 43-8 DBM3)minCyc2*	42-10(low)-syn. lig.(S2)
	pCB298	pRS304	*pNcTET*	43-8(low)-syn. lig.(S5)

	pCB266	pRS605	*pADH1*	5x syn. clamp
	pN287	pRS603	*p(n_c=5, 42-10 DBM1)minCyc1*	GFP
4B/S24	**pN463**	pRS306	*p(n_c=4, 43-8 DBM3)minCyc1*	42-10(low)-syn. lig.(S5)
	pN409	pRS306	*p(n_c=2, 42-10 DBM1, n_c=2, 43-8 DBM2)minCyc1*	42-10(low)-syn. lig.(S5)
	pCB298	pRS304	*pNcTET*	43-8(low)-syn. lig.(S5)
	pCB301	pRS304	*pNcTET*	43-8(low)-syn. lig.(S4)
	pCB263	pRS605	*pADH1*	4x syn. clamp
	pN451	pRS603	*p(n_c=2, 43-8 DBM2, n_c=2, 42-10 DBM1)minCyc1*	mKate
	pN400	pRS603	*p(n_c=2, 43-8 DBM2, n_c=2, 42-10 DBM1)minCyc1*	GFP
S2B,C	**pCB342**	pMAL-c5	*Ptac*	MBP-43-8(low)-syn. lig.(S5)
	pCB347	pMAL-c5	*Ptac*	MBP-43-8(high)-syn. lig.(S5)
	pN93	pMAL-c5	*Ptac*	MBP-42-10(low)-syn. lig.(S5)
	pN313	pMAL-c5	*Ptac*	MBP-42-10(high)-syn. lig.(S5)
S3B,C,D	**pCB378**	pMAL-c5	*Ptac*	MBP-syn.
	pCB425	pMAL-c5	*Ptac*	MBP-erb.
	pCB380	pMAL-c5	*Ptac*	MBP-43-8(low)-syn. lig. (S1)
	pCB381	pMAL-c5	*Ptac*	MBP-43-8(low)-syn. lig. (S2)
	pCB382	pMAL-c5	*Ptac*	MBP-43-8(low)-syn. lig. (S3)
	pCB384	pMAL-c5	*Ptac*	MBP-43-8(low)-syn. lig. (S4)
	pCB385	pMAL-c5	*Ptac*	MBP-43-8(low)-syn. lig. (S5)
	pCB386	pMAL-c5	*Ptac*	MBP-43-8(low)-syn. lig. (S6)
	pCB387	pMAL-c5	*Ptac*	MBP-43-8(low)-syn. lig. (S7)
	pCB379	pMAL-c5	*Ptac*	MBP-43-8(low)-syn. lig. (S5)
S4A	**pRS406**	pRS406	n/a	n/a
	pL329	pRS304	*pNcTET*	GFP
	pL330	pRS304	*NL-TET*	GFP
	pCB702	pRS603	*pNcZEV*	GFP
	pCB703	pRS603	*pADH1*	GFP
	pCB704	pRS605	*pNcTET*	GFP
	pCB705	pRS605	*pADH1*	GFP
S4B	**pCB298**	pRS304	*pNcTET*	43-8(low)-syn. lig.(S5)
S4D	**pN20**	pRS406	*p(n=2, 43-8 DBM1)minCyc1*	GFP
	pN187	pRS605	*pNcZEV*	2x syn. clamp
	pN496	pRS605	*pTEF1*	97-4 ZEV
	pN498	pRS605	*pNcZEV*	43-8_4x, lig S5 (5GS)
S5	**pCB342**	pMAL-c5	*Ptac*	MBP-43-8(low)-syn. lig.(S5)
	pCB429	pMAL-c5	*Ptac*	1x syn.
S6	**pN8**	pRS406	*p(n_c=2, 43-8 DBM1)minCyc1*	GFP
	pCB230	pRS605	*pADH1*	2x syn. clamp (5GS)
	pCB244	pRS605	*pADH1*	2x syn. clamp (10GS)
	pCB245	pRS605	*pADH1*	2x syn. clamp (20GS)
	pCB303	pRS304	*pNcTET*	43-8(low)-syn. lig. (S6) (0GS)
	pCB300	pRS304	*pNcTET*	43-8(low)-syn. lig (S6) (5GS)
	pCB299	pRS304	*pNcTET*	43-8(low)-syn. lig. (S6) (10GS)
	pL372	pRS304	*pNcTET*	43-8(low)-syn. lig. (S5) (0GS)
	pCB298	pRS304	*pNcTET*	43-8(low)-syn. lig. (S5) (5GS)
	pCB304	pRS304	*pNcTET*	43-8(low)-syn. lig. (S5) (10GS)
	pCB303	pRS304	*pNcTET*	43-8(low)-syn. lig. (S4) (0GS)
	pCB301	pRS304	*pNcTET*	43-8(low)-syn. lig. (S4) (5GS)
	pCB267	pRS304	*pNcTET*	43-8(low)-syn. lig. (S4) (10GS)
S12C	**pCB707**	pRS406	*p(nc=1, 43-8 DBM1)minCyc1*	GFP
	pN8	pRS406	*p(n=2, 43-8 DBM1)minCyc1*	GFP
	pN27	pRS406	*p(n=3, 43-8 DBM1)minCyc1*	GFP
	pN20	pRS406	*p(n=4, 43-8 DBM1)minCyc1*	GFP
	pCB282	pRS406	*p(n=5, 43-8 DBM1)minCyc1*	GFP
	pN18	pRS406	*p(n=3, 43-8 DBM3)minCyc1*	GFP
	pCB280	pRS406	*p(n=5, 43-8 DBM3)minCyc1*	GFP
	pCB276	pRS406	*p(n=3, 43-8 DBM2)minCyc1*	GFP
	pCB279	pRS406	*p(n=4, 43-8 DBM2)minCyc1*	GFP

	pCB281	pRS406	*p(n=5, 43-8 DBM2)minCyc1*	GFP
	pCB298	pRS304	*pNcTET*	43-8(low)-syn. lig(S5)
	pCB300	pRS304	*pNcTET*	43-8(low)-syn. lig(S6)
	pCB393	pRS304	*pNcTET*	43-8(low)-syn. lig(S2)
	pCB301	pRS304	*pNcTET*	43-8(low)-syn. lig(S4)
	pCB245	pRS605	*pADH1*	2x syn. clamp
	pCB247	pRS605	*pADH1*	3x syn. clamp
	pCB263	pRS605	*pADH1*	4x syn. clamp
	pCB266	pRS605	*pADH1*	5x syn. clamp
S15	**pCB721**	pRS406	*p(n_c=2, 43-8 DBM3, n_c=2, 42-10 DMB6)minCyc1*	GFP
	pCB722	pRS406	*p(n_c=2, 43-8 DBM3, n_c=2, 42-10 DMB5)minCyc1*	GFP
	pCB723	pRS406	*p(n_c=2, 43-8 DBM2, n_c=2, 42-10 DMB5)minCyc1*	GFP
	pCB724	pRS406	*p(n_c=2, 43-8 DBM2, n_c=2, 42-10 DMB6)minCyc1*	GFP
	pCB725	pRS406	*p(n_c=3, 43-8 DBM3, n_c=2, 42-10 DMB6)minCyc1*	GFP
	pCB726	pRS406	*p(n_c=3, 43-8 DBM3, n_c=3, 42-10 DMB7)minCyc1*	GFP
	pCB727	pRS406	*p(n_c=2, 43-8 DBM1, n_c=2, 42-10 DMB5)minCyc1*	GFP
	pCB728	pRS406	*p(n_c=2, 43-8 DBM1, n_c=3, 42-10 DMB5)minCyc1*	GFP
	pCB729	pRS406	*p(n_c=3, 43-8 DBM2, n_c=3, 42-10 DMB6)minCyc1*	GFP
	pCB730	pRS406	*p(n_c=3, 43-8 DBM2, n_c=3, 42-10 DMB7)minCyc1*	GFP
	pCB731	pRS406	*p(n_c=2, 43-8 DBM2, n_c=2, 42-10 DBM4)minCyc1*	GFP
	pCB732	pRS406	*p(n_c=3, 43-8 DBM3, n_c=2, 42-10 DBM1)minCyc1*	GFP
	pCB302	pRS304	*pNcTET*	43-8(low)-syn. lig(S4)
	pCB393	pRS304	*pncTET*	43-8(low)-syn. lig(S2)
	pCB395	pRS304	*pncTET*	43-8(low)-syn. lig(S1)
	pN288	pRS603	*pNcZEV*	42-10(low)-syn. lig.(S4)
	pCB515	pRS603	*pNcZEV*	42-10(low)-syn. lig.(S2)
	pCB516	pRS603	*pNcZEV*	42-10(low)-syn. lig.(S1)
	pCB263	pRS605	*pADH1*	4x syn. clamp
	pCB266	pRS605	*pADH1*	5x syn. clamp
	pCB564	pRS605	*pADH1*	6x syn. clamp
S16D, E	**pRS406**	pRS406	empty	empty
	pL329	pRS304	multiple (see Fig. S4)	*multiple (see Fig. S4)*
S17B	**pRS406**	pRS406	empty	GFP
	pN8	pRS406	*p(n_c=2, 43-8 DBM1)minCyc1*	GFP
	pN491	pRS406	*p(n_c=4, 43-8 DBM1)minCyc1*	42-10(low)-no lig.
	pN488	pRS406	*p(n_c=4, 43-8 DBM1)minCyc1*	42-10(low)-syn. lig.(S5)
	pL329	pRS304	*pNcTET*	GFP
	pCB298	pRS304	*pNcTET*	43-8(low)-syn. lig.(S5)
	pN281	pRS304	*pNcTET*	43-8(low)-no lig.
	pN286	pRS603	*p(n_c=4, 42-10 DBM1)minCyc1*	GFP
S17C	**pN8**	pRS406	*p(n_c=2, 43-8 DBM1)minCyc1*	GFP
	pCB277	pRS406	*p(n_c=3, 43-8 DBM1)minCyc1*	GFP
	pN20	pRS406	*p(n_c=4, 43-8 DBM1)minCyc1*	GFP
	pCB282	pRS406	*p(n_c=5, 43-8 DBM1)minCyc1*	GFP
	pCB301	pRS304	*pNcTET*	43-8(low)-syn. lig.(S4)
	pCB245	pRS605	*pADH1*	2x syn. clamp
	pCB247	pRS605	*pADH1*	3x syn. clamp
	pCB263	pRS605	*pADH1*	4x syn. clamp
	pCB266	pRS605	*pADH1*	5x syn. clamp
S20	**pN490**	pRS406	*p(n_c=4, 43-8 DBM1)minCyc1*	42-10(high)-syn. lig.(S5)
	pN488	pRS406	*p(n_c=4, 43-8 DBM1)minCyc1*	42-10(low)-syn. lig.(S5)
	pN489	pRS406	*p(n_c=4, 43-8 DBM1)minCyc1*	42-10(low)-syn. lig.(S4)
	pN350	pRS306	*p(n_c=4, 42-10 DBM3, n_c=2, 43-8 DBM1)minCyc1*	42-10(low)-syn. lig.(S5)
	pN354	pRS306	*p(n_c=4, 42-10 DBM2, n_c=2, 43-8 DBM1)minCyc1*	42-10(low)-syn. lig.(S5)
	pN355	pRS306	*p(n_c=4, 42-10 DBM2, n_c=2, 43-8 DBM1)minCyc1*	42-10(low)-syn. lig.(S2)
	pN359	pRS306	*p(n_c=4, 42-10 DBM4, n_c=2, 43-8 DBM1)minCyc1*	42-10(low)-syn. lig.(S2)
	pN360	pRS306	*p(n_c=5, 42-10 DBM4, n_c=2, 43-8 DBM1)minCyc1*	42-10(low)-syn. lig.(S5)
	pN361	pRS306	*p(n_c=5, 42-10 DBM4, n_c=2, 43-8 DBM1)minCyc1*	42-10(low)-syn. lig.(S2)
	pN364	pRS306	*p(n_c=4, 42-10 DBM3, n_c=3, 43-8 DBM1)minCyc1*	42-10(low)-syn. lig.(S5)

	pN366	pRS306	*p(n_c=4, 42-10 DBM2, n_c=3, 43-8 DBM1)minCyc1*	42-10(low)-syn. lig.(S5)
	pN367	pRS306	*p(n_c=4, 42-10 DBM2, n_c=3, 43-8 DBM1)minCyc1*	42-10(low)-syn. lig.(S2)
	pN368	pRS306	*p(n_c=4, 42-10 DBM4, n_c=3, 43-8 DBM1)minCyc1*	42-10(low)-syn. lig.(S5)
	pN369	pRS306	*p(n_c=4, 42-10 DBM4, n_c=3, 43-8 DBM1)minCyc1*	42-10(low)-syn. lig.(S2)
	pN353	pRS306	*p(n_c=5, 42-10 DBM3, n_c=2, 43-8 DBM1)minCyc1*	42-10(low)-syn. lig.(S2)
	pN365	pRS306	*p(n_c=4, 42-10 DBM3, n_c=3, 43-8 DBM1)minCyc1*	42-10(low)-syn. lig.(S2)
	pN409	pRS306	*p(n_c=2, 42-10 DBM1, n_c=2, 43-8 DBM2)minCyc1*	42-10(low)-syn. lig.(S5)
	pN410	pRS306	*p(n_c=2, 42-10 DBM1, n_c=2, 43-8 DBM2)minCyc1*	42-10(low)-syn. lig.(S2)
	pN348	pRS306	*p(n_c=2, 42-10 DBM1, n_c=2, 43-8 DBM1)minCyc1*	42-10(low)-syn. lig.(S5)
	pN344	pRS306	*p(n_c=3, 42-10 DBM1, n_c=1, 43-8 DBM1)minCyc1*	42-10(low)-syn. lig.(S5)
	pN464	pRS306	*p(n_c=4, 43-8 DBM3)minCyc1*	42-10(low)-syn. lig.(S4)
	pN463	pRS306	*p(n_c=4, 43-8 DBM3)minCyc1*	42-10(low)-syn. lig.(S5)
	pN464	pRS306	*p(n_c=4, 43-8 DBM3)minCyc1*	42-10(low)-syn. lig.(S4)
	pN468	pRS306	*p(n_c=5, 43-8 DBM3)minCyc1*	42-10(low)-syn. lig.(S2)
	pN281	pRS304	*pNcTET*	43-8(low)-no lig.
	pCB298	pRS304	*pNcTET*	43-8(low)-syn. lig.(S5)
	pCB301	pRS304	*pNcTET*	43-8(low)-syn. lig.(S4)
	pCB263	pRS605	*pADH1*	4x syn. clamp
	pCB266	pRS605	*pADH1*	5x syn. clamp
	pN286	pRS603	*p(n_c=4, 42-10 DBM1)minCyc1*	GFP
	pN287	pRS603	*p(n_c=5, 42-10 DBM1)minCyc1*	GFP

TABLE S2: Yeast Strains

		Marker Loci			
FIGURE	**STRAIN ID**	**URA3**	**TRP4**	**LEU2**	**HIS3**
1E	**sCB01**	pN8	pCB298	pN187	
	sCB02	pN8	pCB300	pN187	
	sCB03	pN8	pCB302	pN187	
	sCB04	pCB277	pCB298	pCB397	
	sCB05	pCB228	pCB298	pCB398	
	sCB06	CB269	pCB298	pN187	
	sCB07	pN8	pCB706	pN187	
2A	**sCB08**	pCB707	pCB298		
	sCB09	pN8	pCB298	pCB245	
	sCB10	pN18	pCB393	pCB247	
	sCB11	pCB280	pCB393	pCB266	
	sCB56	pCB281	pCB393	pCB266	
2B	**sCB12**	pCB726	pCB302	pCB564	pN288
	sCB13	pCB730	pCB393	pCB564	pCB515
	sCB14	pCB723	pCB393	pCB263	pCB515
	sCB15	pCB729	pCB395	pCB564	pCB516
3A	**sCB16**	pN8	pCB298		
	sCB17	pCB278	pCB298	pCB263	
3B	**yN483**	pN367	pN281	pCB263	pN286
	yN143	pN410	pCB301	pCB263	pN286
	yN005	pN488	pN281	pCB263	pN286
	yN006	pN489	pN281	pCB263	pN286
	yN233	pN464	pCB298	pCB263	pN286
	yN485	pN369	pN281	pCB263	pN286
4A	**sCB18**	pN8	pCB298		
	yN267	pN468	pCB298	pCB266	pN287
4B/S24	**yN473**	pN463	pCB298	pCB263	pN451
	yN140	pN409	pCB301	pCB263	pN400
S4A	**sCB19**	pRS406	pL329		
	sCB20	pRS406	pL330		
	sCB21			pCB704	

	sCB22				pCB702
	sCB23			pCB705	
	sCB24				pCB703
	sCB25	pRS406	pCB298		
S4D	**yN701**	pN20			
	yN711	pN20		pN187	
	yN712	pN20		pN496	
	yN757	pN20		pN498	
S6	**yN490**	pN8	pCB303	pCB230	
	yN491	pN8	pCB300	pCB230	
	yN492	pN8	pCB299	pCB230	
	yN493	pN8	pL372	pCB230	
	yN494	pN8	pCB298	pCB230	
	yN495	pN8	pCB304	pCB230	
	yN496	pN8	pCB303	pCB230	
	yN497	pN8	pCB301	pCB230	
	yN498	pN8	pCB267	pCB230	
	yN499	pN8	pCB303	pCB244	
	yN500	pN8	pCB300	pCB244	
	yN501	pN8	pCB299	pCB244	
	yN502	pN8	pL372	pCB244	
	yN503	pN8	pCB298	pCB244	
	yN504	pN8	pCB304	pCB244	
	yN505	pN8	pCB303	pCB244	
	yN506	pN8	pCB301	pCB244	
	yN507	pN8	pCB267	pCB244	
	yN508	pN8	pCB303	pCB245	
	yN509	pN8	pCB300	pCB245	
	yN510	pN8	pCB299	pCB245	
	yN511	pN8	pL372	pCB245	
	yN512	pN8	pCB298	pCB245	
	yN513	pN8	pCB304	pCB245	
	yN514	pN8	pCB303	pCB245	
	yN515	pN8	pCB301	pCB245	
	yN516	pN8	pCB267	pCB245	
S12C	**sCB08**	pCB707	pCB298		
	yN715	pN8	pCB298		
	yN716	pN27	pCB298		
	yN717	pN20	pCB298		
	yN718	pCB282	pCB298		
	sCB09	pN8	pCB298	pCB245	
	sCB10	pN18	pCB393	pCB247	
	sCB11	pCB280	pCB393	pCB266	
	sCB51	pN20	pCB300	pCB263	
	sCB52	pCB280	pCB301	pCB266	
	sCB53	pN8	pCB301	pCB245	
	sCB54	pCB276	pCB393	pCB247	
	sCB55	pCB279	pCB298	pCB263	
	sCB56	pCB281	pCB393	pCB266	
S15	**sCB26**	pCB721	pCB302	pCB263	pN288
	sCB27	pCB721	pCB393	pCB263	pCB515
	sCB28	pCB722	pCB302	pCB263	pN288
	sCB29	pCB722	pCB393	pCB263	pCB515
	sCB30	pCB723	pCB302	pCB263	pN288
	sCB14	pCB723	pCB393	pCB263	pCB515
	sCB31	pCB724	pCB302	pCB263	pN288
	sCB32	pCB724	pCB393	pCB263	pCB515
	sCB33	pCB725	pCB302	pCB266	pN288
	sCB34	pCB725	pCB393	pCB266	pCB515
	sCB12	pCB726	pCB302	pCB564	pN288
	sCB35	pCB726	pCB393	pCB564	pCB515
	sCB36	pCB727	pCB302	pCB263	pN288
	sCB37	pCB727	pCB393	pCB263	pCB515
	sCB38	pCB728	pCB302	pCB266	pN288
	sCB39	pCB728	pCB393	pCB266	pCB515

	sCB40	pCB729	pCB302	pCB564	pN288
	sCB41	pCB729	pCB393	pCB564	pCB515
	sCB15	pCB729	pCB395	pCB564	pCB516
	sCB42	pCB730	pCB302	pCB564	pN288
	sCB13	pCB730	pCB393	pCB564	pCB515
	sCB43	pCB731	pCB302	pCB263	pN288
	sCB44	pCB731	pCB393	pCB263	pCB515
	sCB45	pCB732	pCB302	pCB266	pN288
	sCB46	pCB732	pCB393	pCB266	pCB515
S16D,E	**sCB30**	pRS406	pL329		
S17B	**sCB31**	pRS406	pL329		
	sCB32	pN8	pCB298		
	yN474	pN491	pN281		pN286
	yN005	pN488	pN281	pCB263	pN286
S17C	**sCB47**	pN8	pCB301	pCB245	
	sCB48	pCB277	pCB301	pCB247	
	sCB49	pN20	pCB301	pCB263	
	sCB50	pCB282	pCB301	pCB266	
S20	**yN004**	pN488	pN281	pCB263	pN286
	yN005	pN489	pN281	pCB263	pN286
	yN006	pN490	pN281	pCB263	pN286
	yN475	pN350	pN281	pCB263	pN286
	yN476	pN354	pN281	pCB263	pN286
	yN477	pN355	pN281	pCB263	pN286
	yN478	pN359	pN281	pCB263	pN286
	yN479	pN360	pN281	pCB266	pN287
	yN480	pN361	pN281	pCB266	pN287
	yN481	pN364	pN281	pCB263	pN286
	yN482	pN366	pN281	pCB263	pN286
	yN483	pN367	pN281	pCB263	pN286
	yN484	pN368	pN281	pCB263	pN286
	yN485	pN369	pN281	pCB263	pN286
	yN486	pN353	pN281	pCB266	pN287
	yN487	pN365	pN281	pCB263	pN286
	yN137	pN409	pCB298	pCB263	pN286
	yN143	pN410	pCB301	pCB263	pN286
	yN488	pN348	pCB298	pCB263	pN286
	yN489	pN344	pCB298	pCB263	pN286
	yN233	pN464	pCB298	pCB263	pN286
	yN241	pN463	pCB301	pCB263	pN286
	yN245	pN464	pCB301	pCB263	pN286
	yN288	pN468	pCB301	pCB266	pN287

Table S3. Data Fitting

Name of Fitting Function	Data Type	Output Parameters	MATLAB solver	Associated Figures
Hillfun.m (hill function)	Anisotropy or fluorescence dose response	Hill parameters	least squares	1C, 2A, 3A, S2B, S3B, S5, S11, S12, S16E
Anisotropy_Fit.m (Wang fit, see reference 4)	fluor. anisotropy competition	protein-competitor affinity	least squares	S2C, S3C,D
MeanTxn_OneTF.m	thermodynamic model for a one TF assembly	[TF], [Clamp] binding affinities	least squares	1E

polyfitB.m (polynomial degree of 1)	thermodynamic model parameter extrapolation	slope and intercept of linear fit	polynomial fit	S10
fit_logistic.m (logistic function)	promoter rate extrapolation	logistic function variables	least squares	S17C
OneNode.m, TwoNode.m, ThreeNode.m	microfluidic time courses	kinetic rates	Pattern Search	S17B

Table S4. Simulation Functions

Name of Custom Function	Function Output	Input Parameters	Associated Figures	Function Description
MeanTxn_OneTF.m	one-input dose response	[TF], [Clamp], *n*, binding affinities	2A, S11, S12	uses protein concentrations and thermos. parameters to calculate mean transcriptional rate for a 1 TF, 1 Clamp assembly
MeanTxn_TwoTF.m	two-input decision surface	[TF1], [TF2], [Clamp], *n*, binding affinities	2B, S14, S15	uses protein concentrations and thermo. parameters to calculate mean transcriptional rate for a 2 TF, 1 Clamp assembly
OneNode.m	one-node cascade dynamics	[GFP] @t=0, binding affinities, kinetic rates, Dox input	S17	predicts dynamics of a one node circuit for a defined Dox input over time
TwoNode.m	two-node cascade dynamics	[TF1],[GFP] @t=0, binding affinities, kinetic rates, Dox input	3A,B, 4A, S18-22	predicts dynamics of a two node circuit for a defined Dox input over time
ThreeNode.m	three-node cascade dynamics	[TF1],[TF2],[GFP] @t=0, binding affinities, kinetic rates, Dox input	3B, 4A, S18-22	predicts dynamics of a three node circuit for a defined Dox input over time
ThreeNodeFB.m	three-node cascade + FB dynamics	[TF1],[TF2],[GFP] @t=0, binding affinities, kinetic rates, Dox input	3B, S18-19, S22	predicts dynamics of a three node + FB circuit for a defined Dox input over time
CFFL.m	CFFL dynamics	[TF1],[TF2],[GFP] @t=0, binding affinities, kinetic rates, Dox input	S21-23	predicts dynamics of a CFFL circuit for a defined Dox input over time
CFFLFB.m	CFFL + FB dynamics	[TF1],[TF2],[GFP] @t=0, binding affinities, kinetic rates, Dox input	S22-23	predicts dynamics of a CFFL + FB circuit for a defined Dox input over time

Supplementary Movies

Movies S1 and S2. Time lapse fluorescence microscopy of yeast strains harboring 12 engineered circuits in two distinct microfluidic chambers (movies S1 and S2, respectively). GFP fluorescence (top) is shown in cyan and tracks the activation/deactivation time courses of the circuits following a 16 h Dox induction pulse (10 μg/mL), with corresponding phase contrast time lapse (below). Circuit configurations were selected from the dynamic behavior space of **Fig. 3** and ordered by their experimentally determined deactivation time (t_d) from shortest to longest. From left to right: circuits correspond to #1, 3, 14, 17, 12, 18 (top), and 11, 13, 8, 9, 15, 16 (bottom) listed in **Figure S20**. Scale bar = 10 μm.

References and Notes

34. Jantz, D. and J.M. Berg, Probing the DNA-binding affinity and specificity of designed zinc finger proteins. *Biophys J*. **98**, 852-60 (2010).

35. Wang, Z.X., An exact mathematical expression for describing competitive binding of two different ligands to a protein molecule. *FEBS Lett*. **360**, 111-4 (1995).

36. Cookson, S., et al., Monitoring dynamics of single-cell gene expression over multiple cell cycles. *Mol Syst Biol*. **1**, 2005 0024 (2005).

37. Vega, N.M., et al., Signaling-mediated bacterial persister formation. *Nature chemical biology*. **8**, 431-33 (2012).

38. Duffy, D.C., et al., Rapid Prototyping of Microfluidic Systems in Poly(dimethylsiloxane). *Anal Chem*. **70**, 4974-84 (1998).

39. Unger, M.A., et al., Monolithic microfabricated valves and pumps by multilayer soft lithography. *Science*. **288**, 113-6 (2000).

40. Wang, Q., et al., Image segmentation and dynamic lineage analysis in single-cell fluorescence microscopy. *Cytometry A*. **77**, 101-10 (2010).

41. Harris, B.Z., B.J. Hillier, and W.A. Lim, Energetic determinants of internal motif recognition by PDZ domains. *Biochemistry*. **40**, 5921-30 (2001).

42. Wiedemann, U., et al., Quantification of PDZ domain specificity, prediction of ligand affinity and rational design of super-binding peptides. *J Mol Biol*. **343**, 703-18 (2004).

43. Bintu, L., et al., Transcriptional regulation by the numbers: models. *Current opinion in genetics & development*. **15**, 116-24 (2005).

44. Mirny, L.A., Nucleosome-mediated cooperativity between transcription factors. *Proc Natl Acad Sci U S A*. **107**, 22534-9 (2010).

45. Hansen, A.S. and E.K. O'Shea, Promoter decoding of transcription factor dynamics involves a trade-off between noise and control of gene expression. *Mol Syst Biol*. **9**, 704 (2013).

46. Mao, C., et al., Quantitative analysis of the transcription control mechanism. *Mol Syst Biol*. **6**, 431 (2010).

47. Aymoz, D., et al., Timing of gene expression in a cell-fate decision system. *Mol Syst Biol*. **14**, e8024 (2018).

48. Guarente, L., et al., Distinctly regulated tandem upstream activation sites mediate catabolite repression of the CYC1 gene of S. cerevisiae. *Cell*. **36**, 503-11 (1984).

49. Estrada, J., et al., Information Integration and Energy Expenditure in Gene Regulation. *Cell*. **166**, 234-44 (2016).

50. Bintu, L., et al., Transcriptional regulation by the numbers: applications. *Current opinion in genetics & development*. **15**, 125-35 (2005).

51. Kang, J.S., Correlation between functional and binding activities of designer zinc-finger proteins. *Biochem J*. **403**, 177-82 (2007).

52. Ferrell, J.E., Jr., Self-perpetuating states in signal transduction: positive feedback, double-negative feedback and bistability. *Curr Opin Cell Biol*. **14**, 140-8 (2002).

53. Bennett, M.R., et al., Metabolic gene regulation in a dynamically changing environment. *Nature*. **454**, 1119-22 (2008).

54. Bialek, W., et al., Reading a neural code. *Science*. **252**, 1854-7 (1991).